

1962

Propagation characteristics of capillary ripples

Julian Adin Mann Jr.
Iowa State University

Follow this and additional works at: <https://lib.dr.iastate.edu/rtd>

 Part of the [Physical Chemistry Commons](#)

Recommended Citation

Mann, Julian Adin Jr., "Propagation characteristics of capillary ripples " (1962). *Retrospective Theses and Dissertations*. 2066.
<https://lib.dr.iastate.edu/rtd/2066>

This Dissertation is brought to you for free and open access by the Iowa State University Capstones, Theses and Dissertations at Iowa State University Digital Repository. It has been accepted for inclusion in Retrospective Theses and Dissertations by an authorized administrator of Iowa State University Digital Repository. For more information, please contact digirep@iastate.edu.

This dissertation has been 62-4168
microfilmed exactly as received

MANN, Jr., Julian Adin, 1932-
PROPAGATION CHARACTERISTICS OF CAPILLARY
RIPPLES.

Iowa State University of Science and Technology
Ph.D., 1962
Chemistry, physical

University Microfilms, Inc., Ann Arbor, Michigan

PROPAGATION CHARACTERISTICS OF CAPILLARY RIPPLES

by

Julian Adin Mann, Jr.

A Dissertation Submitted to the
Graduate Faculty in Partial Fulfillment of
The Requirements for the Degree of
DOCTOR OF PHILOSOPHY

Major Subject: Physical Chemistry

Approved:

Signature was redacted for privacy.

In Charge of Major Work

Signature was redacted for privacy.

Head of Major Department

Signature was redacted for privacy.

Dean of Graduate College

Iowa State University
Of Science and Technology
Ames, Iowa

1962

TABLE OF CONTENTS

	Page
DEDICATION	iv
INTRODUCTION	1
Surface Waves	5
Purpose of This Research	11
THE HYDRODYNAMIC THEORY OF SURFACE LAYERS	12
Introduction	12
Insoluble Monolayer Case	18a
Soluble Monolayer Case	53
EXPERIMENTAL	73
Automatic Surface Balance	73
Ripple Instrumentation	90
Miscellaneous Comments on Technique	145
Suggestions for Improved Instrumentation	149
Film Spreading	151
Materials	152
RESULTS	155
Theoretical Calculation	155
Experimental	162
DISCUSSION	198
Theory	198
Experimental	217
Conclusions and Recommendations	244

	Page
SUMMARY	250
LITERATURE CITED	252
ACKNOWLEDGMENTS	255

DEDICATION

To Arlene

And Our Children

Elizabeth, Jennifer, and Adin III

INTRODUCTION

The study of films spread on water dates back to before the last century. Benjamin Franklin, in 1765, carried out experiments on the spreading of oils on the pond at Clapham Common. It was not until 1891 that the first quantitative studies were reported by Fräulein Pockels. Rayleigh and Devaux were also pioneers in this field.

Hardy pointed out in 1913 that monomolecular films (monolayers) are formed from molecules having both a hydrophobic and hydrophilic part; the hydrophilic part must be oriented down into the aqueous substrate, the hydrophobic part up away from the substrate. In 1917 Langmuir provided conclusive experimental support for this idea through his studies of the compression properties of various long chain fatty acid monolayers. The names of Adam, Rideal, Harkins, Guastalla, Zisman and Dervichian are associated with more recent developments of experimental techniques for measuring monolayer compression, viscosity and orientation characteristics.

Methods for the measurement of monolayer properties are extensively discussed in the books by Adam (1), Harkins (2), Adamson (3), and Davies and Rideal (4). Adamson gives probably the best modern account of surface chemistry. Davies and Rideal, the newest of the cited books, is a

thorough exposition of the authors' viewpoint and researches on the properties of surface films. Harkins discusses most of his own work giving quantitative data on the properties of many insoluble film systems. Adam's book, written in 1941, is a classic in the field; it serves as a good source for review of the older literature.

The viscosity properties of monolayers have been extensively studied employing techniques adapted from methods often used to measure bulk viscosity. Canal techniques analogous to capillary flow viscosimeters, and rotating rings analogous to rotating bob viscosimeters have been used extensively (4).

The viscous force produced by shear motion through a surface film is given by

$$\underline{F} = \mu_s L \left(\frac{dq}{dr} \right) \Big|_{\text{surface}} \quad (\text{Eq. 1})$$

where μ_s is the surface viscosity constant, in units of $\frac{M}{T}$, L is the length of shear "lines" and $\frac{dq}{dr} \Big|_{\text{surface}}$ is the velocity

gradient between shearing "lines" on the film surface. In contrast to μ_s , the analogous bulk viscosity constant, μ_b , in units of $\frac{M}{TL}$, adds a length dimension so that the viscous force produced in bulk shear motion is given by

$$\underline{F} = \mu_b A \frac{dq}{dr} \quad . \quad (\text{Eq. 2})$$

A is the area of the shear "planes" and $\frac{dq}{dr}$ is the velocity gradient between the shear "planes."

The elastic properties of monolayers have not been explored to any great extent. In a recent paper reviewing work on this aspect of surface films, Tschoegl (5) pointed out that a number of authors have used elastic parameters which were dimensionally incorrect. One can define the compressional modulus K_c as

$$K_c = -S \left(\frac{\partial \pi}{\partial S} \right) \quad (\text{Eq. 3})$$

where $\pi = \gamma_0 - \gamma$, the change in surface tension ($\gamma_0 = 72 \text{ d/cm}$ for water) and S is the area occupied by one molecule in the film. The units on the surface elastic constant must be

$$\frac{M}{T^2} \quad . \quad (\text{Eq. 4a})$$

This is in contrast to the bulk elastic constant with units of

$$\frac{M}{T^2 L} \quad . \quad (\text{Eq. 4b})$$

The techniques previously used to study surface elastic constants were closely related to the rotating disk technique for measuring viscosity. Tschoegl's statement concerning the use of the oscillating needle is typical of the state of the art:

The oscillating needle offers certain experimental advantages over the disk or ring. Unfortunately no really satisfactory expression has been yet proposed for the calculation of the coefficient of surface viscosity or the surface shear modulus determined with an oscillating needle or vane, since the problem is indeed very difficult to treat hydrodynamically.

The study of capillary ripple propagation presents a different path to the visco-elastic properties of monolayers. Consider the profile of a free liquid surface crossed by forced ripples following the equation

$$\eta = \eta_0 \exp(-\alpha x) \cos(kx - \omega t) \quad . \quad (\text{Eq. 5})$$

The ripples, generated continuously at $x = 0$, travel in the positive x direction along the trough. The ripples die out according to the term $\exp(-\alpha x)$. It should be apparent that the area of the free surface in steady oscillation will be greater than its area at rest. It is also true that the local area available to monolayer molecules will fluctuate with time going through one complete oscillation in $\frac{2\pi}{\omega}$ seconds. This periodic area change must work against forces

associated with monolayer viscosity and elasticity. It is reasonable to expect that determination of the ripple propagation parameters, i.e., the ripple damping coefficient, the angular frequency ω , and the propagation velocity $c (= \frac{\omega}{k})$, should allow quantitative discussion of the visco-elastic properties of monolayers if the associated hydrodynamical problem can be solved.

Surface Waves

Wave motion has fascinated man for many centuries. This fascination is exemplified by the hours of pleasure often found by young children throwing pebbles into placid ponds. The expanding circle of ripples traveling away from a disturbance is familiar to many. It is quite natural that the wave motion of large bodies of water should have been closely studied; sea travel is an important aspect of our culture. The literature on water wave propagation is very extensive. One needs only to look at an example of this literature, Stoker's (6) "Water Waves," to realize that the problems treated are primarily concerned with the motion of large waves under the influence of a variety of boundary conditions. Most often the restoring force is considered to be only the conservative gravity field. Our interest is in the effect of surface restoring forces, that is, in the effect of surface tension phenomena on wave properties.

Thus restricting our literature search, we find that the bulk of the literature on waves is excluded. It is the purpose of this section to review the literature on the subject of capillary ripple propagation.

The calming effect of oil poured on turbulent sea has been known for a long time. Pliny recorded the practice of seamen pouring oil on rough water in the first century A.D. In 1762 Benjamin Franklin related stories of the use of oil to reduce surf or to reduce annoying ripple reflection patterns on lakes during spear fishing expeditions. In 1891 Fräulein Pöckels (7) showed experimentally that monolayers spread on water surfaces will damp surface ripples.

The functional relation between the wave propagation velocity and frequency, referred to as velocity dispersion, was first derived by Lord Kelvin (8) in 1871. This relation, subsequently called the Kelvin equation, is derived in the theoretical section, Equation 24, of This Thesis.

Experimental techniques for the study of capillary ripple phenomena have received little attention. In 1936 Brown (9) described a number of techniques for the measurement of ripple velocity; his bibliography of 20 entries included all important work on this subject up to 1936. No significant developments in technique have been published since that date. All of the methods investigated by Brown depended upon the direct measurement of ripple wave lengths by

optical techniques, and most of them depended upon the plane waves forming a series of approximately cylindrical lenses on the water surface. Lighting was usually synchronized with the wave production mechanism in order to cause progressive waves to appear as standing waves, that is, a stroboscopic effect was usually sought. Fairly precise knowledge of the ripple frequencies was obtained by a complex and, by comparison with modern techniques, rather amusing collection of equipment involving such items as an Osclim lamp, electrically driven tuning forks, and a stroboscopic disc mounted on the spindle of a "phonic" motor. The number of frequencies which Brown was able to use with these techniques was small and their range was also rather limited.

Only four journal papers (10, 11, 12, 13) have been published on the measurement of the amplitude and damping properties of capillary ripples. Brown's (10) paper published in 1936 was the most extensive publication on the experimental aspects of the problem, however, he presented only "preliminary results" on the damping coefficient for ripples moving on clean water surfaces at a single frequency, 300 cps. Briefly, he calculated the damping coefficient at a given frequency from optical measurements of the focal length change with ripple amplitude of the approximately cylindrical lens formed on the water surface by plane capillary waves. Brown, however, has not published on this

subject since 1936.

Davies and Rideal (4) very recently referred to damping of waves by monolayers. They had the following to say about the experimental problem of measuring damping properties:

"Experimentally, it is convenient to study wave-damping using an oscillating plate at a given amplitude and frequency to produce waves at one end of a very long Langmuir trough. One counts the number of waves, n_w , which can just be distinguished, or photographs the waves and finds n_w for the amplitude to be reduced to a certain level . . ." They presented some data on the wave damping properties of sodium lauryl sulfate films at a frequency of 50 cps. We have not found any further reports on their research in the current literature. To our knowledge, Brown's paper and the rather short section in the book by Davies and Rideal represent the total published effort in this field since 1936.

The theoretical aspects of capillary waves have received more attention. The work of Kelvin and others was summarized in Lamb's (14) classic on hydrodynamics. Both the propagation velocity equation and the theory of the damping of free wave motion under a number of different boundary conditions were discussed. However, the boundary conditions employed by Lamb were restricted to either the clean surface case or the rigid surface film case. In the latter case, the horizontal component of surface velocity was taken to be zero.

Klemm (15) and Wieghardt (16) approached the theory of the damping of normal mode wave motion on a free surface by writing the dynamic surface tension as a sum of the static surface tension and terms proportional to the particle velocity along the surface. Klemm introduced a single relaxation time constant into his formulation to take care of the local perturbation of surface concentration due to the wave motion. Wieghardt ignored the relaxation assumption of Klemm and proceeded to develop equations for the normal modes calculation assuming that the dynamic surface tension was modified by a term proportional to the velocity gradient across the surface.

Dorrestein (17) has rather recently written on the effect of surface films on water ripple propagation. He introduced surface viscosity through a term proportional to the derivative of the component of velocity parallel to the surface with respect to the distance parallel to the surface, and he introduced an elastic modulus term by assuming that surface pressure and area per molecule data were linearly related. This last assumption is true only for certain substances in certain surface concentration ranges.¹

¹Harkins (2, p. 114, Fig. 11) shows the force-area curves for palmitic acid at various temperatures. Both non-linear and linear regions exist in this system.

He allowed for hysteresis in monolayer compression by introducing a phase factor into the formulation.

Levich (18) in 1941 published two papers on the damping of surface waves treating both the soluble monolayer and the insoluble monolayer cases. He derived the boundary conditions from a thermodynamic point of view; film viscosity did not play a part in his theory. Levich's diffusion control theory of wave damping for soluble monolayers contained a number of ideas that were incorporated into our theory to be presented later. However, a consequence of the approximations Levich applied to his formulation of the time damping of capillary waves was that the horizontal component of velocity at the surface could be taken as zero; this result implies that the film produced by a soluble monolayer is rigid.

Koussakov (19) has treated the case of capillary waves at the interface between two viscous liquids at finite depth. A number of papers have been written on the damping of waves using the ideal fluid assumption (20, 21). Notable among these is a paper by Crapper (22) wherein he develops equations that are exact representations for progressive capillary waves of arbitrary amplitude. Case and Parkinson (23) have examined the damping of surface waves in liquids contained in cylinders. They use boundary layer theory to simplify the development of their theory.

There is every reason to expect that surface films should have visco-elastic properties analogous to those of bulk systems. There is no a priori reason to exclude either surface elastic forces or surface viscous forces from consideration in the hydrodynamic boundary value problem. We should expect that the surface elastic forces are proportional to the monolayer strain and the surface viscous forces are proportional to the rate of monolayer strain. No theory embodying these expectations has hitherto been presented.

Purpose of This Research

The purpose of this research effort can be broken into four parts:

1. To develop the instrumentation necessary to quickly and accurately measure the propagation parameters of surface films
2. To measure the propagation parameters on a number of representative film types
3. To develop the hydrodynamical theory of surface waves on the basis of our concept of the surface visco-elastic forces involved
4. To compare the theory to our experimental results.

THE HYDRODYNAMIC THEORY OF SURFACE LAYERS

Introduction

The theory of capillary ripple phenomena presented in This Thesis is developed within the framework of classical fluid dynamics. We have found that the approach to fluid dynamics given by Landau and Lifshitz (24) has been the one most useful and stimulating reference; the classic exposition by Lamb (14) must not be ignored. The writings of Wehausen and Laitone (25), Truesdell (26), and Sommerfeld (27) have been read with profit.

Birkhoff (28) has recently written a book which is largely devoted to two special aspects of fluid mechanics: the logical relation between theory and experiment, and the application of symmetry concepts. Birkhoff interestingly and at times somewhat cynically discussed the assumptions hidden in the mathematical formulation of fluid dynamical problems. Hurchelwood was quoted as having said "fluid dynamicists were divided into hydraulic engineers who observed what could not be explained, and mathematicians who explained things that could not be observed." Birkhoff admits that progress in the formulation and solution of the boundary value problems of "rational" hydrodynamics would have been much slower if rigorous mathematics had not been supplanted by "plausible intuitive hypotheses." The

following plausibility hypotheses were mentioned and appear especially suggestive for the formulation of the hydrodynamic surface layer theory:

- P1 Intuition determines which physical variables require consideration.
- P2 Small causes produce small effects, and infinitesimal causes produce infinitesimal effects.
- P3 Symmetric causes produce effects with the same symmetry.
- P4 The flow topology can be guessed by intuition.
- P5 The process of analysis can be freely used; the functions appearing can be freely integrated, differentiated, and expanded in series or integrals.
- P6 Mathematical problems suggested by intuitive physical ideas are well set.

These plausibility assumptions are often made tacitly in the formulation of physical theories. Our theory will make frequent use of these assumptions. We will try occasionally to point out where some of these assumptions are used as the theory develops.

Our theory will depend upon the validity of the Navier-Stokes equations of motion for describing the incompressible flow of viscous fluids (P1). The experimental evidence, e.g., see Birkhoff (28), pertaining to the validity of the

Navier-Stokes equation of motion strongly implies that this description can be applied successfully to incompressible fluid flow at low Mach numbers. We assume that the fluid of interest to us, water, is incompressible (P1) and experimentally we know that the fluid particle velocity was far below the sound propagation velocity.

The Navier-Stokes equations of motion are expressed in terms of the vector equation:

$$\rho \left\{ \frac{\partial \underline{q}}{\partial t} + (\underline{q} \cdot \nabla) \underline{q} \right\} = -\nabla p + \mu \nabla^2 \underline{q} + (\bar{\mu} + \frac{1}{3}\mu) \nabla \operatorname{div} \underline{q} + \underline{F} \quad . \quad (\text{Eq. 1})$$

The equation is simplified with the incompressibility assumption to

$$\rho \left\{ \frac{\partial \underline{q}}{\partial t} + (\underline{q} \cdot \nabla) \underline{q} \right\} = -\nabla p + \mu \nabla^2 \underline{q} + \underline{F} \quad (\text{Eq. 2})$$

where ρ = fluid density

\underline{q} = vector particle velocity

μ = viscosity coefficient

$\bar{\mu}$ = additional viscosity coefficient¹

¹The general theory of fluids requires two viscosity coefficients, the incompressibility assumption eliminates $\bar{\mu}$ from our consideration.

\underline{F} = body forces, e.g., gravity forces

p = pressure.

The experimental conditions are such that the sinusoidal wave amplitude and the particle velocity, \underline{q} , are very small. We wish to rationalize the linearization of the Navier-Stokes equation using the small amplitude assumption. Let us suppose that we can in view of the experimental magnitude of the wave amplitude express the various variables entering into the problem as power series expansions, (P2, P5). Let β be the perturbation parameter for the expansion, then

$$\underline{q} = \beta \underline{q}_1 + \beta^2 \underline{q}_2 + \dots$$

$$p = p_0 + \beta p_1 + \beta^2 p_2 + \dots$$

$$\underline{F} = \underline{F}_0 + \beta \underline{F}_1 + \beta^2 \underline{F}_2 + \dots \quad (\text{Eq. 3})$$

Substitution of these expansions into Equation 2 and then upon collecting terms of like powers of β , we find for β^0

$$-\nabla p_0 + \underline{F}_0 = 0 \quad (\text{Eq. 4})$$

and for β^1

$$\rho \frac{\partial \underline{q}_1}{\partial t} = -\nabla p_1 + \mu \nabla^2 \underline{q}_1 + \underline{F}_1 \quad (\text{Eq. 5})$$

We will ignore the higher order perturbation terms (P2). Equation 4, for the case of a conservative gravity field, just expresses the variation of pressure with depth in a static fluid. It is convenient to combine the zero order and first order perturbation equations through the following definitions:

$$\underline{q} = \beta \underline{q}_1$$

$$p = p_0 + \beta p_1$$

$$\underline{F} = \underline{F}_0 + \beta \underline{F}_1 \quad (\text{Eq. 6})$$

Then we see that Equations 4 and 5 combine to give

$$\rho \frac{\partial \beta \underline{q}_1}{\partial t} = -\nabla (p_0 + \beta p_1) + \mu \nabla^2 \beta \underline{q}_1 + \underline{F}_0 + \beta \underline{F}_1$$

or

$$\rho \frac{\partial \underline{q}}{\partial t} = -\nabla p + \mu \nabla^2 \underline{q} + \underline{F} \quad (\text{Eq. 7})$$

which is the linearized Navier-Stokes equation (LNS). The quantities \underline{q} , p , and \underline{F} are to be considered as reflecting

the actual physical quantities of velocity, pressure, and body forces to the precision of a first order approximation. The desirable feature of this linearization technique is that the extension to higher order approximations, while in practice difficult to calculate, is in principle obvious. It should be noted that the nonlinear terms start appearing with the second order perturbation equations. The reader is referred to the article by Wehausen and Laitone (25) for a more extensive discussion of perturbation techniques in the hydrodynamic theory of waves.

We shall first consider the case in which the fluid is assumed to be both incompressible and irrotational. These assumptions lead to the Kelvin (8) capillary ripple velocity dispersion relation. Only gravity and static surface tension forces enter into the formulation; the Euler equation of motion is used. The theory will then be generalized to include the fact that real fluids have viscosity; the LNS equation of motion will be used. The theory will also reflect the fact that surface films possess properties in addition to surface tension; surface film viscosity and elasticity will be included in the formulation of the dispersion equations. The surface properties enter the theory through the imposition of continuity on the stress tensor evaluated at the surface. This condition reflects the physical fact that, under our experimental conditions,

forces acting on any surface within the fluid region, including the bounding surface, must be continuous with respect to space and time variables. A further boundary condition is imposed on the system by the fact that a surface continuity equation must be obeyed. This boundary condition allows us to describe the insoluble monolayer and also the soluble monolayer systems. The soluble monolayer theory requires that a source-sink term be added to the surface continuity equation. The form of this source-sink term allows us to introduce mechanisms for surface adsorption into the theory.

Insoluble Monolayer Case

Ideal fluid theory

Focus attention on a fluid filling the region $y < 0$ with the fluid surface represented at rest by the equation $y = 0$, Figure 1. Let the surface undergo periodic perturbations in the y direction traveling in the x direction with velocity c , wave length $(k = \frac{2\pi}{\lambda})$, and frequency $\nu(\omega = 2\pi\nu)$. Let η , the height of the surface with respect to the plane $y = 0$, be a function of x and t . If the fluid is incompressible and irrotational, then

$$\nabla \cdot \underline{q} = 0 \quad (\text{Eq. 8})$$

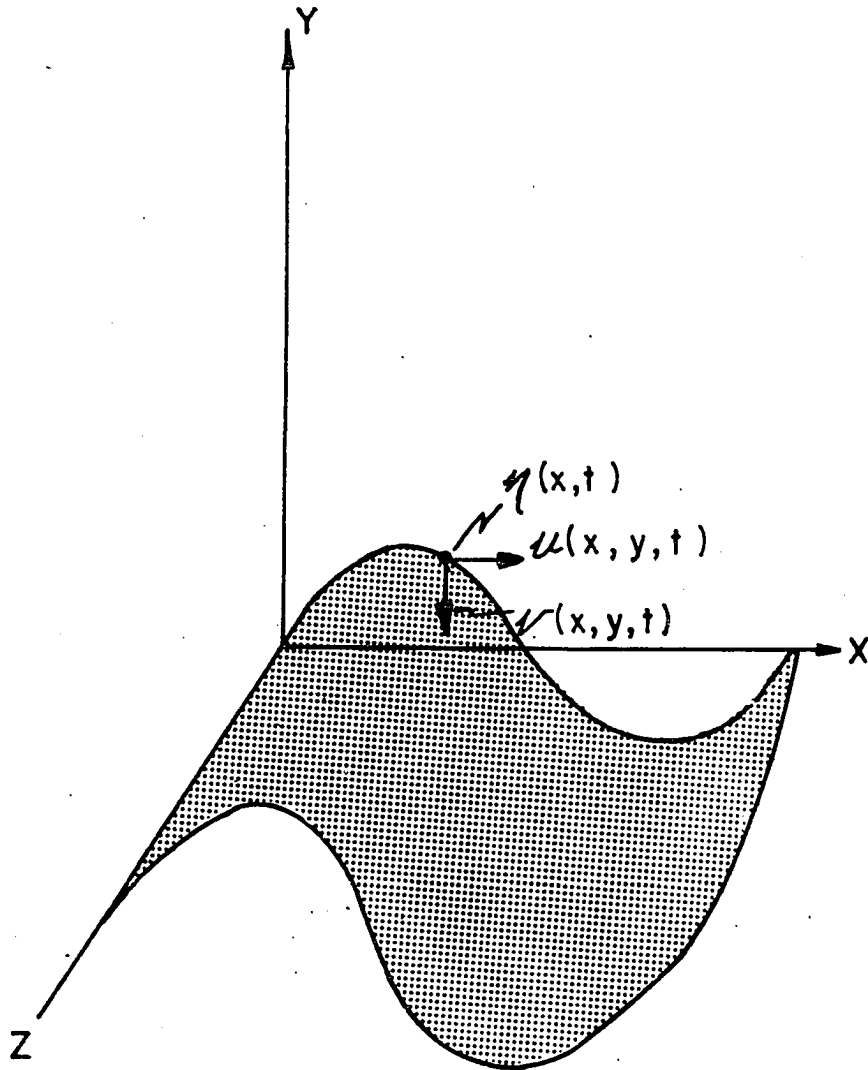


Figure 1. Fluid surface under periodic motion

$$\nabla \cdot \underline{xq} = 0 \quad (\text{Eq. 9})$$

where \underline{q} is the velocity vector represented by the ordered triple of numbers (u, v, w) . Suppose that the plane waves propagated along the x-axis have the form

$$\eta = \eta_0 \sin(kx - \omega t) \quad (\text{Eq. 10})$$

We know from Equation 9 that there exists a function φ such that

$$\underline{q} = -\nabla\varphi(x, y) \quad (\text{Eq. 11})$$

and in fact Equation 8 implies that φ must satisfy

$$\nabla^2 \varphi(x, y) = 0 \quad (\text{Eq. 12})$$

The boundary conditions on Equation 12 read

- i) φ is periodic in x .
- ii) If the fluid is considered to be unbounded in depth then

$$\lim_{y \rightarrow -\infty} \varphi(x, y) = 0 \quad .$$
- iii) If the fluid is considered to be of finite depth, h , then the condition on φ is

$$\lim_{y \rightarrow -h} \frac{\partial \varphi}{\partial y} = 0 \quad (\text{Eq. 13})$$

If the boundary conditions are taken to be i and ii, then

$$\varphi(x,y) = A \exp(ay) \cos(ax - b) .$$

If the boundary conditions are taken to be i and iii, then

$$\varphi(x,y) = A \cosh a(y + h) \cos(ax - b) .$$

Since $\underline{q}:(u,v,o) = (-\frac{\partial\varphi}{\partial x}, -\frac{\partial\varphi}{\partial y}, o)$, the y component of the velocity at the surface is given by

$$-\left(\frac{\partial\varphi}{\partial y}\right)_{y \rightarrow 0^-} = \dot{\eta} . \quad (\text{Eq. 14})$$

This implies, in case i and ii are taken as boundary conditions, that

$$\varphi(x,y) = \frac{\omega}{k} \eta_0 \exp(ky) \cos(kx - \omega t) , \quad (\text{Eq. 15'})$$

and in the case of i, iii conditions we have

$$\varphi(x,y) = \frac{\omega}{k} \eta_0 \coth(ky + kh) \cos(kx - \omega t) . \quad (\text{Eq. 15''})$$

We next relate $\varphi(x,y) \Big|_{y \rightarrow 0^-}$ to the surface tension of the fluid and the wave propagation velocity ($c = \frac{\omega}{k}$). The

equation of motion for inviscid flow (Euler's equation) is read from the Navier-Stokes equation as

$$\rho \frac{\partial \underline{q}}{\partial t} = \underline{F} - \nabla p \quad . \quad (\text{Eq. 16})$$

The body force is taken to be that of gravity;

$$\underline{F} : (0, -\rho g, 0) = -\nabla \rho g y \quad . \quad (\text{Eq. 17})$$

Substitution of Equations 11 and 17 into Equation 16 produces the result

$$\nabla \left[-\frac{\partial \varphi}{\partial t} + \frac{1}{\rho} p + g y \right] = 0 \quad (\text{Eq. 18})$$

which integrates to

$$-\frac{\partial \varphi}{\partial t} + \frac{1}{\rho} p + g y = \text{constant} \quad .$$

Assuming that $p = p_0$ when $\underline{q} = \underline{0}$, $y = 0$, we can write the pressure drop across the interface as

$$\Delta p = \rho \left[\frac{\partial \varphi}{\partial t} \Big|_{\eta} - g \eta \right] \quad (\text{Eq. 19})$$

but

$$\Delta p = -\gamma \frac{\partial^2 \eta}{\partial x^2} \quad (\text{Eq. 20})$$

where γ is the surface tension of the fluid.

Thus
$$-\frac{\partial^2 \eta}{\partial x^2} = \frac{\rho}{\gamma} \left[\frac{\partial \varphi}{\partial t} \eta - g\eta \right] . \quad (\text{Eq. 21})$$

Substitution of Equations 10, 15' and 10, 15'' gives

$$\omega^2 = \frac{k^3 \gamma}{\rho} + kg \quad (\text{Eq. 22'})$$

and
$$\omega^2 = \left(\frac{k^3 \gamma}{\rho} + kg \right) \tanh(kh) . \quad (\text{Eq. 22''})$$

Equation 22' can also be written as

$$c = \sqrt[3]{v \left[\frac{g}{2\pi} \left(\frac{v}{\lambda} \right)^2 + \frac{2\pi\gamma}{\rho} \right]} \quad (\text{Eq. 23})$$

and in case the gravity term can be ignored

$$c = \sqrt[3]{\frac{2\pi\gamma}{\rho} v}$$

or
$$\omega^2 = \frac{k^3 \gamma}{\rho} . \quad (\text{Eq. 24})$$

Waves obeying Equation 24 are often called "capillary ripples." The alternate case, in which kg is very large

compared to $\frac{\gamma k^3}{\rho}$ is followed by waves referred to as "gravity waves." The gravity term is small for waves on clean water surfaces if the frequency of the waves is above roughly 100 cps.

It is interesting to note how Equations 22' and 22'' compare for situations of experimental interest. Assuming a fluid depth of 1 cm and a wave length of 0.3 cm we have in this unfavorable case that

$$\tanh(kh) = \tanh \frac{6.3}{0.3} = \tanh 21 \quad .$$

where $0.99991 < \tanh 21 < 1$. It should be clear that to a very high degree of approximation the water depth can be taken as infinite.

It is also of interest to try to find an estimate of the effect of the air mass over the surface on the wave propagation velocity dispersion. To do this, one can assume that during the wave motion the air is essentially at rest so that

$$\frac{D\rho_{\text{air}}}{Dt} = 0 \quad . \quad (\text{Eq. 25})$$

To the extent that this is true

$$\text{div } \underline{q}_{\text{air}} = 0 \quad . \quad (\text{Eq. 26})$$

Assuming that the "flow" of air is irrotational and ignoring gravity we find the following equations:

$$\varphi_{\text{air}} = -\eta_0 \frac{\omega}{k} \exp(-ky) \cos(kx - \omega t) \quad (\text{Eq. 27})$$

$$\frac{p_{\text{air}}}{\rho_{\text{air}}} = -\eta_0 \frac{\omega^2}{k} \exp(-ky) \cos(kx - \omega t) \quad . \quad (\text{Eq. 28})$$

We will then find, upon substitution of Equation 28 and the analogous equation calculated from Equation 15' into Equation 20, the result that

$$\omega^2 = \frac{\gamma k^3}{\rho + \rho_{\text{air}}} \quad . \quad (\text{Eq. 29})$$

Since the density of air is about a factor of one thousand smaller than the density of water, the presence of the gas phase will be ignored in subsequent considerations.

Real fluid theory

We now relax the conditions placed on the fluid by recognizing that aqueous systems are viscous. We retain the

incompressibility assumption but we can no longer call the fluid irrotational. The LNS equation is written with the body force assumed to be gravity:

$$\rho \frac{\partial \underline{q}}{\partial t} = -\nabla(p + \rho g y) + \mu \Delta \underline{q} \quad . \quad (\text{Eq. 30})$$

The fluid flow is required to obey the continuity equation which is written for regions without sources or sinks as

$$\frac{\partial \rho}{\partial t} + \text{div} \rho \underline{q} = 0 \quad . \quad (\text{Eq. 31})$$

The stress tensor becomes for an incompressible fluid

$$\sigma_{ij} = -p \delta_{ij} + \mu \left(\frac{\partial q_i}{\partial x_j} + \frac{\partial q_j}{\partial x_i} \right) \quad . \quad (\text{Eq. 32})$$

We note that with $\underline{q} : (u, v, 0)$ and the independence of the motion with z the Equations 30, 31 and 32 become

$$\frac{\partial u}{\partial x} + \frac{\partial v}{\partial y} = 0 \quad (\text{Eq. 33})$$

$$\rho \frac{\partial u}{\partial t} = -\frac{\partial p}{\partial x} + \mu \nabla^2 u \quad (\text{Eq. 34})$$

$$\rho \frac{\partial v}{\partial t} = - \frac{\partial p}{\partial y} - \rho g + \mu \nabla^2 v \quad (\text{Eq. 35})$$

$$\underline{\sigma} = \begin{bmatrix} (-p + 2\mu \frac{\partial u}{\partial x}) & \mu(\frac{\partial u}{\partial y} + \frac{\partial v}{\partial x}) & 0 \\ \mu(\frac{\partial u}{\partial y} + \frac{\partial v}{\partial x}) & (-p + 2\mu \frac{\partial v}{\partial y}) & 0 \\ 0 & 0 & -p \end{bmatrix} \quad (\text{Eq. 36})$$

The entries of the matrix $\underline{\sigma}$ are the components of the stress tensor applying to this system.

Any vector \underline{q} can be represented uniquely to within a constant vector by the sum of a solenoidal vector and the gradient of a potential function, i.e.,

$$\underline{q} = \underline{q}_1 + \underline{q}_2$$

where \underline{q}_1 , \underline{q}_2 satisfy the conditions that

$$\text{curl } \underline{q}_1 = \underline{0}, \quad \text{div } \underline{q}_2 = \underline{0} \quad (\text{Eq. 37})$$

The first condition implies the existence of a function φ such that $\underline{q}_1 = -\nabla\varphi$. Since the smooth flow is to be treated in two dimensions, there exists a function Ψ such

that at each point (x, y) the velocity vector \underline{q}_2 is tangent to the line defined by $\Psi(x, y, t) = \text{constant}$. Time is taken to be a parameter. We can write

$$d\Psi = 0 = \frac{\partial\Psi}{\partial x} dx + \frac{\partial\Psi}{\partial y} dy$$

$$-\frac{dx}{\frac{\partial\Psi}{\partial y}} = \frac{dy}{\frac{\partial\Psi}{\partial x}} \quad (\text{Eq. 38})$$

The condition that \underline{q}_2 is tangent to $\Psi = \text{constant}$ is that

$$\underline{q}_2 \times \frac{d\underline{r}}{dt} = 0 \Rightarrow \frac{dx}{u_2} = \frac{dy}{v_2} \quad (\text{Eq. 39})$$

Equations 38, 39 suggest the definition:

$$u_2 = -\frac{\partial\Psi}{\partial y}$$

$$v_2 = \frac{\partial\Psi}{\partial x} \quad (\text{Eq. 40})$$

That this function leads to a solenoidal vector is demonstrated by noting

$$\text{div } \underline{q}_2 = \frac{\partial u_2}{\partial x} + \frac{\partial v_2}{\partial y} = -\frac{\partial^2 \Psi}{\partial x \partial y} + \frac{\partial^2 \Psi}{\partial x \partial y} = 0$$

providing that Ψ is in C^{11} .

Now the velocity components of \underline{q} can be written as

$$\begin{aligned} u &= -\frac{\partial \varphi}{\partial x} - \frac{\partial \Psi}{\partial y} \\ v &= -\frac{\partial \varphi}{\partial y} + \frac{\partial \Psi}{\partial x} \end{aligned} \quad (\text{Eq. 41})$$

Substituting Equations 41 into Equations 34 and 35 we find

$$\begin{aligned} -\frac{\partial^2 \varphi}{\partial t \partial y} + \frac{\partial^2 \Psi}{\partial t \partial x} &= -\frac{1}{\rho} \frac{\partial p}{\partial y} - g + \frac{\mu}{\rho} \nabla^2 \left(-\frac{\partial \varphi}{\partial y} + \frac{\partial \Psi}{\partial x} \right) \\ -\frac{\partial^2 \varphi}{\partial t \partial x} - \frac{\partial^2 \Psi}{\partial t \partial y} &= -\frac{1}{\rho} \frac{\partial p}{\partial x} + \frac{\mu}{\rho} \nabla^2 \left(-\frac{\partial \varphi}{\partial x} - \frac{\partial \Psi}{\partial y} \right) \end{aligned} \quad (\text{Eq. 42})$$

We note that $\text{div } \underline{q} = \text{div } \underline{q}_1 = -\text{div grad } \varphi = 0 = \nabla^2 \varphi$ under the assumption of incompressibility and uniform density of the fluid. Assuming sufficient continuity of φ , we have

$$\begin{aligned} -\frac{\partial^2 \varphi}{\partial t \partial x} - \frac{\partial^2 \Psi}{\partial t \partial y} &= -\frac{1}{\rho} \frac{\partial p}{\partial x} - \frac{\mu}{\rho} \frac{\partial}{\partial y} (\nabla^2 \Psi) \\ -\frac{\partial^2 \varphi}{\partial t \partial y} + \frac{\partial^2 \Psi}{\partial t \partial x} &= -\frac{1}{\rho} \frac{\partial p}{\partial y} - g + \frac{\mu}{\rho} \frac{\partial}{\partial x} (\nabla^2 \Psi) \end{aligned} \quad (\text{Eq. 43'})$$

These equations will become identities if

$$\frac{\partial \Psi}{\partial t} = \frac{\mu}{\rho} \nabla^2 \Psi$$

and

$$\frac{p}{\rho} = \frac{\partial \phi}{\partial t} - gy \quad . \quad (\text{Eq. 43''})$$

Thus the problem of finding q satisfying Equations 34 and 35 has been transformed to the problem of finding a potential function (ϕ) and a stream function (Ψ) such that

$$\nabla^2 \phi = 0$$

$$\frac{\partial \Psi}{\partial t} = \frac{\mu}{\rho} \nabla^2 \Psi$$

$$\frac{p}{\rho} = \frac{\partial \phi}{\partial t} - gy \quad . \quad (\text{Eq. 44})$$

The capillary ripples are produced experimentally by a T bar lying along the Z axis in periodic motion around $y = 0$ but constrained to move in the Y-Z plane. The waves are propagated toward increasing x with amplitude η . With these facts in mind, we look for potential and stream functions that have the form

$$f(y) \cdot \exp i(\underline{k}x - \omega t) \quad (\text{Eq. 45})$$

where $\underline{k} = k + i\alpha$; α is the damping coefficient sought for comparison with experiment.

Assuming $\varphi = Y_1(y) \exp i(\underline{k}x - \omega t)$ we find that

$$- \underline{k}^2 Y_1(y) + Y_1''(y) = 0 \quad (\text{Eq. 46'})$$

so that $Y_1 = Q \exp(\underline{k}y) + B \exp(-\underline{k}y)$ (Eq. 46'')

and $\varphi(x, y, t) = [Q \exp(\underline{k}y) + B \exp(-\underline{k}y)] \exp i(\underline{k}x - \omega t)$.
(Eq. 47)

Assuming $\Psi = Y_2(y) \exp i(\underline{k}x - \omega t)$ we find from the second of Equations 44 that

$$- i\omega Y_2(y) = \frac{\mu}{\rho} Y_2''(y) - \frac{\mu}{\rho} \underline{k}^2 Y_2(y)$$

defining m^2 as

$$m^2 = \underline{k}^2 - \frac{i\rho\omega}{\mu} \quad (\text{Eq. 48'})$$

we see that

$$\Psi(x, y, t) = [G \exp(my) + D \exp(-my)] \exp i(\underline{k}x - \omega t) .$$

(Eq. 48'')

We assume that the wave motion damps quickly away from the surface so that even in the case of the trough actually used in the experimental part of this research we can impose

the conditions that $\lim_{y \rightarrow -\infty} \varphi(x,y)$, $\lim_{y \rightarrow -\infty} \psi(x,y)$ are both

zero. Providing that the real parts of m and k are positive (as a consequence of the choice of roots in the case of m).

we have that $D = B = 0$. Thus

$$\varphi(x,y,t) = Q \exp(\underline{k}y) \exp i(\underline{k}x - \omega t) \quad (\text{Eq. 49})$$

$$\psi(x,y,t) = G \exp(my) \exp i(\underline{k}x - \omega t) \quad (\text{Eq. 50})$$

Calculating the components of \underline{q} we find:

$$\begin{aligned} u &= - \frac{\partial \varphi}{\partial x} - \frac{\partial \psi}{\partial y} \\ &= [-i\underline{k}Q \exp(\underline{k}y) - Gm \exp(my)] \exp i(\underline{k}x - \omega t) \end{aligned} \quad (\text{Eq. 51})$$

$$\begin{aligned} v &= - \frac{\partial \varphi}{\partial y} + \frac{\partial \psi}{\partial x} \\ &= [i\underline{k}G \exp(my) - \underline{k}Q \exp(\underline{k}y)] \exp i(\underline{k}x - \omega t) \end{aligned} \quad (\text{Eq. 52})$$

$$\frac{p}{\rho} = -i\omega Q \exp(\underline{k}y) \exp i(\underline{k}x - \omega t) - gy \quad (\text{Eq. 53})$$

The vertical and horizontal surface displacements are

calculated by $\dot{\zeta} = v|_{y=0}$ $\dot{\xi} = u|_{y=0}$ where we have assumed that η is sufficiently small to allow $u|_{y=0} = u|_{y=\eta}$ as a first order approximation. We have that

$$\begin{aligned}\dot{\zeta} &= [ikG \exp(my) - kQ \exp(ky)]|_{y=0} \exp i(kx - \omega t) \\ \zeta &= -\frac{k}{\omega} [G + iQ] \exp i(kx - \omega t)\end{aligned}\quad (\text{Eq. 54})$$

$$\begin{aligned}\dot{\xi} &= u|_{y=0} = -[ikQ + Gm] \exp i(kx - \omega t) \\ \xi &= \frac{1}{\omega} [kQ - iGm] \exp i(kx - \omega t)\end{aligned}\quad (\text{Eq. 55})$$

We must next formulate the boundary conditions which will be sufficient to establish a unique solution to the problem. The first boundary condition is purely kinematic. Let $\eta - \eta(x, t) = F(x, y, t) = 0$ be the bounding surface. Then we have that

$$\frac{\partial F}{\partial x} \frac{dx}{dt} + \frac{\partial F}{\partial y} \frac{dy}{dt} + \frac{\partial F}{\partial t} = 0 \quad .$$

Let \underline{v}^* be the velocity of the surface at (x, y) and \underline{v}_n^* be the normal component of the velocity of the surface at (x, y) then

$$\underline{v}_n^* = \frac{\nabla F}{|\nabla F|} \cdot \underline{v}^* = -\frac{\partial F}{\partial t} \cdot$$

The velocity of the fluid particle at the point (x,y) on the surface will be denoted by \underline{q} , its normal component by \underline{q}_n .

Now

$$\underline{q}_n = \frac{\nabla F}{|\nabla F|} \cdot \underline{q} \cdot$$

The boundary condition states that

$$\underline{v}_n^* = \underline{q}_n \quad (\text{Eq. 56})$$

which implies that

$$\frac{\partial F}{\partial t} + u \frac{\partial F}{\partial x} + v \frac{\partial F}{\partial y} = 0$$

or

$$\frac{DF}{Dt} = 0 \quad (\text{Eq. 57})$$

Other boundary conditions are formulated in terms of the continuity of the components of the stress tensor associated with the normal to the free surface. We suppose that the normal to the surface is given to a good approximation by

$$\underline{n} : (0,1,0)$$

so that

$$\underline{\sigma} \underline{n} = \begin{bmatrix} \sigma_{xy} \\ \sigma_{yy} \\ 0 \end{bmatrix}_{y \rightarrow 0^-} \quad (\text{Eq. 58})$$

is the vector expression of the force acting on a unit area of surface. We impose the condition

$$\sigma_{yy}|_{y \rightarrow 0^-} = \gamma \frac{\partial^2 \eta}{\partial x^2} \quad (\text{Eq. 59})$$

on the vertical component of the surface force vector; γ is the surface tension of the system and $\frac{\partial^2 \eta}{\partial x^2}$ the curvature of the surface.

The stress tensor component $\sigma_{xy}|_{y \rightarrow 0^-}$ gives the tangential component of the force per unit area acting on the surface $y = 0$. The problem is to find a satisfactory model for the tangential monolayer forces; such forces, invoking continuity, are to be equated to the stress tensor component, σ_{xy} , evaluated at $y = 0$.

Consider an area A_0 containing n_0 molecules of a surface active agent undergoing dilatation. Assuming that Hooke's law holds and that the viscous force is proportional to the time rate of change of strain, we write

$$\tilde{F} = \tilde{F}_0 + k_e \frac{(A - A_0)}{A_0} + \frac{k_v}{A_0} \frac{dA}{dt}$$

or

$$\tilde{F} = \tilde{F}_0 + k_e \frac{(S - S_0)}{S_0} + \frac{k_v}{S_0} \frac{dS}{dt} \quad . \quad (\text{Eq. 60})$$

S is defined as the area occupied by each molecule, $S = \frac{A}{n}$, k_e is the film elastic constant, k_v is the film viscosity constant, and \tilde{F} is the force exerted on a line one centimeter long lying in the surface. Define Γ , the surface density of surfactant, by the relation $\Gamma = \frac{1}{S}$. Assuming that the dilatation of the surface due to capillary ripples is very small, we can write

$$\begin{aligned} \tilde{F} &= \tilde{F}_0 - \frac{k_e}{\Gamma_0} (\Gamma - \Gamma_0) - \frac{k_v}{\Gamma_0} \frac{d\Gamma}{dt} \\ &= \tilde{F}_0 - K_e (\Gamma - \Gamma_0) - K_v \frac{d\Gamma}{dt} \end{aligned} \quad (\text{Eq. 61})$$

where

$$\begin{aligned} K_e &= \frac{k_e}{\Gamma_0} \\ K_v &= \frac{k_v}{\Gamma_0} \quad . \end{aligned} \quad (\text{Eq. 62})$$

We must next relate the xy component of the stress tensor to the forces produced by local dilatation of the surface during wave passage. Figure 2 shows the nature of the surface forces involved in our model. Initially the forces acting on a line δZ are balanced, Figure 2A, and reflect the equilibrium surface tension of the system. On dilatation, the local change in area represented in Figure 2B by the region $\delta Z \delta x$, will cause a surface tension gradient across the region. The surface film will try to return to the original state resulting in a net force in the negative x direction given by

$$\tilde{F}_1 \delta Z - \Delta \tilde{F} \delta Z - \tilde{F}_1 \delta Z = \left. \frac{\partial \tilde{F}}{\partial x} \right|_{x \in (x_1, x_2)} \delta x \delta Z$$

The net force per unit area must be equal to the stress tensor component, σ_{xy} , evaluated at $y = \eta$ so that we write

$$\left(\sigma_{xy} \Big|_{y \rightarrow \eta^-} \right) \delta x \delta Z = - \left. \frac{\partial \tilde{F}}{\partial x} \right|_{x \in (x_1, x_2)} \delta x \delta Z \quad . \quad (\text{Eq. 63}')$$

Substituting for \tilde{F} , and taking η to be small, we see that (as $\delta x \delta Z$ goes to zero) $\sigma_{xy} \Big|_{y \rightarrow 0^-}$ becomes

$$\sigma_{xy} \Big|_{y \rightarrow 0^-} = \bar{K}_e \frac{\partial \Gamma}{\partial x} + \bar{K}_v \frac{\partial^2 \Gamma}{\partial x \partial t} \quad . \quad (\text{Eq. 63''})$$

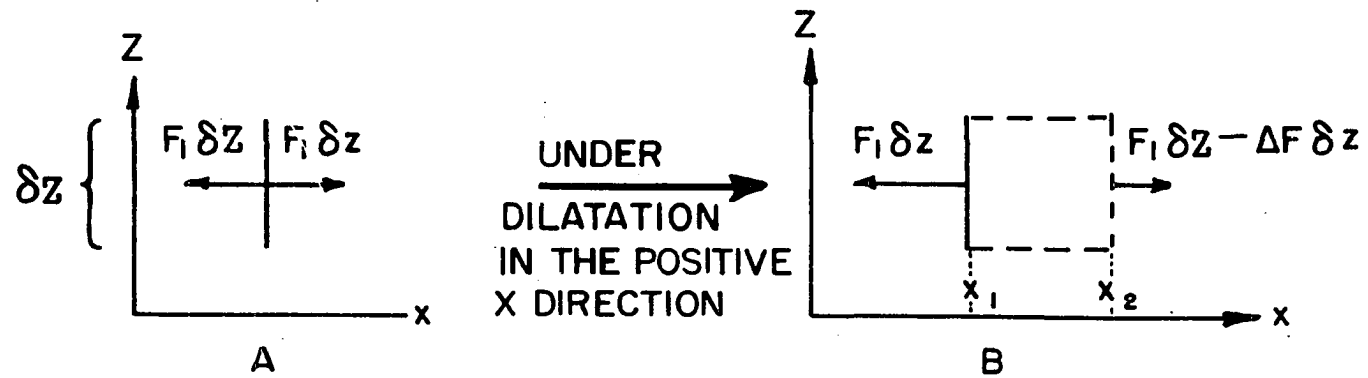


Figure 2. Lateral surface forces

We must also impose the surface continuity equation written in this case for insoluble monolayers;

$$\frac{\partial \Gamma}{\partial t} + \text{div } \Gamma \underline{q} \Big|_{y \rightarrow 0^-} = 0. \quad (\text{Eq. 64})$$

This equation must be solved for Γ in terms of the propagation parameters. If we assume that the concentration variation is due only to horizontal displacements, the boundary value problem can be stated as

$$\frac{\partial \Gamma}{\partial t} = - \Gamma_0 \frac{\partial u}{\partial x} \Big|_{y \rightarrow 0^-}$$

$$\text{subject to } \lim_{x \rightarrow \infty} \Gamma(x, t) = \Gamma_0. \quad (\text{Eq. 65})$$

The linearization of Equation 64 can be discussed in terms of the perturbation theory developed in the introduction of this section. The Γ calculated from Equation 65 should represent the surface density of surfactant to within the first order of approximation.

The function $\frac{\partial u}{\partial x}$ evaluated at $y \rightarrow 0$ is taken from Equation 51.

With

$$u|_{y \rightarrow 0^-} = - [i\underline{k}Q + Gm] \exp i(\underline{k}x - \omega t)$$

$$\frac{\partial u}{\partial x} \Big|_{y \rightarrow 0^-} = - i\underline{k}[i\underline{k}Q + Gm] \exp i(\underline{k}x - \omega t)$$

$$= \underline{k}[\underline{k}Q - iGm] \exp i(\underline{k}x - \omega t) \quad (\text{Eq. 66})$$

we have that

$$\frac{\partial \Gamma}{\partial t} = - \Gamma_0 \underline{k}[\underline{k}Q - iGm] \exp i(\underline{k}x - \omega t)$$

Integration gives

$$\Gamma = - \Gamma_0 \frac{\underline{k}}{\omega} [i\underline{k}Q + Gm] \exp i(\underline{k}x - \omega t)$$

+ constant

but

$$\lim_{x \rightarrow \infty} \exp i(\underline{k}x - \omega t) = \lim_{x \rightarrow \infty} \exp(-\alpha x) \exp i(\underline{k}x - \omega t) = 0$$

so that

$$\Gamma - \Gamma_0 = - \Gamma_0 \frac{\underline{k}}{\omega} [i\underline{k}Q + Gm] \exp i(\underline{k}x - \omega t); \quad (\text{Eq. 67})$$

Equation 63'' thus becomes

$$\sigma_{xy}|_{y \rightarrow 0^-} = -\Gamma_0 \left(i \frac{\bar{K}_e}{\omega} + \bar{K}_v \right) [i \underline{k}^3 Q + \underline{k}^2 G m] \exp i(\underline{k}x - \omega t) \quad .$$

(Eq. 68)

Equation 36 states that

$$\sigma_{xy}|_{y \rightarrow 0^-} = \mu \left[\frac{\partial u}{\partial y} + \frac{\partial v}{\partial x} \right] \Big|_{y \rightarrow 0^-}$$

so that using Equations 51 and 52 we find

$$\sigma_{xy}|_{y \rightarrow 0^-} = -\mu [G(m^2 + \underline{k}^2) + 2i \underline{k}^2 Q] \exp i(\underline{k}x - \omega t) \quad .$$

(Eq. 69)

Equating Equations 68 and 69 we find that

$$\Gamma_0 \left(i \frac{\bar{K}_e}{\omega} + \bar{K}_v \right) [i \underline{k}^3 Q + \underline{k}^2 G m] = +\mu [G(m^2 + \underline{k}^2) + 2i \underline{k}^2 Q] \quad .$$

(Eq. 70)

Using Equations 52, 53 and 54 we solve as follows:

$$\sigma_{yy}|_{y \rightarrow 0^-} = \gamma \frac{\partial^2 \eta}{\partial x^2}$$

and noting that $\eta = \mathcal{J}$, the result of integrating Equation 56, we have that

$$\sigma_{yy}|_{y \rightarrow 0^-} = \frac{\gamma \underline{k}^3}{\omega} [G + iQ] \exp i(\underline{k}x - \omega t) \quad (\text{Eq. 71})$$

but

$$\begin{aligned} \sigma_{yy}|_{y \rightarrow 0^-} &= -p|_{y \rightarrow 0^-} + 2\mu \left(\frac{\partial v}{\partial y} \right) \Big|_{y \rightarrow 0^-} \\ &= \left\{ i\omega \rho Q + 2\mu [i \underline{k} G m - \underline{k}^2 Q] \right\} \exp i(\underline{k}x - \omega t) \end{aligned}$$

so that

$$i\omega \rho Q + 2\mu [i \underline{k} m G - \underline{k}^2 Q] = \frac{\gamma \underline{k}^3}{\omega} [G + iQ] \quad (\text{Eq. 72})$$

Rearranging Equations 70 and 72 we find two homogeneous linear equations in the constants Q and G:

$$\left\{ i \underline{k}^3 \Gamma_0 \left[\frac{i \bar{K}}{\omega} e + \bar{K}_v \right] - 2i \mu \underline{k}^2 \right\} Q + \left\{ \Gamma_0 \left[\frac{i \bar{K}}{\omega} e + \bar{K}_v \right] m \underline{k}^2 - \mu (\underline{k}^2 + m^2) \right\} G = 0 \quad (\text{Eq. 73})$$

and

$$\left\{ i\omega \rho - 2\mu \underline{k}^2 - \frac{i \gamma \underline{k}^3}{\omega} \right\} Q + \left\{ i 2\mu m \underline{k} - \frac{\gamma \underline{k}^3}{\omega} \right\} G = 0 \quad (\text{Eq. 74})$$

At this point in the development of the theory, it is desirable to make several further assumptions concerning the

magnitude of the propagation parameters. Specifically we assume that $(\frac{\alpha}{k})^n$, for $n > 1$, can be ignored when compared to unity. This approximation leads to the following relations:

$$\frac{k}{k} = 1 + i \frac{\alpha}{k} \quad (\text{Eq. 75})$$

$$\begin{aligned} \left(\frac{k}{k}\right)^2 &= 1 - \left(\frac{\alpha}{k}\right)^2 + 2i \frac{\alpha}{k} \\ &\approx 1 + 2i \frac{\alpha}{k} \end{aligned} \quad (\text{Eq. 76})$$

$$\begin{aligned} \left(\frac{k}{k}\right)^3 &= 1 - 3\left(\frac{\alpha}{k}\right)^2 + i\left[3\left(\frac{\alpha}{k}\right) - \left(\frac{\alpha}{k}\right)^3\right] \\ &\approx 1 + 3i \frac{\alpha}{k} \end{aligned} \quad (\text{Eq. 77})$$

The theory would simplify if a proper approximation can be found for m . We proceed as follows:

$$m^2 = \underline{k}^2 - i \frac{\rho\omega}{\mu}$$

$$\left(\frac{m}{k}\right)^2 = \left(\frac{k}{k}\right)^2 - i \frac{\rho\omega}{k^2\mu}$$

$$\left(\frac{m}{k}\right)^2 = 1 - \left(\frac{\alpha}{k}\right)^2 + i\left[2\frac{\alpha}{k} - \frac{\rho\omega}{k^2\mu}\right]$$

$$= r \exp(i\theta)$$

where

$$r = \left| \left(\frac{m}{k}\right)^2 \right|$$

and

$$\tan\theta = \frac{2\frac{\alpha}{k} - \frac{\rho\omega}{k^2\mu}}{1 - \left(\frac{\alpha}{k}\right)^2}$$

$$\left| \tan\theta \right| \geq \left| 2\frac{\alpha}{k} - \frac{\rho\omega}{k^2\mu} \right|$$

Assuming a Kelvin equation fit, $\omega^2 = \frac{\gamma}{\rho} k^3$

$$\left| \tan\theta \right| \geq \left| 2\frac{\alpha}{k} - \frac{\rho}{k^2\mu} \left(\frac{\gamma}{\rho}\right)^{\frac{1}{2}} k^{\frac{3}{2}} \right|$$

$$= \left| 2\frac{\alpha}{k} - \frac{\rho^{\frac{1}{2}}\gamma^{\frac{1}{2}}}{\mu k^{\frac{1}{2}}} \right|$$

$$= \left| 2\frac{\alpha}{k} - 100\left(\frac{\rho\gamma}{k}\right)^{\frac{1}{2}} \right|$$

Assuming a surface tension of 40 d/cm and a wave number of $180 \frac{1}{\text{cm}}$ we have in this unfavorable case that

$$\tan\theta \geq \left| 100 \left(\frac{40}{180} \right)^{\frac{1}{2}} - 0.1 \right|$$

so that

$$\tan\theta \geq 47 .$$

Noting that $2 \frac{\alpha}{k} - \frac{\rho\omega}{k^2\mu} < 0$ and that $1 - \left(\frac{\alpha}{k}\right)^2 > 0$ we conclude that $\theta \approx -\frac{\pi}{2}$. This value for θ implies that

$$\frac{m}{k} = \sqrt{\frac{\rho\omega}{2k^2\mu}} [1 - i] = \sqrt{-i \frac{\rho\omega}{k^2\mu}} . \quad (\text{Eq. 78})$$

We next choose a set of dimensionless groups which will prove useful to the discussion:

$$Z_1 = \frac{\alpha}{k}$$

$$Z_2 = \left(\frac{\Gamma_0}{\gamma}\right) \bar{K}_v \omega = \frac{k_v}{\gamma} \omega$$

$$Z_3 = \left(\frac{\Gamma_0}{\gamma}\right) \bar{K}_e = \frac{k_e}{\gamma}$$

$$Z_4 = \frac{\mu\omega}{\gamma k}$$

$$Z_5 = \sqrt{\frac{\rho\omega}{2k^2\mu}}$$

$$Z_6 = \frac{\omega^2\rho}{k^3\gamma} \quad . \quad (\text{Eq. 79})$$

We should note at this point that two of the groups are degenerate,¹ i.e.,

$$Z_6 = 2Z_5^2 Z_4 \quad .$$

It is useful to retain Z_6 to remind us that the particular group defined by Z_6 is unity if the Kelvin equation holds for the system investigated. Introducing the Z_i dimensionless groups into the approximation equations we find

$$\frac{k}{\bar{k}} = 1 + iZ_1$$

$$\left(\frac{k}{\bar{k}}\right)^2 = 1 + 2iZ_1$$

¹Actually, Z_5 could be defined by

$$Z_5 = \sqrt[4]{\left(1 - \left(\frac{\alpha}{k}\right)^2\right)^2 + \left(2\frac{\alpha}{k} - \frac{\rho\omega}{k^2\mu}\right)^2} \quad .$$

$$\left(\frac{k}{k}\right)^3 = 1 + 3iZ_1$$

$$\frac{m}{k} = Z_5[1 - i] \quad . \quad (\text{Eq. 80})$$

We next put Equation 74 into dimensionless form by dividing through by $\frac{\gamma}{\omega} k^3$:

$$\left\{ i \frac{\omega^2 \rho}{\gamma k^3} - 2 \frac{\mu \omega}{\gamma k} \left(\frac{k}{k}\right)^2 - i \frac{k^3}{k^3} \right\} Q + \left\{ i 2 \frac{\mu \omega}{\gamma k} \frac{m}{k} \frac{k}{k} - \left(\frac{k}{k}\right)^3 \right\} G = 0 \quad .$$

Substituting entries from Equation 80, and the dimensionless groups defined in Equation 79, we find

$$\begin{aligned} & \left\{ iZ_6 - 2Z_4(1 + 2iZ_1) - i(1 + 3iZ_1) \right\} Q \\ & + \left\{ 2Z_4Z_5(1 + i)(1 + iZ_1) - 1 - 3iZ_1 \right\} G = 0 \end{aligned}$$

or

$$\begin{aligned} & \left\{ (3Z_1 - 2Z_4) + i(Z_6 - 1 - 4Z_1Z_4) \right\} Q \\ & + \left\{ [2Z_4Z_5(1 - Z_1) - 1] + i[2Z_4Z_5(1 + Z_1) - 3Z_1] \right\} G = 0 \quad . \end{aligned}$$

$$(\text{Eq. 81})$$

Equation 73 can also be put into dimensionless form by dividing through by $\frac{\gamma k^3}{\omega}$:

$$\left\{ i\omega \frac{\Gamma_0}{\gamma} \left(\frac{k}{k}\right)^3 \left[i \frac{\bar{K}_e}{\omega} + K_v \right] - 2i \frac{\mu\omega}{k\gamma} \left(\frac{k}{k}\right)^2 \right\} Q$$

$$+ \left\{ \frac{\Gamma_0}{\gamma} \omega \left[i \frac{\bar{K}_e}{\omega} + \bar{K}_v \right] \frac{m}{k} \left(\frac{k}{k}\right)^2 - \frac{\mu\omega}{k\gamma} \left[\left(\frac{k}{k}\right)^2 + \left(\frac{m}{k}\right)^2 \right] \right\} G = 0 .$$

We next substitute from Equations 79 to give

$$\left\{ i(1 + 3iZ_1)(iZ_3 + Z_2) - 2iZ_4(1 + i2Z_1) \right\} Q$$

$$+ \left\{ [iZ_3 + Z_2]Z_5[1 - i][1 + i2Z_1] - Z_4(2 + i(4Z_1 - 2Z_5^2)) \right\} G = 0$$

which can be written

$$\left\{ (4Z_1Z_4 - 3Z_1Z_2 - Z_3) + i(Z_2 - 3Z_1Z_3 - 2Z_4) \right\} Q$$

$$+ \left\{ [Z_2Z_5(1 + 2Z_1) + Z_3Z_5(1 - 2Z_1) - 2Z_4] \right.$$

$$\left. + i[Z_3Z_5(1 + 2Z_1) - Z_2Z_5(1 - 2Z_1) - 4Z_1Z_4 + Z_6] \right\} G = 0 .$$

(Eq. 82)

Equations 81 and 82 are linear and homogeneous in two unknown complex constants, Q and G. These two equations

are of the form

$$(a_{11} + ib_{11})Q + (a_{12} + ib_{12})G = 0$$

$$(a_{21} + ib_{21})Q + (a_{22} + ib_{22})G = 0 \quad (\text{Eq. 83})$$

where we take

$$a_{11} = 4Z_1Z_4 - 3Z_1Z_2 - Z_3$$

$$b_{11} = Z_2 - 3Z_1Z_3 - 2Z_4$$

$$a_{12} = Z_2Z_5(1 + 2Z_1) + Z_3Z_5(1 - 2Z_1) - 2Z_4$$

$$b_{12} = Z_3Z_5(1 + 2Z_1) - Z_2Z_5(1 - 2Z_1) - 4Z_1Z_4 + Z_6$$

$$a_{21} = 3Z_1 - 2Z_4$$

$$b_{21} = Z_6 - 1 - 4Z_1Z_4$$

$$a_{22} = 2Z_4Z_5(1 - Z_1) - 1$$

$$b_{22} = 2Z_4Z_5(1 + Z_1) - 3Z_1 \quad (\text{Eq. 84})$$

The necessary and sufficient condition for existence of a non-trivial solution for Equations 83 is that the determinant of the coefficients is zero, i.e.,

$$\begin{vmatrix} a_{11} + ib_{11} & a_{12} + ib_{12} \\ a_{21} + ib_{21} & a_{22} + ib_{22} \end{vmatrix} = 0 \quad . \quad (\text{Eq. 85})$$

This equation can be written as

$$\begin{vmatrix} a_{11} & a_{12} \\ a_{21} & a_{22} \end{vmatrix} - \begin{vmatrix} b_{11} & b_{12} \\ b_{21} & b_{22} \end{vmatrix} + i \begin{vmatrix} a_{11} & a_{12} \\ b_{21} & b_{22} \end{vmatrix} + \begin{vmatrix} b_{11} & b_{12} \\ a_{21} & a_{22} \end{vmatrix} = 0 \quad . \quad (\text{Eq. 86})$$

For this equation to hold, the real part and the imaginary part must each equal zero.

We can handle Equations 83 in another way in order to circumvent calculation of the constants Q and G. Writing $Q = Q' + iQ''$ and $G = G' + iG''$ we see that

$$a_{11}Q' - b_{11}Q'' + a_{12}G' - b_{12}G'' = 0$$

$$b_{11}Q' + a_{11}Q'' + b_{12}G' + a_{12}G'' = 0$$

$$a_{21}Q' - b_{21}Q'' + a_{22}G' - b_{22}G'' = 0$$

$$b_{21}Q' + a_{21}Q'' + b_{22}G' + a_{22}G'' = 0 \quad . \quad (\text{Eq. 87})$$

The necessary and sufficient condition for existence of a non-trivial solution of Equations 86 is that the determinant of the coefficients¹ is zero, i.e.,

$$\begin{vmatrix} a_{11} & -b_{11} & a_{12} & -b_{12} \\ b_{11} & a_{11} & b_{12} & a_{12} \\ a_{21} & -b_{21} & a_{21} & -b_{22} \\ b_{21} & a_{21} & b_{22} & a_{22} \end{vmatrix} = 0 \quad . \quad (\text{Eq. 88})$$

It is not transparent that Equations 86 and 88 are equivalent. Suppose we let

¹Note that these coefficients are real.

$$a_1 = a_{11} + ib_{11}$$

$$a_2 = a_{12} + ib_{12}$$

$$a_3 = a_{21} + ib_{21}$$

$$a_4 = a_{22} + ib_{22} \quad . \quad (\text{Eq. 89})$$

The complex conjugate of these quantities will be written a_i^* . First multiply column 2 (Equation 88) by $-i$ and add to column 1, then multiply column 4 by $-i$ and add to column 3. Next multiply row 1 by i and add to row 2, then multiply row 3 by i and add to row 4. Equation 88 will transform under these operations to

$$\begin{vmatrix} a_1 & -b_{11} & a_2 & -b_{12} \\ 0 & a_1^* & 0 & a_2^* \\ a_3 & -b_{21} & a_4 & -b_{22} \\ 0 & a_3^* & 0 & a_4^* \end{vmatrix} = 0. \quad (\text{Eq. 90})$$

Expanding we find that

$$a_1 a_4 \begin{vmatrix} a_1^* & a_2^* \\ a_3^* & a_4^* \end{vmatrix} - a_2 a_3 \begin{vmatrix} a_1^* & a_2^* \\ a_3^* & a_4^* \end{vmatrix} = 0$$

or

$$\begin{vmatrix} a_1 & a_2 \\ a_3 & a_4 \end{vmatrix} \cdot \begin{vmatrix} a_1^* & a_2^* \\ a_3^* & a_4^* \end{vmatrix} = 0 \quad (\text{Eq. 91'})$$

We must have that one or both of the 2 x 2 determinants in Equation 91' is zero; in fact both are zero as expansion of each 2 x 2 determinant into real and imaginary parts will show.

It might appear that we have lost some information in using Equation 88 since Equation 86 requires both the real and imaginary parts of this equation to be zero thus giving two equations which must be satisfied together while Equation 88 stands alone. However if we write

$$\begin{vmatrix} a_1 a_2 \\ a_3 a_4 \end{vmatrix} = A' + iA''$$

then Equation 91' reads

$$(A')^2 + (A'')^2 = 0 \quad (\text{Eq. 91''})$$

which holds iff

$$A' = 0$$

$$A'' = 0$$

Indeed, Equations 86 and 88 are equivalent.

To conclude this section of the theory, we must point out that portions of the hydrodynamical theory expounded here have been discussed by others. The viewpoint from which we develop the theory is our own. Our handling of the visco-elastic parameters is, to our knowledge, new. Our use of dimensionless groups is also new.

The application of this theory to our experimental results will be discussed in a later section of This Thesis.

Soluble Monolayer Case

Basic assumptions

A number of assumptions are to be carried throughout this section:

- i) The surface active compound (surfactant) is positive-adsorbed at the air-liquid interface; the surface layer is always in a state of statistical equilibrium with the adjacent subsurface

layer of the volume solution.

- ii) The solution is dilute.
- iii) The interactions between surface layer molecules are weak so that surface viscosity parameter, k_v , can be neglected.

As the theory develops, assumptions will be made concerning the degree of approximation to be carried in the calculation. Order symbols will usually be used to indicate behavior of series expansion remainder terms. To review, $f(x) = O(q[x])$ reads that there is a positive real number M such that

$$\left| \frac{f(x)}{q(x)} \right| < M$$

for all x in some specified domain.

Preliminary considerations

Waves generated on a liquid surface will cause local periodic variations of the surface area resulting in local periodic variations in the surface concentration of the surfactant. In the insoluble monolayer case, the total number of surfactant molecules confined to the surface of given area remains constant with time although the waves will cause local concentration changes. In this case, the two dimension continuity equation holds:

$$\frac{\partial \Gamma}{\partial t} + \text{div} \Gamma \underline{q} = 0 \quad .$$

Γ is independent of the volume surfactant concentration.

In the case of soluble films, the total number of surfactant molecules confined to the surface of given area varies periodically with time; the nature of the concentration variations will depend upon the volume concentration of the surfactant. The functional relationship between Γ and C , the surface concentration and the volume concentration of the surfactant, will reflect the model chosen to represent the adsorption-desorption process. This section treats the diffusion control model.

Theory

Define Γ_0 as the surface concentration of the undeformed surface and $\Gamma' (= \Gamma - \Gamma_0)$ as the total change in surface concentration due to deformation. Let C_0 and C' ($= C - C_0$) denote the volume solution concentration and the volume solution concentration change due to the diffusion of the substrate surfactant molecules to the surface as the result of surface deformation.

At equilibrium, it is necessary for the chemical potential of the surfactant in the subsurface layer to equal the chemical potential of the surfactant in the surface layer. Assuming sufficiently small surface deformations so that the

chemical potential changes are infinitesimal, we expand the chemical potential functions in terms of r' and C' ignoring terms of $O(r'^2)$ and $O(C'^2)$:

$$\mu_s(r') = \mu_s(0) + \left. \frac{\partial \mu_s}{\partial r} \right|_{r_0} r'$$

$$\mu_v(C') = \mu_v(0) + \left. \frac{\partial \mu_v}{\partial C} \right|_{C_0} C' .$$

Asserting basic assumption i),

$$\left. \left(\frac{\partial \mu_s}{\partial r} \right) \right|_{r_0} r' = \left. \left(\frac{\partial \mu_v}{\partial C} \right) \right|_{C_0} C'_{y \rightarrow 0^-}$$

and so

$$r' = \frac{\left. \left(\frac{\partial \mu_v}{\partial C} \right) \right|_{C_0}}{\left. \left(\frac{\partial \mu_s}{\partial r} \right) \right|_{r_0}} C'_{y \rightarrow 0^-} . \quad (\text{Eq. 92})$$

Basic assumption ii) allows us to write

$$\mu_v = RT \log C + f(P, T)$$

so that

$$\Gamma' = \frac{RT}{C_0} \frac{1}{\left(\frac{\partial \mu_s}{\partial \Gamma}\right)_{\Gamma_0}} C'_{y \rightarrow 0^-} \quad (\text{Eq. 93})$$

The continuity equation written in the previous section must now include a term reflecting the diffusion process occurring at the interface. The Fick's law flux will be written as

$$D \frac{\partial C'}{\partial y} \Big|_{y \rightarrow 0^-} .$$

The linearized surface continuity equation, with the addition of the source-sink term, becomes

$$\frac{\partial \Gamma'}{\partial t} + \Gamma' \frac{\partial \mu}{\partial x} \Big|_{y \rightarrow 0^-} + D \left(\frac{\partial C'}{\partial y} \right)_{y \rightarrow 0^-} = 0 .$$

Since $\Gamma' \ll \Gamma_0$ and $\Gamma' = \Gamma - \Gamma_0$,

$$\frac{\partial \Gamma'}{\partial t} + \Gamma_0 \frac{\partial \mu}{\partial x} \Big|_{y \rightarrow 0^-} + D \left(\frac{\partial C'}{\partial y} \right)_{y \rightarrow 0^-} = 0 . \quad (\text{Eq. 94})$$

To determine the diffusion flux from the volume solution, it is necessary to solve the diffusion equation subject to the boundary conditions, Equations 93 and 94. It is convenient

to introduce the equations of motion and its boundary conditions at this point of the discussion. The full boundary value problem becomes after substitution of Equation 93 into Equation 94:

$$\frac{\partial C'}{\partial t} = D \left(\frac{\partial^2 C'}{\partial x^2} + \frac{\partial^2 C'}{\partial y^2} \right); \quad 0 < x < +\infty, \quad -\infty < y < 0 \quad (\text{Eq. 95})$$

$$\frac{RT}{C_0} \frac{1}{\left(\frac{\partial \mu_s}{\partial r} \right) \Gamma_0} \left[\frac{\partial C'}{\partial t} \right]_{y \rightarrow 0^-} = - \Gamma_0 \frac{\partial u}{\partial x} \Big|_{y \rightarrow 0^-} - D \left(\frac{\partial C'}{\partial y} \right)_{y \rightarrow 0^-} \quad (\text{Eq. 96})$$

$$\frac{\partial \underline{q}}{\partial t} = - \frac{1}{\rho} \nabla p + \frac{\mu}{\rho} \nabla^2 \underline{q} \quad (\text{Eq. 97})$$

$$\sigma_{yy} \Big|_{y \rightarrow 0^-} = \frac{\partial^2 \underline{z}}{\partial x^2} \quad (\text{Eq. 98})$$

$$\sigma_{xy} \Big|_{y \rightarrow 0^-} = \bar{K}_e \frac{\partial \Gamma'}{\partial x} \quad (\text{Eq. 99})$$

Equation 99 deserves some discussion. Basic assumption iii) implies that the surface viscosity parameter k_v in Equation 60 of the previous section should be very small. It is taken to be zero. The remaining term contributing to the

force balance across an element of surface area must reflect the thermodynamic compressibility of the film. The thermodynamic compressibility of a surface film is defined by

$$\beta = - \frac{1}{A} \frac{\partial A}{\partial \pi} = + \frac{\partial \log A}{\partial \gamma} .$$

By definition

$$\Gamma = \frac{n}{A}$$

and with area considered as the independent variable, keeping n constant, we have

$$d \log \Gamma = - d \log A$$

so that

$$\beta = - \frac{\partial \log \Gamma}{\partial \gamma} \approx - \frac{1}{\Gamma_0} \frac{\partial \Gamma'}{\partial \gamma} . \quad (\text{Eq. 100})$$

Using an approach based on thermodynamics, Levich (29) derived the following relation for the surface component of the stress tensor.

$$\sigma_{xy} \Big|_{y \rightarrow 0^-} = - \frac{E_0}{\nu_0} \frac{\partial \nu'}{\partial x} . \quad (\text{Eq. 101})$$

E_0 is identified as the "Two dimensional compressibility modulus of the film"; ν is identical to our Γ . We note then

that

$$\bar{K}_e = - \frac{E_o}{r_o} . \quad (\text{Eq. 102})$$

In this case, \bar{K}_e might be identified as $+\frac{1}{\beta r_o}$. However, the point is that \bar{K}_e will be constant over the frequency range investigated and it will be proportional to the thermodynamic film compressibility. Relaxation frequencies for water dipole or heptanoic acid dipole reorientation lie orders of magnitude above the high frequency limit of the present instrumentation.

Equation 97 has the following solution (Equations 51 and 52 of the previous section):

$$u = \frac{\partial \mathcal{F}}{\partial t} = [-i \underline{k} Q \exp(\underline{k}y) - Gm \exp(my)] \exp i(\underline{k}x - \omega t) \quad (\text{Eq. 103})$$

$$v = \frac{\partial \mathcal{F}}{\partial t} = [i \underline{k} G \exp(my) - \underline{k} Q \exp(\underline{k}y)] \exp i(\underline{k}x - \omega t) \quad (\text{Eq. 104})$$

where

$$m^2 = \underline{k}^2 - \frac{i\rho\omega}{\mu} \quad (\text{Eq. 105})$$

and $\underline{k} = k + i\alpha$, with k as the propagation constant and α as the damping coefficient.

We seek a solution to Equations 95 and 96 having the following form:

$$C' = B \cdot f(y) \cdot \exp i(\underline{k}x - \omega t) \quad .$$

Substituting this equation into Equation 95, we find

$$\begin{aligned} & - i\omega B f(y) \exp i(\underline{k}x - \omega t) \\ & = D[- \underline{k}^2 B f(y) + B f''(y)] \exp i(\underline{k}x - \omega t) \quad . \end{aligned}$$

Rearranging yields

$$f''(y) - \left(\underline{k}^2 - \frac{i\omega}{D} \right) f(y) = 0 \quad .$$

The solution having the property $\lim_{y \rightarrow -\infty} f(y) = 0$ is

$$f(y) = \bar{B} \exp\left(\underline{k}^2 - \frac{i\omega}{D}\right)^{\frac{1}{2}} y \quad .$$

The expression for the concentration change at any point in the solution becomes

$$C' = B \exp\left(\underline{k}^2 - \frac{i\omega}{D}\right)^{\frac{1}{2}} y \exp i(\underline{k}x - \omega t) \quad . \quad (\text{Eq. 106})$$

Next, the constant B must be determined by substitution into Equation 96:

$$\frac{RT}{C_0} \frac{-i\omega B}{\left(\frac{\partial \mu_s}{\partial r}\right) r_0} = i r_0 k (ikQ + Gm) - D(k^2 - i\frac{\omega}{D})^{\frac{1}{2}} B$$

so that

$$B = \frac{i r_0 k (ikQ + Gm)}{D(k^2 - i\frac{\omega}{D})^{\frac{1}{2}} - \frac{RT}{C_0} \frac{i\omega}{\left(\frac{\partial \mu_s}{\partial r}\right) r_0}} \quad (\text{Eq. 107})$$

then

$$C' = \frac{i r_0 k (ikQ + Gm)}{D(k^2 - i\frac{\omega}{D})^{\frac{1}{2}} - \frac{RT}{C_0} \frac{i\omega}{\left(\frac{\partial \mu_s}{\partial r}\right) r_0}} \exp(k^2 - i\frac{\omega}{D})^{\frac{1}{2}} y \exp i(kx - \omega t) \quad (\text{Eq. 108})$$

Equation 93 then becomes

$$r' = \frac{RT}{C_0} \frac{1}{\left(\frac{\partial \mu_s}{\partial r}\right) r_0} \frac{i r_0 k (ikQ + Gm) \exp i(kx - \omega t)}{D(k^2 - i\frac{\omega}{D})^{\frac{1}{2}} - \frac{RT}{C_0} \frac{i\omega}{\left(\frac{\partial \mu_s}{\partial r}\right) r_0}}$$

$$= \frac{-\Gamma_o \frac{k}{\omega} (Gm + ikQ) \exp i(\underline{k}x - \omega t)}{1 + i \frac{C_o D}{RT\omega} \left(\frac{\partial \mu_s}{\partial r}\right) \Gamma_o (\underline{k}^2 - i\frac{\omega}{D})^{\frac{1}{2}}} \quad (\text{Eq. 109})$$

The stress tensor component, $\sigma_{xy}|_{y \rightarrow 0^-}$, is now written as

$$\begin{aligned} \sigma_{xy}|_{y \rightarrow 0^-} &= \frac{-i\bar{K}_e \Gamma_o \frac{k^2}{\omega} (Gm + ikQ) \exp i(\underline{k}x - \omega t)}{1 + i \frac{C_o D}{RT\omega} \left(\frac{\partial \mu_s}{\partial r}\right) \Gamma_o (\underline{k}^2 - i\frac{\omega}{D})^{\frac{1}{2}}} \\ &= \frac{\bar{K}_e \Gamma_o \frac{k^2}{\omega} (\underline{k}Q - iGm) \exp i(\underline{k}x - \omega t)}{1 + i \frac{C_o D}{RT\omega} \left(\frac{\partial \mu_s}{\partial r}\right) \Gamma_o (\underline{k}^2 - i\frac{\omega}{D})^{\frac{1}{2}}} \end{aligned} \quad (\text{Eq. 110})$$

An independent expression for the stress tensor component σ_{xy} is given by Equation 69 of the previous section. Equating, we find that

$$\frac{(\underline{k}Q - iGm)}{(\bar{K}_e \Gamma_o \frac{k^2}{\omega})^{-1} \left[1 + i \frac{C_o D}{RT\omega} \left(\frac{\partial \mu_s}{\partial r}\right) \Gamma_o (\underline{k}^2 - i\frac{\omega}{D})^{\frac{1}{2}}\right]}$$

$$= -\mu[(m^2 + \underline{k}^2)G + 2i\underline{k}^2Q] .$$

Thus

$$\left\{ \frac{\underline{k}}{(\bar{K}_e \Gamma_o \frac{k^2}{\omega})^{-1} [1 + i \frac{C_o D}{RT\omega} (\frac{\partial \bar{\mu}_s}{\partial \Gamma}) \Gamma_o (\underline{k}^2 - i \frac{\omega}{D})^{\frac{1}{2}}]} + 2i\mu \underline{k}^2 \right\} Q$$

$$+ \left\{ \mu(m^2 + \underline{k}^2) - \frac{im}{(\bar{K}_e \Gamma_o \frac{k^2}{\omega})^{-1} [1 + i \frac{C_o D}{RT\omega} (\frac{\partial \bar{\mu}_s}{\partial \Gamma}) \Gamma_o (\underline{k}^2 - i \frac{\omega}{D})^{\frac{1}{2}}]} \right\} G = 0 .$$

(Eq. 111)

From Equation 72 of the previous section, we have that

$$[-2\mu \underline{k}^2 + i(\omega\rho - \frac{k^3}{\omega})]Q + [-\frac{\gamma k^3}{\omega} + i2\mu \underline{k}m]G = 0 . \quad (\text{Eq. 112})$$

The constants Q and C will be eliminated by the arguments developed in the previous section.

We note that the quantity $(\underline{k}^2 - i \frac{\omega}{D})^{\frac{1}{2}}$ appears in Equation 111. We use the following representation:

$$\underline{k}^2 - i \frac{\omega}{D} = k^2 - \alpha^2 + i(2k\alpha - \frac{\omega}{D})$$

$$= r_1 \exp(i\theta_1)$$

where

$$r_1 = \sqrt{(k^2 - \alpha^2)^2 + (2k - \frac{\omega}{D})^2}$$

$$\tan\theta_1 = \frac{2k\alpha - \frac{\omega}{D}}{k^2 - \alpha^2} \quad (\text{Eq. 113})$$

so that

$$(\underline{k}^2 - i\frac{\omega}{D})^{\frac{1}{2}} = r_1^{\frac{1}{2}} \exp(i\frac{\theta_1}{2}) = r_1^{\frac{1}{2}} (\cos \frac{\theta_1}{2} + i \sin \frac{\theta_1}{2}) .$$

(Eq. 114)

Rather than go through the considerable labor of expanding Equations 111 and 112 into real and imaginary parts using Equations 105 and 114 and the definition of the complex wave number, \underline{k} , we make a number of assumptions about the magnitude of various quantities. $(\frac{\alpha}{k})^n$, which is experimentally of the order of $(5 \times 10^{-2})^n$, is to be considered small compared to one for $n > 1$. This approximation implies that we can again take

$$\frac{k}{k} = 1 + i\frac{\alpha}{k}$$

$$\frac{k^2}{k^2} = 1 + 2i\left(\frac{\alpha}{k}\right)$$

$$\frac{k^3}{k^3} = 1 + 3i\left(\frac{\alpha}{k}\right) \quad (\text{Eq. 115})$$

Consider the approximation valid for Equation 114:

$$\left| \tan\theta_1 \right| > \left| \frac{2\alpha k - \frac{\omega}{D}}{k^2} \right| = \left| 2\frac{\alpha}{k} - \frac{\omega}{k^2 D} \right|.$$

In the most unfavorable case, we have that $|\tan\theta_1| > 10^3$. Since $2\alpha k - \frac{\omega}{D} < 0$, and $k^2 > 0$, we have that $\theta_1 = -\frac{\pi}{2}$. This implies that

$$\begin{aligned} \left(\underline{k}^2 - i\frac{\omega}{D} \right)^{\frac{1}{2}} &\approx \left(\frac{\omega}{2D} \right)^{\frac{1}{2}} [1 - i] \\ &= \sqrt{-i\frac{\omega}{D}} \quad (\text{Eq. 116}) \end{aligned}$$

Referring to Equation 78 of the previous section we write

$$m = \sqrt{\frac{\rho\omega}{2\mu}} [1 - i] \quad . \quad (\text{Eq. 117})$$

We wish to introduce a set of dimensionless groups:

$$Z_1 = \frac{\alpha}{k}$$

$$Z_3 = \frac{\Gamma_0}{\gamma} \bar{K}_e = \frac{k_e}{\gamma}$$

$$Z_4 = \frac{\mu\omega}{\gamma k}$$

$$Z_5 = \sqrt{\frac{\rho\omega}{2\mu k^2}}$$

$$Z_6 = \frac{\omega^2 \rho}{k^3 \gamma} = 2Z_5^2 Z_4$$

$$Z_7 = \frac{C_0 D}{RT} \left(\frac{\partial \mu_s}{\partial r} \right) r_0 \sqrt{\frac{1}{2\omega D}} \quad . \quad (\text{Eq. 118})$$

We note that Z_6 is not independent. However if the Kelvin equation is obeyed for capillary ripples then $Z_6 = 1$; again Z_6 serves as a reminder for us to note terms that simplify under this assumption. This set differs from the groups listed in the previous section only in that Z_2 is missing and Z_7 is added to carry the diffusion terms. With these definitions in mind, Equations 115 and 117 become:

$$\frac{k}{\bar{k}} = 1 + iZ_1$$

$$\left(\frac{k}{\bar{k}}\right)^2 = 1 + 2iZ_1$$

$$\left(\frac{k}{\bar{k}}\right)^3 = 1 + 3iZ_1$$

$$\frac{m}{k} = Z_5[1 - i] \quad . \quad (\text{Eq. 119})$$

Substituting these approximations into Equation 111 and dividing through by k^3 , we have:

$$\left\{ \frac{\bar{K} e^{\Gamma_0} \frac{k}{\bar{k}}}{w} \left(\frac{k}{\bar{k}}\right)^3 [(1 + Z_7) - iZ_7] + 2\frac{i\mu}{k} \left(\frac{k}{\bar{k}}\right)^2 \right\} Q$$

$$+ \left\{ \frac{\mu}{k} \left[\left(\frac{m}{k}\right)^2 + \left(\frac{k}{\bar{k}}\right)^2 \right] - \frac{i\bar{K} e^{\Gamma_0} \left(\frac{k}{\bar{k}}\right)^2 \left(\frac{m}{k}\right) [(1 + Z_7) - iZ_7]}{[(1 + Z_7)^2 + (Z_7)^2]} \right\} G = 0 \quad .$$

Multiplying through by $\frac{w}{\gamma}$ gives the result:

$$\left\{ \frac{Z_3 \left(\frac{k}{\bar{k}}\right)^3 [(1 + Z_7) - iZ_7]}{(1 + Z_7)^2 + (Z_7)^2} + 2iZ_4 \left(\frac{k}{\bar{k}}\right)^2 \right\} Q$$

$$+ \left\{ z_4 \left[\left(\frac{m}{k} \right)^2 + \left(\frac{k}{k} \right)^2 \right] - \frac{i z_3 \left(\frac{k}{k} \right)^2 \left(\frac{m}{k} \right) [(1 + z_7) - i z_7]}{(1 + z_7)^2 + (z_7)^2} \right\}_G = 0 .$$

We notice that this last equation is dimensionless. We also see that

$$\left(\frac{m}{k} \right)^2 + \left(\frac{k}{k} \right)^2 = 2 \left(\frac{k}{k} \right)^2 - i \frac{\rho \omega}{\mu k^2}$$

$$\cong 2 + i[4z_1 - 2z_5^2] .$$

so that

$$\left\{ \frac{z_3(1 + 3iz_1)[(1 + z_7) - iz_7]}{(1 + z_7)^2 + (z_7)^2} + 2iz_4(1 + 2iz_1) \right\}_Q$$

$$+ \left\{ 2z_4 + i[4z_1z_4 - 2z_5^2z_4] \right.$$

$$\left. - \frac{z_3(1 + 2iz_1)z_5[1 + i][(1 + z_7) - iz_7]}{(1 + z_7)^2 + (z_7)^2} \right\}_G = 0 .$$

Multiplying the complex terms together and collecting into real and imaginary parts, we find:

$$\begin{aligned}
& \left\{ \left[\frac{z_3 [1 + z_7 (1 + 3z_1)]}{(1 + z_7)^2 + (z_7)^2} - 4z_1 z_4 \right] \right. \\
& + i \left[\frac{z_3 [3z_1 (1 + z_7) - z_7]}{(1 + z_7)^2 + (z_7)^2} + 2z_4 \right] \left. \right\} Q \\
& + \left\{ \left[- \frac{z_3 z_5 (1 - 2z_1 + 2z_7)}{(1 + z_7)^2 + (z_7)^2} + 2z_4 \right] \right. \\
& + i \left[- \frac{z_3 z_5 (2z_1 + 4z_1 z_7 + 1)}{(1 + z_7)^2 + (z_7)^2} \right. \\
& \left. \left. + 4z_1 z_4 - 2z_5^2 z_4 \right] \right\} G = 0 \quad . \quad (\text{Eq. 120})
\end{aligned}$$

Equation 112, as shown in the previous section, transforms to the dimensionless equation:

$$\begin{aligned}
& [(3z_1 - 2z_4) + i(z_6 - 4z_4 z_1 - 1)] Q \\
& + [(2z_4 z_5 (1 - z_1) - 1) + i(2z_4 z_5 (1 + z_1) - 3z_1)] G = 0 \quad .
\end{aligned}$$

(Eq. 121)

Recalling the form of Equation 83 in the previous section we have that

$$a_{11} = \frac{z_3(1 + z_7(1 + 3z_1))}{(1 + z_7)^2 + (z_7)^2} - 4z_1z_4$$

$$b_{11} = \frac{z_3(3z_1(1 + z_7) - z_7)}{(1 + z_7)^2 + (z_7)^2} + 2z_4$$

$$a_{12} = \frac{z_3z_5(2z_1 - 1 - 2z_7)}{(1 + z_7)^2 + (z_7)^2} + 2z_4$$

$$b_{12} = -\frac{z_3z_5(2z_1 + 4z_1z_7 + 1)}{(1 + z_7)^2 + (z_7)^2} + 4z_1z_4 - z_6$$

$$a_{21} = 3z_1 - 2z_4$$

$$b_{21} = z_6 - 4z_1z_4 - 1$$

$$a_{22} = 2z_4z_5(1 - z_1) - 1$$

$$b_{22} = 2z_4z_5(1 + z_1) - 3z_1 \quad . \quad (\text{Eq. 122})$$

The discussion in the previous section centering around Equations 81 and 82 applies to the situation expressed in Equations 30 and 31. The numerical procedures used to calculate the damping coefficient, α , through the calculation of Z_1 , are given in the next section.

We wish to point out that the fundamental idea of the diffusion control theory, the functional form expressing the assumption of equilibrium between the subsurface layer and surface layer, was due to Levich (29). Our point of view was somewhat different; we solved the problem for forced wave motion, $\underline{k} = k + i\alpha$, while he viewed the problem in terms of free oscillations, $\underline{\omega} = \beta \pm i\omega$. Our use of dimensionless groups is original.

EXPERIMENTAL

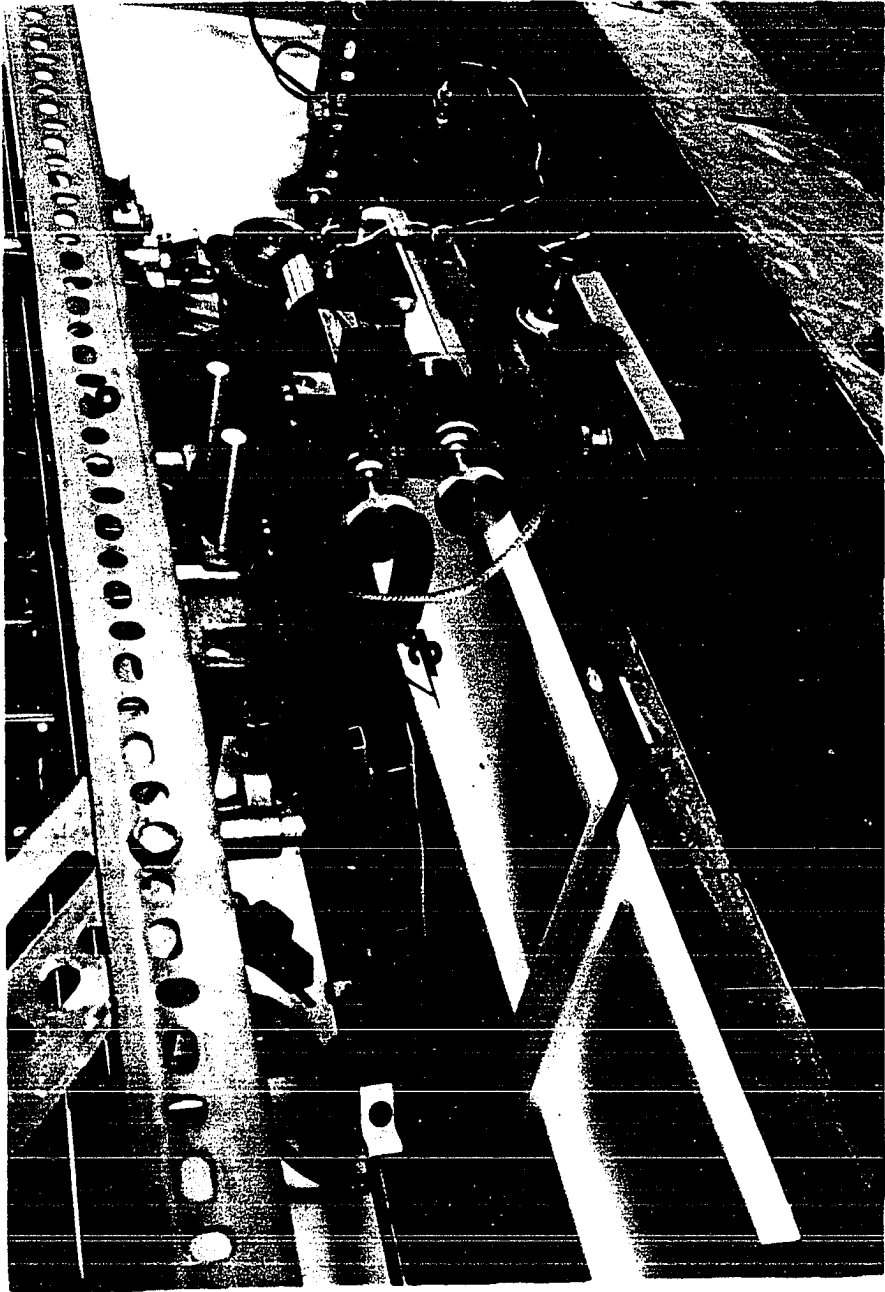
The instrumentation for the measurement of surface viscoelastic phenomena has passed through two distinct phases in this laboratory. We first built a recording surface balance of the Langmuir type along with the associated constant temperature chamber. We subsequently designed and built the various components of the ripple generator and receiver. In this section we will describe the automatic recording surface balance, the air thermostat, the ripple generator, and the ripple receiving instrument. We will also discuss the form of the data collected in measuring the propagation constants of capillary ripples, and the data processing necessary to obtain propagation velocity and attenuation coefficient dispersion curves.

Automatic Surface Balance

The prototype of the automatic surface balance now in use in our laboratory was described in a recent paper by Mann and Hansen (30). While the operation principles remain unchanged, we have modified many of the details of that first balance. Figure 3 is a labeled photograph of the present surface balance and associated equipment.

Figure 3. View of surface balance and ripple analyzer

1. Teflon trough
2. Teflon moving barrier mounted on transport system
3. Receiving and sending probes positioned for use
4. Micromanipulator
5. Torsion balance
6. Dexion frame supporting sending probe
7. Base plate on top of rubber strips for vibration control



The trough

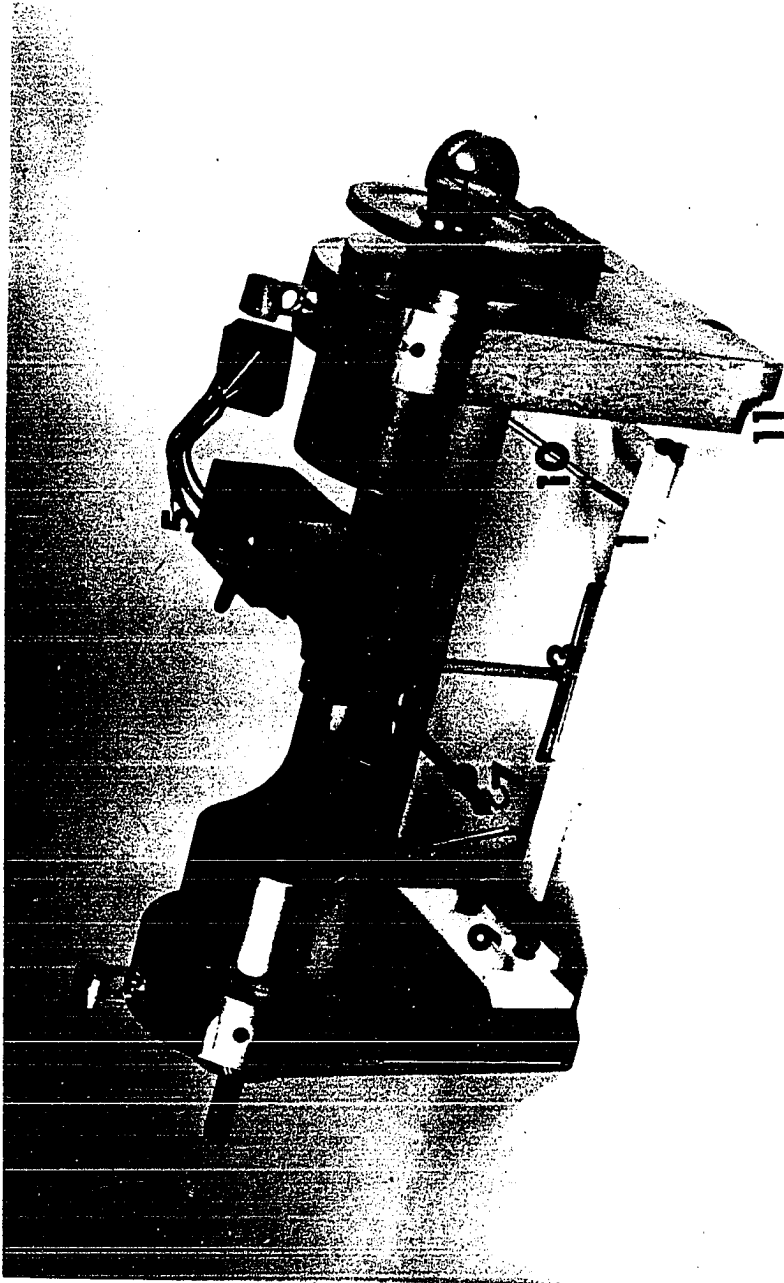
The trough was made of a single piece of milled teflon with dimensions roughly 2.5 cm x 18 cm x 70 cm. A channel was milled around the sides of a teflon slab to allow firm clamping of the slab to a $\frac{3}{8}$ -inch brass plate. Low walls were soldered to the edge of the base plate to hold solutions spilled from the trough during surface sweeping operations. The trough height and level were adjusted with three pointed bolts turning through drilled and tapped brass blocks soft soldered to the ends of the base plate to form a triangular support. The teflon slab, clamped to the base plate, was then milled to form a 1.5 cm deep trough with side walls approximately 1.3 cm thick. The trough was released from the base plate by loosening screws which clamped brass strips between the base plate and the slot milled around the sides of the teflon trough. The trough alone was cleaned by immersion in a hot, 1:1 mixture of HNO_3 and H_2SO_4 . When the trough was clean, the water contact angle was greater than 90° and the hot HNO_3 - H_2SO_4 mixture would not wet the teflon.

The torsion balance

The film pressure sensing device, the "torsion balance," is shown in Figure 4. A teflon float, labeled 1 in Figure 4, was coupled to the torsion wire, 2, by a three pronged fork

Figure 4. Torsion balance

1. Teflon float
2. Torsion wire
3. Fork coupling barrier to torsion balance
4. LVDT core is attached to end of this bar
5. LVDT
6. Calibration arm of Tee
7. Calibration weight hook
8. One of two teflon ribbons
9. Teflon side pieces
10. Platinum wire barrier supports
11. Relief milled shoulders to fit trough



arrangement, 3. The prongs of the fork were cut from platinum wire and soldered to the brass cross-bar. A bar, 4, perpendicular to the fork and the float at the torsion wire was coupled to the core of a 0.033 inch travel Linear Variable Differential Transformer (LVDT), 5, manufactured by the Schaevitz Co. A force perpendicular to the float was resisted by the torsion wire so that the float displacement was directly proportional to the magnitude of the force. Float movement caused a displacement of the LVDT core which changed the level of the output from the LVDT secondary coils by an amount proportional to the displacement of the float. The A.C. output from the LVDT secondary coil was then rectified and read out on the y axis of an x - y recorder. The recorder pen displacement was calibrated in terms of the force acting on one centimeter of the barrier. The third arm of the Tee, 6, was designed to expedite the calibration procedure. Since the distances from the float, 1, to the torsion wire, 2, and from the torsion wire, 2, to the calibration weight hook, 7, were known, and in fact equal, weights hung from this hook represented forces applied against the barrier. The recorder span was adjusted so that convenient chart increments would correspond to 10, 20, . . . dynes/cm as calculated from

$$\bar{F} = \frac{(980.5)m}{L} \quad (\text{Eq. 1})$$

where \bar{F} is the force applied per centimeter of equivalent barrier length, m is the mass of the calibration weight and L is the equivalent length¹ of the barrier. The barrier was attached to the sides of the torsion head by two 3 mil teflon ribbons, 8, cut from teflon standard taper sleeves. The ribbons were attached to the thicker teflon parts by first carefully slitting the teflon barrier and the teflon side pieces, 9, with a thin razor blade. The very narrow slots were then carefully held open just wide enough to allow the teflon ribbon to be slipped into place. When released, the teflon slot clamped down on the ribbon; the seal formed was impervious to monolayer leakage. The small teflon side pieces holding the teflon ribbons to the sides of the torsion balance could be released so that this whole assembly (teflon side pieces, ribbons, and float) could be cleaned together in a hot $\text{HNO}_3 - \text{H}_2\text{SO}_4$ bath and reassembled without separating the teflon parts. Before the torsion balance was removed from the trough, two heavy gauge platinum wires, 10, were lowered to support the barrier.

In use, the torsion balance was lowered close to one

¹A correction must be added to L to allow for the presence of ribbons connecting the float to the trough side. In our case, $L = l_b + \frac{1}{2}l_s$. l_b is the length of the barrier, and l_s is the total distance between the barrier and the trough sides.

end of the trough; the relief milled shoulders, 11, of the brass side pieces rode on the trough edges. The separation of the two brass side pieces was adjusted so that the small teflon side pieces were held tightly to the teflon trough forming a seal impervious to monolayer flow. The torsion balance was placed on the trough so that the pressure sensing barrier was roughly 10 cm from the end of the trough.

The torsion balance transducer circuit is shown in Figure 5. The primary coil was excited by 4.2 volts 60 cps alternating current. The LVDT used was rated at 6.3 volts A.C.; we used a lower excitation voltage for calibration convenience. The output from the transducer circuit was led directly to a Moseley Autograf model 2S x-y recorder. The recorder sensitivity was adjusted to give a convenient y axis span, e.g., 5 d/cm per inch of chart paper was often a convenient sensitivity. The response of the pressure measuring circuit was linear to within the linearity specifications of the LVDT (better than 1%).

The barrier advance mechanism

The piston barrier advance mechanism, Figure 6, consisted of a tempered $\frac{3}{8}$ -inch steel rod, labeled 1 in Figure 6, on which a linear travel ball bushing could run. The Thompson ball bushing was forced into a brass, hexagonally cut block $1\frac{1}{2}$ in. x $1\frac{1}{4}$ in. x $1\frac{1}{4}$ in., 2. This assembly was

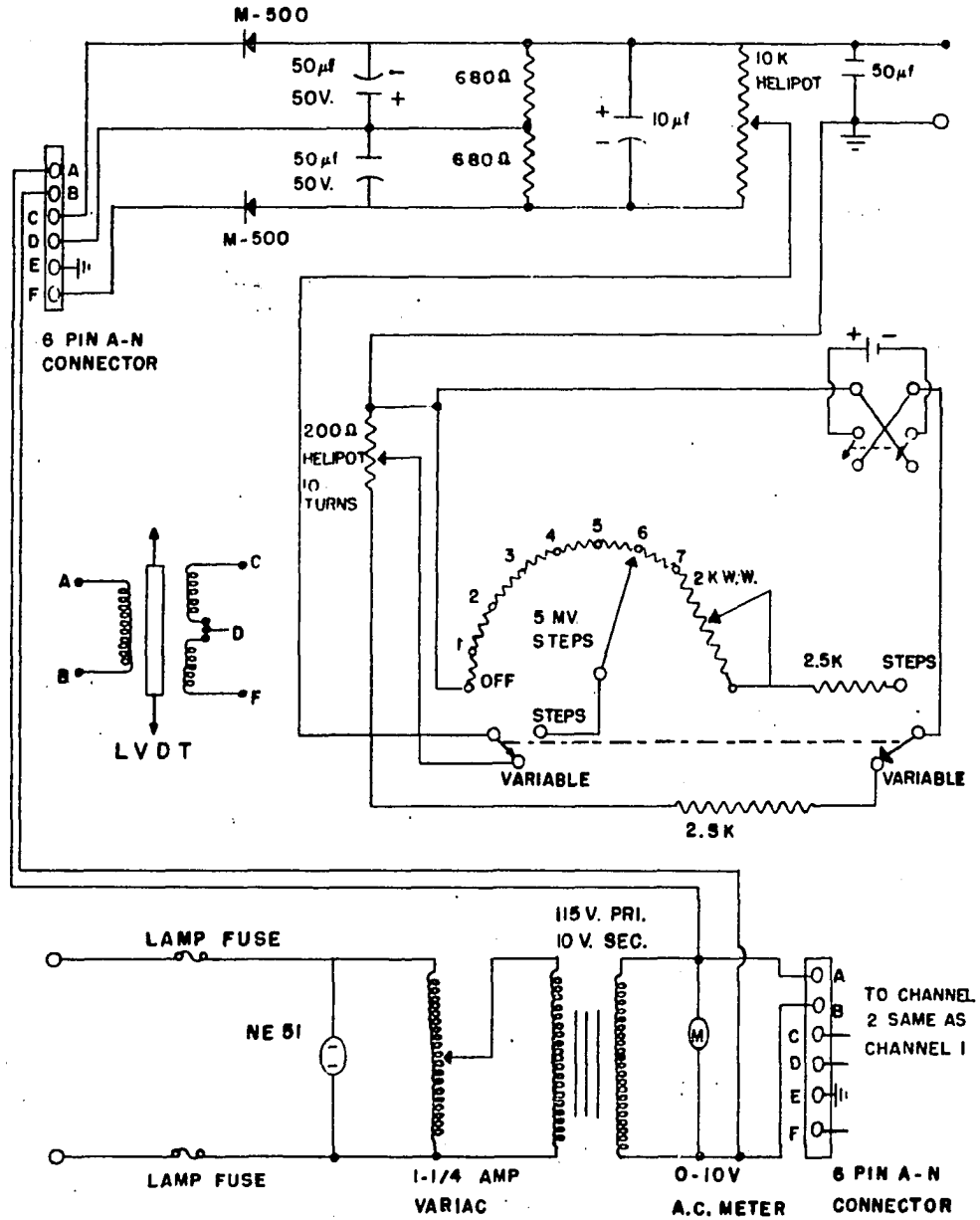
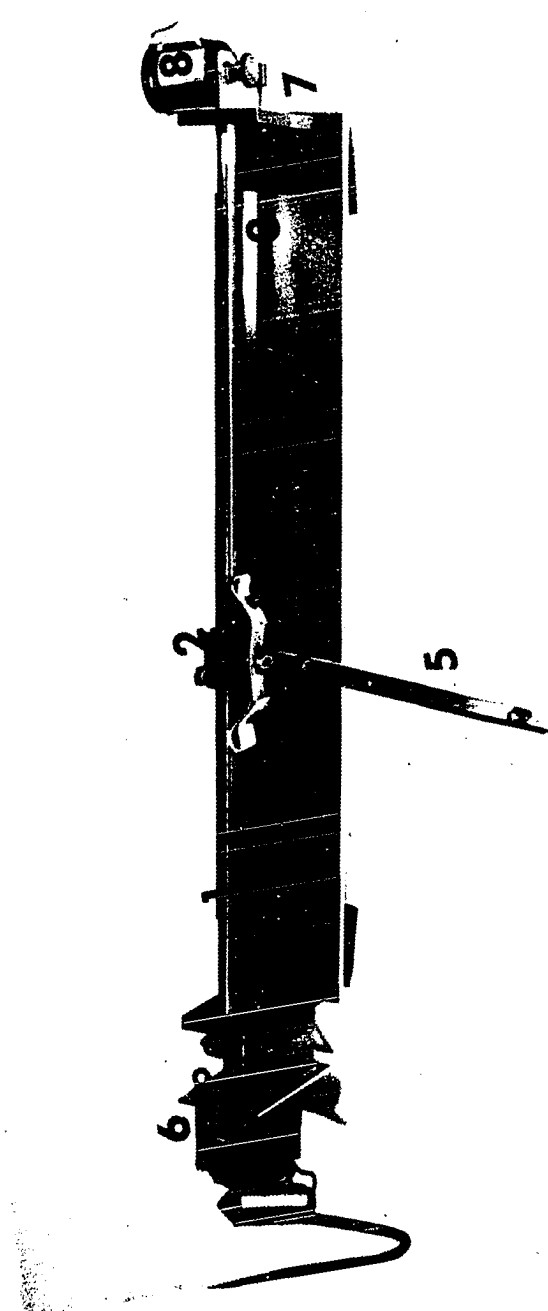


Figure 5. LVDT demodulation circuit

Figure 6. Barrier transport mechanism

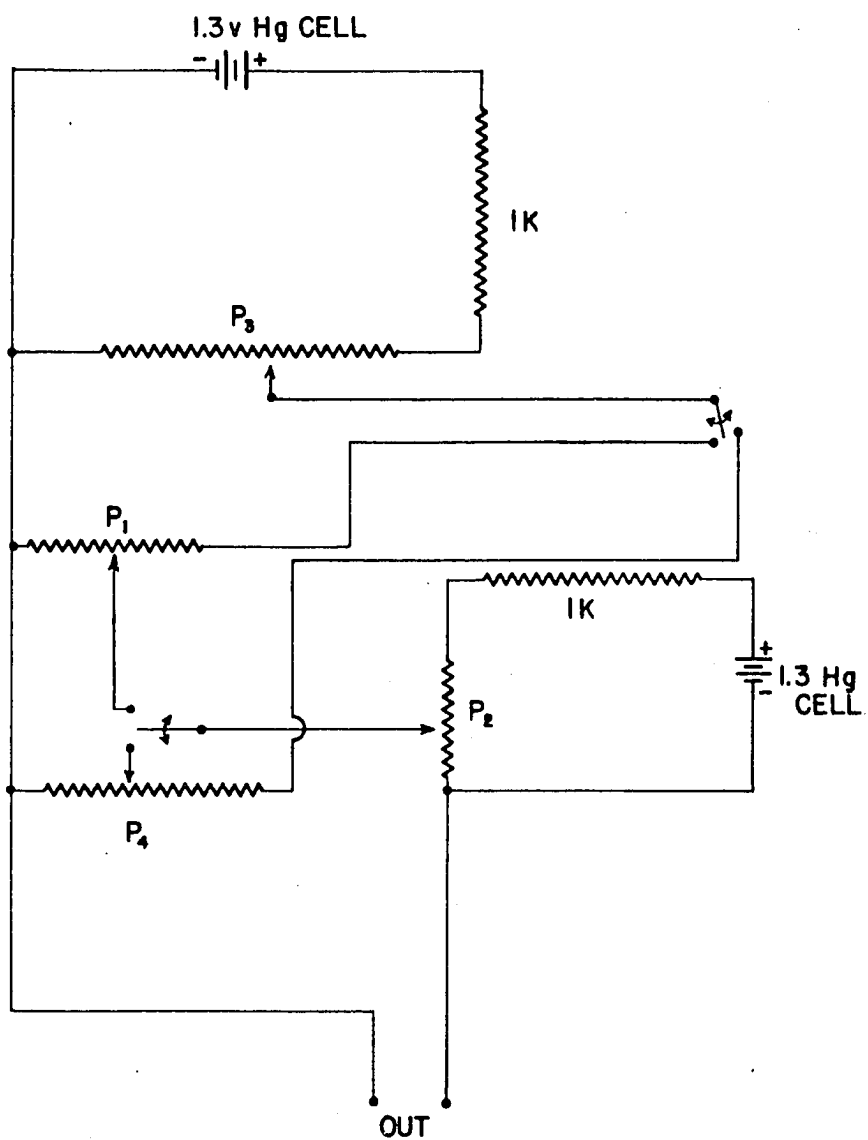
1. 3/8" steel rod
2. Thompson ball bushing assembly
3. Lead screw
4. Lead screw - bushing assembly
5. Aluminum L bar to carry teflon barrier
6. Bodine motor working into simple gear train
7. Worm gear coupling of lead screw to helipot
8. Helipot



placed on the tempered rod which had been polished to allow free movement of the bushing. A lead screw, 3, parallel to the tempered rod was installed through bushings at either end of the brass supporting structure just below the steel rod. A small, drilled and tapped brass block, 4, was placed on the lead screw and coupled to the brass block running on the tempered rod. Rotation of the lead screw caused the barrier support block to run smoothly over the tempered steel rod. An aluminum L bar, 5, was attached by a wing nut to the brass barrier support block. The long member of the L bar extended out over the trough and carried a teflon strip which could be adjusted to span the water surface and the trough edges. The lead screw driven by a geared, reversible Bodine motor, 6, moved the teflon strip back and forth over the trough. An assortment of gears and motors allowed a number of barrier velocities in the range of $0.6 \frac{\text{cm}}{\text{sec}}$ to $0.05 \frac{\text{cm}}{\text{min}}$. The lead screw was coupled by worm gear reduction, 7, to a 10 turn Helipot, 8. When the potentiometer was included in a battery circuit, the output of the helipot was directly proportional to the barrier position on the trough. The barrier circuit is shown in Figure 7. Provisions were made for zero suppression, sensitivity adjustment, and calibration. The Helipot calibration potentiometer was adjusted with a Duodial so that the dial setting was proportional to the barrier position.

Figure 7. Barrier transport circuit

- P₁ - Helipot (IK) coupled to barrier transport mechanism
- P₂ - Zero adjust Helipot (IK)
- P₃ - Range adjust Helipot (IK)
- P₄ - Reference Helipot (IK)



The calibration potentiometer allowed us to adjust the sensitivity of the circuit coupled directly to the x-axis of the recorder without running the barrier through numerous cycles across the trough.

The film balance operation sequence

The sequence of events in order to operate the automatic film balance was as follows:

1. The substrate was added to the trough until the liquid meniscus was above the edges of the teflon trough.
2. The surface was swept four or five times with a teflon bar being sure that liquid was carried over the end of the trough during each sweep.
3. The surface was allowed to quiet for roughly thirty seconds before the balance head was placed on the trough.
4. The teflon ribbon retainers were checked to be sure of a tight fit against the inner trough walls.
5. The platinum barrier supports were swung up out of the water releasing the barrier to float on the water surface.
6. The teflon pressure sensing barrier and ribbons were checked to insure that the trough solution was not wetting them.

7. The LVDT circuit was activated and calibrated by hanging weights on the arm opposite to the arm carrying the LVDT core. The recorder or LVDT span circuit was adjusted to give a convenient sensitivity, usually 5 d/cm per inch of pen displacement.
8. The sweep barrier was brought in close, approximately 1 cm, to the sensing barrier in order to check for surface contamination. If the trough and barrier had just been cleaned and assembled, contamination occurred at a rate of roughly one d/cm per hour in terms of compression to a barrier separation of 1 cm. Contamination occurred at a faster rate if the trough was not closed up in the air thermostat or if several monolayers had been previously run. If the rate of contamination became too high, say one d/cm per minute in terms of compression to the 1 cm barrier separation, the trough was disassembled and cleaned in hot one-to-one nitric acid-sulfuric acid mixtures.
9. The monolayer was next spread from a petroleum ether or benzene solution delivered to the surface by 100 -500 micropipets. The merits of the two solvents will not be argued here. LaMer (31) has discussed this aspect recently. We have found that low boiling petroleum ether gave reproducible

results with long chain fatty acid and alcohol systems. The area per molecule calculation was made using the following formula

$$A\left(\frac{\text{Å}^2}{\text{Molecule}}\right) = \frac{\text{Area of trough}(\text{cm}^2) \times 10^{16}}{\text{Molecules of surfactant in the surface}}$$

$$= 1.66 \times 10^{-5} \frac{\text{Molecular weight} \times \text{Width of trough (cm)} \times \text{Barrier separation (cm)}}{\text{Concentration} \left(\frac{\text{mg}}{\text{ml}}\right) \times \text{Volume of solution delivered (ml)}}$$

(Eq. 2)

10. Several minutes were allowed to pass before compression was begun. Although most of the solvent had evaporated before the first compression cycle, the initial compression curve was usually somewhat distorted. After the first several compression-expansion cycles, the π -A curves reproduced quite well.

The surface balance will easily detect changes in π of 0.1 d/cm. It was fairly easy to increase the sensitivity to allow detection of changes in π of 0.01 d/cm although such a high sensitivity was seldom employed. With the present barrier transport mechanism, we can easily see separation

changes of $0.1 \text{ \AA}^2/\text{molecule}$. Mechanical backlash was small amounting to approximately $\pm 0.1 \text{ \AA}^2/\text{molecule}$.

Ripple Instrumentation

Figures 3, 8 and 9 present a block diagram and photographs of the ripple analyzer built in this laboratory. The ripple apparatus employs a new, non-optical, detection technique; the forces generated by ripples impinging on the sensing probe are coupled to a piezoelectric transducer, a crystal phonograph cartridge in our case, which presents (for amplification and display) a signal proportional to the acceleration of the surface. For sinusoidal waves, the signal is directly proportional to the surface displacement. We have found that two items of information must be displayed at any given frequency and probe separation, viz., the phase angle relationship between the ripple generator and the sensing probe, and the amplitude of the signal seen by the sensing probe.

The ripple generator

The ripple generator was an electro-mechanical transducer, essentially a highly modified audio speaker, Figure 10. The magnet, designated by 1 in Figure 10, was a small, $2\frac{1}{2}$ inch, military voice speaker of conventional design. The manufacturer of the speaker used in our system is unknown.

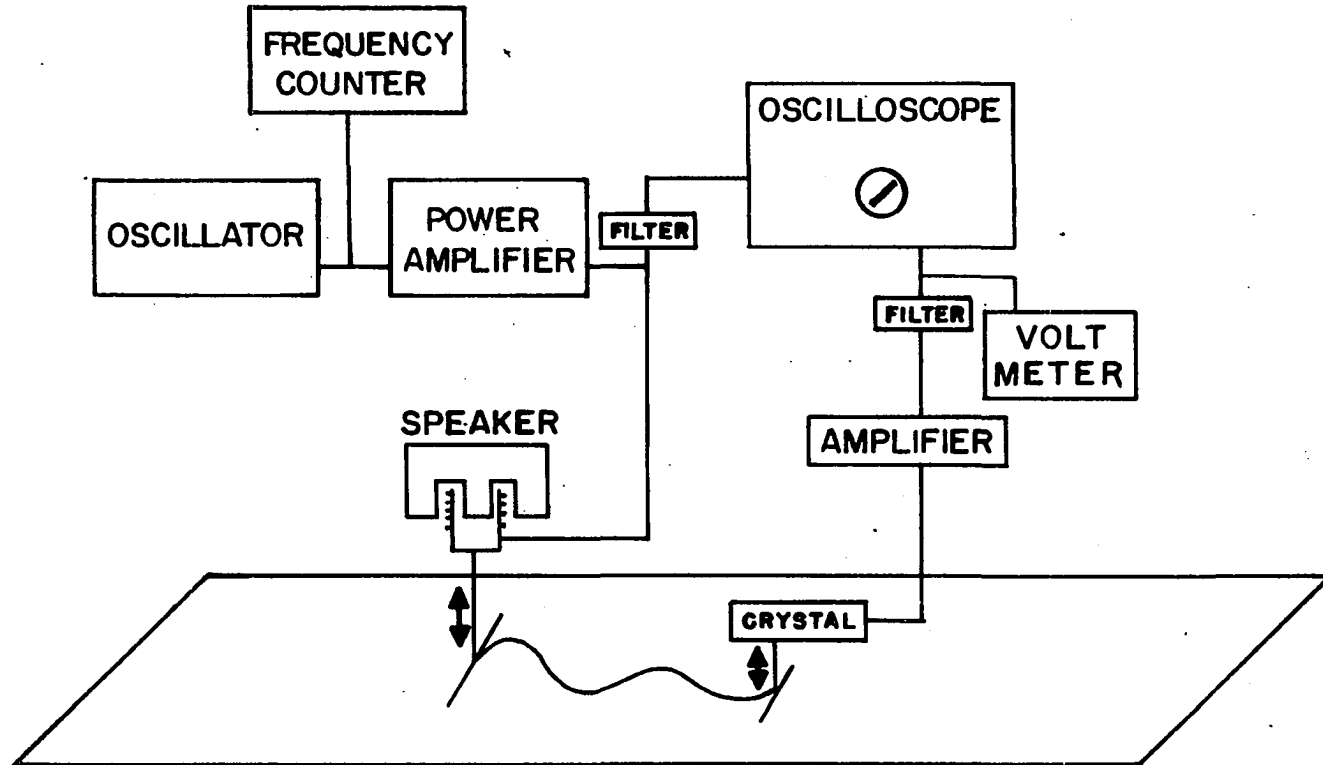
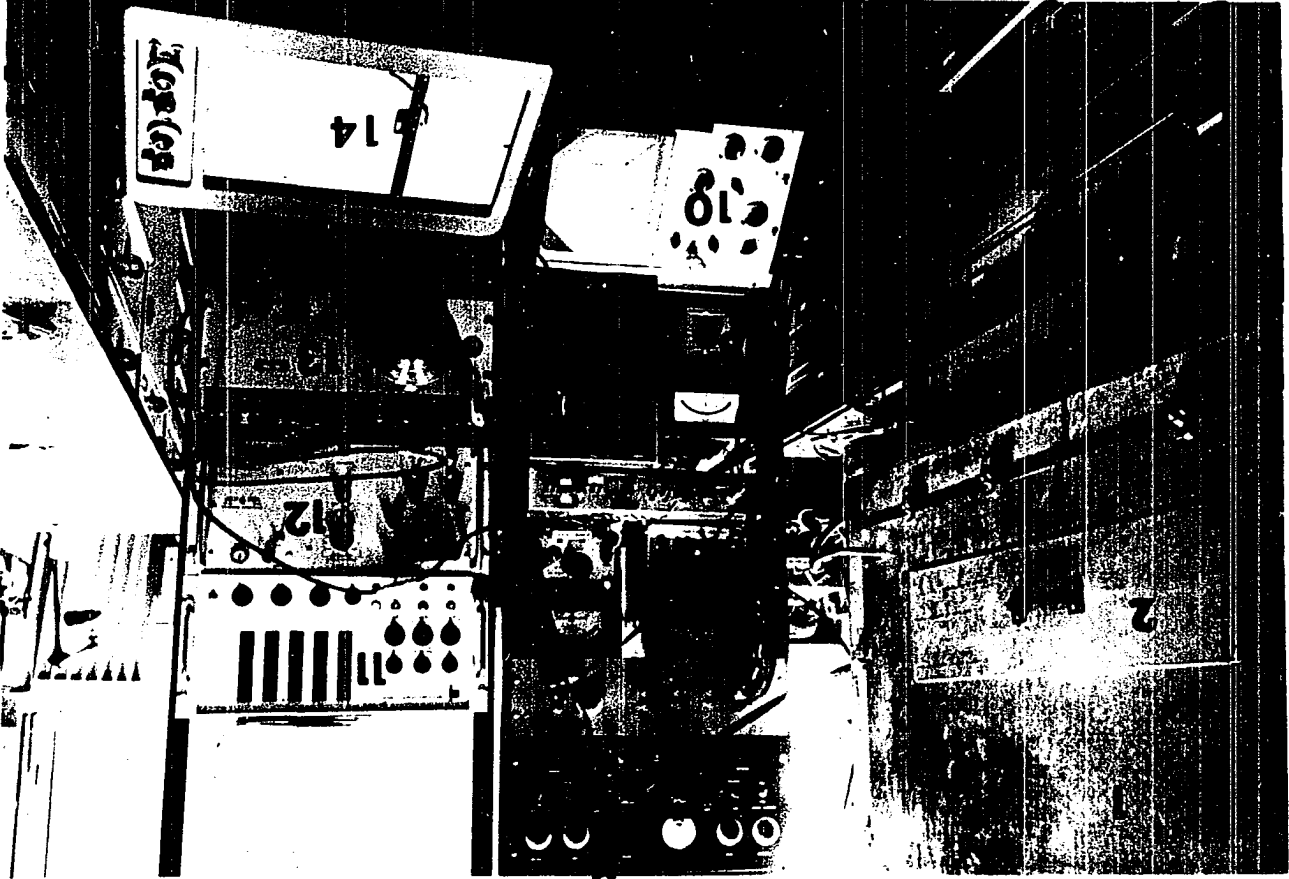


Figure 8. Ripple analyzer block diagram

Figure 9. Photograph of the apparatus closed for operation

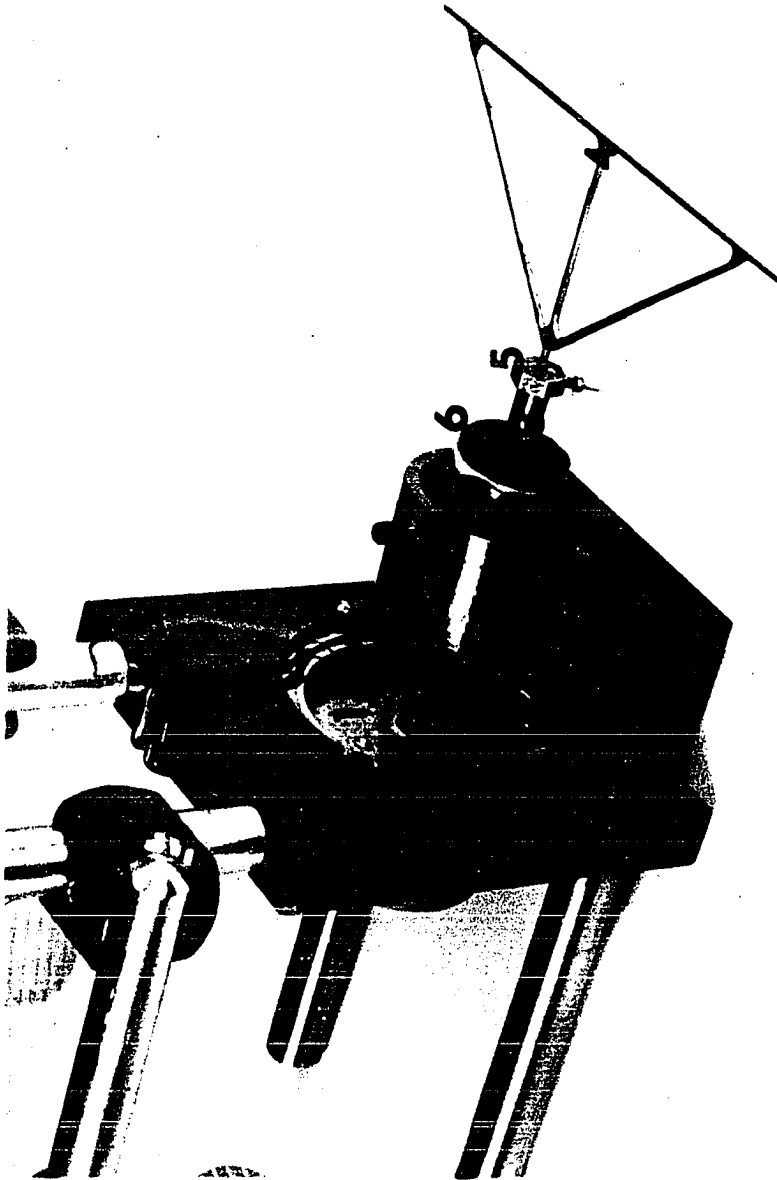
1. Air thermostat
2. Access port to interior of air thermostat
3. LVDT demodulation circuit
4. Matched filter circuit
5. Null detector - probe separation circuit
6. A.C. V.T.V.M. to monitor speaker coil signal
7. Barrier motor controls
8. A.C. V.T.V.M. to monitor receiving probe output
9. DuMont oscilloscope for phase display
10. Barrier and probe separation circuits
11. Frequency counter
12. Frequency standard oscillator
13. Working oscillator
14. Autograph x-y recorder



3

Figure 10. Ripple generator

1. Speaker magnet
2. Voice coil
3. Piston
4. Tee bar
5. Tee bar clamp
6. One of two flexible rubber washers



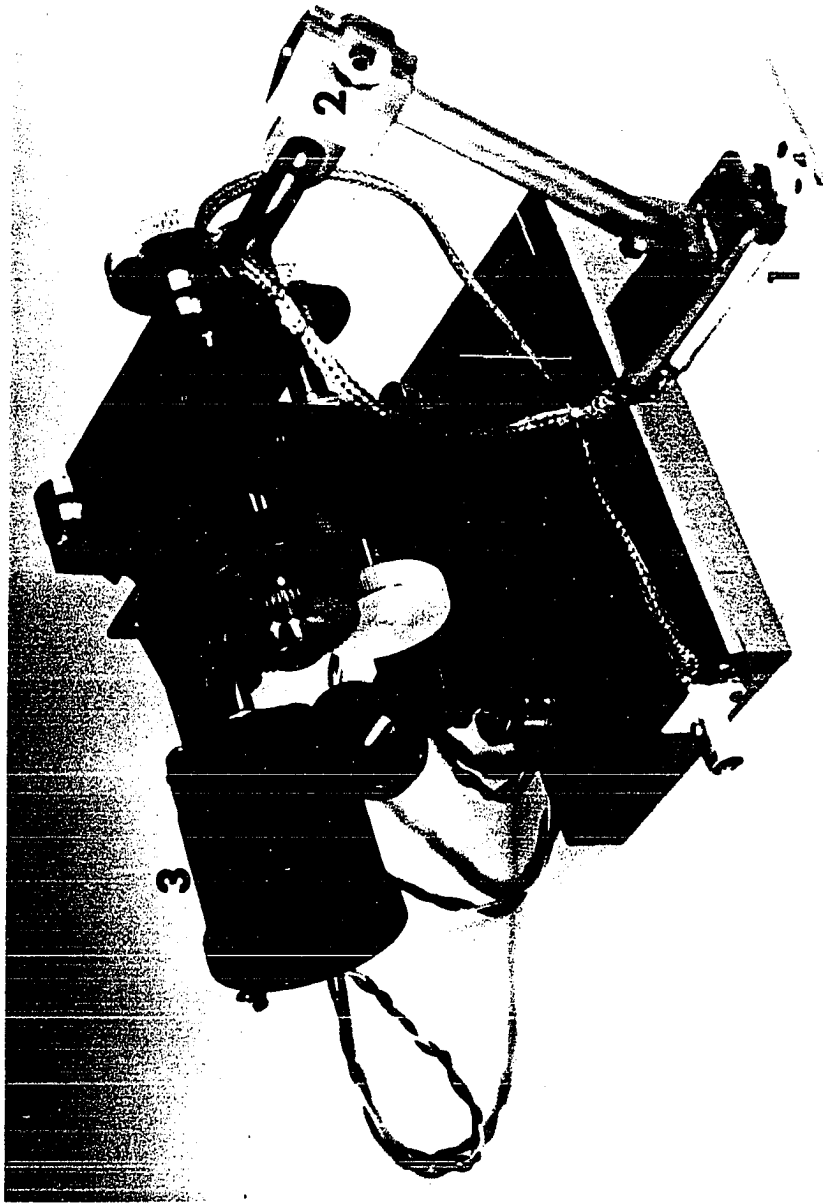
The voice coil, 2, was firmly attached, by an epoxy resin, to a piston, 3. The Tee bar, 4, actually producing the ripples was coupled to the piston by a wing nut clamping arrangement, 5. The Tee bar was easily released so that height and angular position could be adjusted. The thin hollow tube acting as a piston was supported by two pieces of flexible rubber sheet washers, 6. The voice coil was excited by the output from a 25 watt Heathkit power amplifier fed by a Hewlett Packard model 200 JR audio oscillator. The signal level into the voice coil was monitored by a Hewlett Packard 400H A.C. vacuum tube voltmeter. The signal output from the voltmeter passed through a filter circuit and then was led to the x-axis input of the oscilloscope. The frequency range covered extended from 30 cps to 2,000 cps. A Computer Measurements Co. model 225C counter or a Hewlett Packard model 100 ER frequency standard oscillator was used to measure frequency to ± 0.1 cycle per second or better. Unfortunately the mass of the Tee bar was sufficiently great so that under the circumstances of the measurement the mechanical impedance of the system was mass controlled. This implies that the amplitude attenuates as $\frac{1}{\omega^2}$. The Tee bar amplitude at constant power input rapidly decreased with frequency beyond roughly 300 cps.

Ripple receiving transducer

The ripple sensing device, designated by 1 in Figure 11, was a phonograph crystal cartridge, designated N4-3, made by Astatic Inc. The cartridge was designed for resonance free response in the range of 50 cps to 5,000 cps. The crystal cartridge was mounted on a micromanipulator distributed by Brinkman, Inc. The mounting arm, 2, was arranged so that the orientation of the cartridge with respect to the micromanipulator could be adjusted and then firmly clamped. The micromanipulator had 10:1 planetary gear attachments on each of the three axis movements. It was possible to move the cartridge over the surface precisely positioning it with respect to the sending Tee bar and with respect to the water surface. The receiving probe was initially a Tee constructed from 30 mil copper wire. The shank of the Tee was fitted into the screw clamp well on the crystal cartridge in place of the usual phonograph needle. Any vibration of the Tee bar was transmitted to the sodium potassium tartrate piezoelectric wafer enclosed in the cartridge. The voltage out of the crystal was first amplified by a Tektronix low level preamplifier. The filtered output from the preamplifier was fed into the y-axis of the oscilloscope and into a second 400H Hewlett Packard A.C. vacuum tube voltmeter. The filter circuits will be described later. The oscilloscope displayed the phase

Figure 11. Ripple receiving transducer

1. Phonograph cartridge
2. Mounting arm
3. Helipot coupled through gears to micromanipulator control



relationship between the sending and receiving probes while the voltmeters measured the amplitudes of the vibrating probes.

During the initial phase of the experimental effort, we were interested in establishing whether the receiving probe was responding only to surface disturbances or whether mechanical coupling was also occurring through the aqueous substrate or through the air. The probe response was studied as a function of vertical displacement. Capillary ripples were generated on a swept water surface at some convenient frequency such as 300 cps. The receiving probe was placed so that the sending and receiving Tee bars were parallel. The receiving probe could be moved in three mutually perpendicular directions by use of the micromanipulator. The probes were separated about $1\frac{1}{2}$ cm and then the output from the crystal cartridge was recorded as a function of displacement from the surface, Figure 12. A rapid increase in signal occurred when the probe just touched the water surface, and a rapid decrease in signal occurred when the probe broke through the surface. Bringing the probe back into the surface region produced the same results; the signal from the probe increased rapidly when the probe just reached the surface and decreased rapidly when the probe broke through the surface into the air. This experiment showed conclusively that the signal was caused by surface

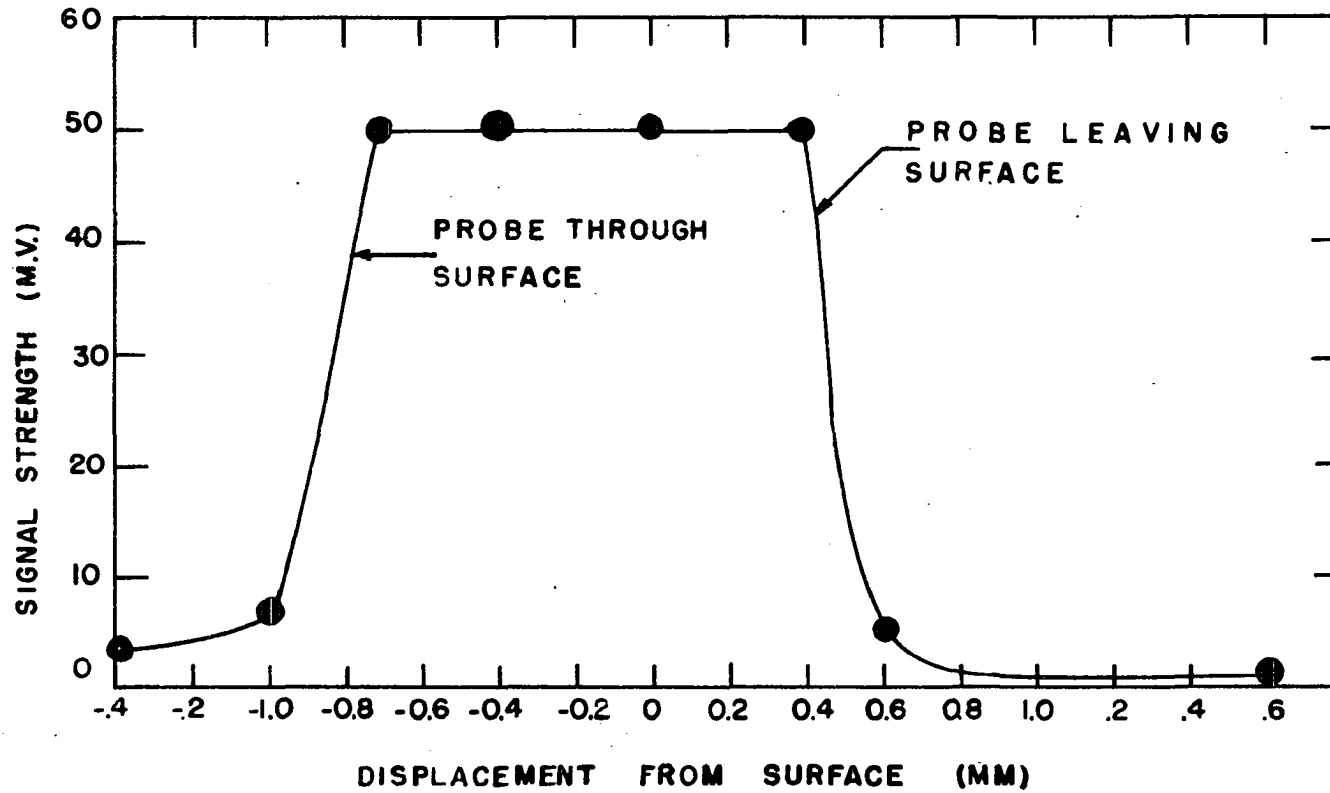


Figure 12. Dependence of receiving probe output on vertical location of the receiving Tee bar

disturbances.

A difficult aspect of the experimental technique was the measurement of probe separation. The micromanipulator had vernier scales on each axis allowing measurement of probe displacement to 0.01 cm. To measure the ripple wave lengths directly, the probe separation must be established to at least 0.001 cm. It turned out that coupling a 10 turn 100 K Helipot, 3, through gears to the course adjustment on the x axis of the micromanipulator allowed one to establish the magnitude of probe displacements to the required precision. The potentiometer was hooked into the circuit shown in Figure 13. Mercury dry cells were used for current sources and a Kintel, model 203, high impedance microvoltmeter was used to establish the null. A high resistance potentiometer was used since the resolution of a wire-wound potentiometer increases with the number of turns of wire on the slide wire helix. Using the circuit with the microvoltmeter on the one millivolt range presented the greatest useable resolving power. The resolution under these conditions was about ± 0.0004 cm. It should be noted that the Helipot could have been put into a bridge circuit; however, the double potentiometer circuit shown in Figure 13 was easy to build and with mercury batteries as current sources proved to be very stable.

The calibration of the probe separation circuit was

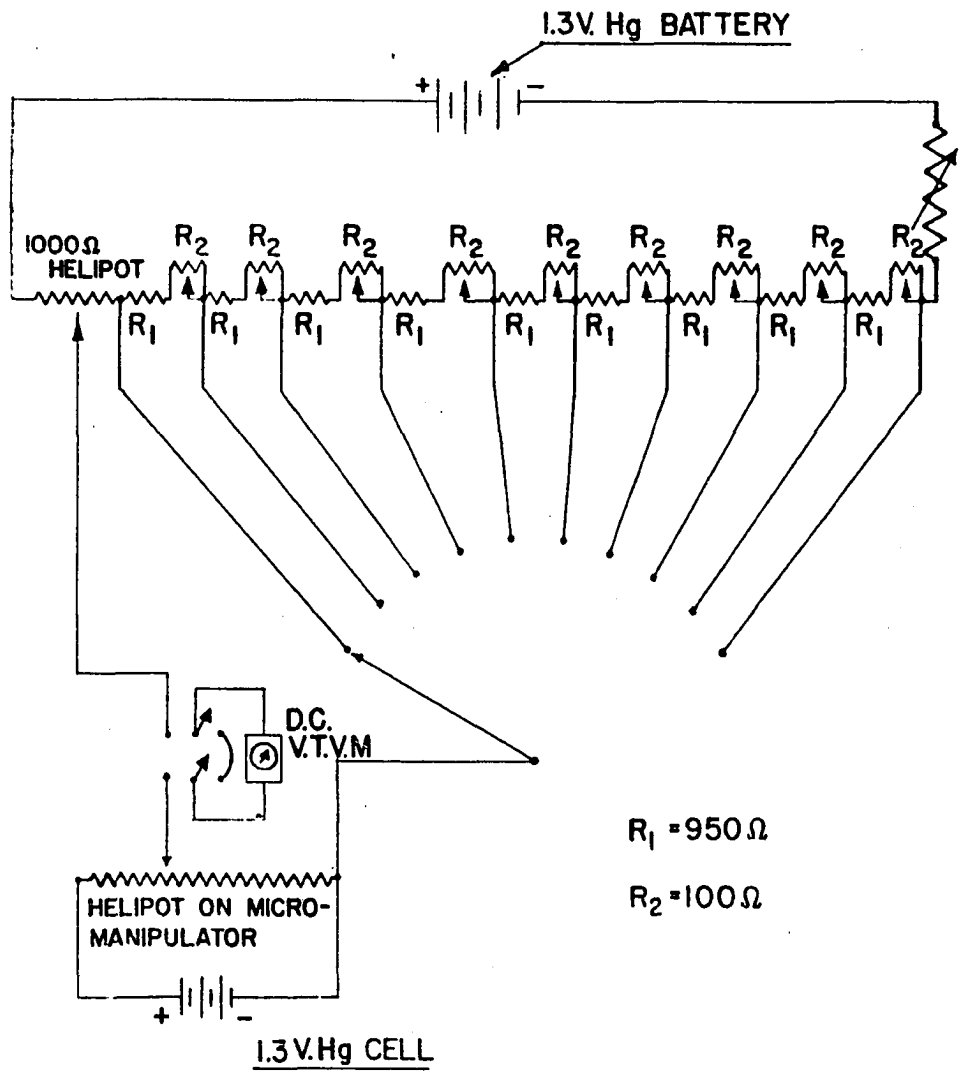


Figure 13. Probe separation circuit

fortunately easy. The scale on the x axis movement was compared to the scale on a Cambridge measuring machine. They were found to agree to within 0.0001 cm. Viewing the scale, replaced on the micromanipulator, through a low power microscope allowed us to calibrate the probe separation circuit reproducibility to within ± 0.0004 cm. The range + pot settings were nearly linear with probe separation; the deviations from linearity did not exceed $\pm 0.1\%$ and could be easily corrected with the use of a correction graph prepared from the calibration data.

A number of different Tee designs were tried. A satisfactory arrangement appeared to consist of a razor blade soft soldered to a short piece of high temperature silver solder. Since the needle well on the phonograph cartridge was angled, the blade was soldered to the shank at an angle so that the cutting edge would be parallel and the blade perpendicular to the water surface. As in the case of the generator probe, the mass of the probe should be minimized. "Thin Gillette" blades were used at first with this point in mind; however, they would tend to distort under the heat of soldering. The single edge laboratory razor blade was finally used. Several probes were made that remained undistorted even with soft soldering. The blades were flat to within 25 microns. The blades were always coated with a thin layer of paraffin to render them hydrophobic. In use

the blade could be brought down to touch the monolayers without radically disturbing the film. The vertical position of the blade was easily kept constant relative to the surface by watching light reflected from surface regions near the blade and adjusting the trough water level or probe height until no meniscus was visible close to the blade.

Pick-up noise was minimized by carefully shielding the leads from the crystal cartridge to the preamplifier, low noise Amphenol RG-62/u coaxial cable was used. All instruments used in this study were eventually grounded through a grounding system available in the laboratory and supposedly independent of the main grounding system. Even with very careful grounding of the carefully shielded high impedance circuits, stray pick-up from two sources proved very irritating. Degassing of ion vacuum gauges located in the same room produced large amounts of white noise amply received and amplified by the probe circuit. Fortunately, the degassing procedure was intermittent and so easily scheduled. Much more irritating was the fact that an induction furnace converter on the floor below, some 25 to 50 yards away, broadcasted white noise amply received and amplified by our system. Attempts to eliminate this source of noise were not profitable. Fortunately, operation scheduling to our mutual satisfaction attenuated the problem. Building vibration was always a source of noise in these experiments. Sharp noises,

overly loud conversations, resonant voices and other such laboratory sound sources induced noise levels which could reduce the signal-to-noise ratio to unmanageable levels. Measures taken to combat these problems will be discussed later in This Thesis.

Air thermostat

For the purposes of temperature, contamination, vibration and sonic noise control, the sending and receiving probe mechanisms and the film balance were mounted in a constant temperature air bath, approximately 5 ft. x 3 ft. x $2\frac{1}{3}$ ft. The air bath, partially shown in Figure 9 and designated by 1, looked much like a deep freeze unit placed on its side and oriented so that the door could open out. The unit was constructed from galvanized sheet metal. The space left between the inner walls of the chamber and the outer walls, roughly 4 in., was insulated with Styrofoam packing. Copper tubing was soldered to the walls of the inside chamber so that water from a constant temperature bath could be circulated exchanging heat with the inner chamber. Two types of front doors were used during this research. In common, they provided for circulation of the constant temperature bath water through the door region. One set of doors was made from plexiglass pieces cemented and firmly screwed together so that a water tight annular space was

formed. Temperature controlled water was circulated through this annular space. Two of these doors were required to span the open front of the air bath. The doors were too heavy to hinge; instead they were allowed to rest on weather stripping glued to the front edge of the inner chamber. Twelve spring clamps held the doors in place against the weather stripping. The chamber when "buttoned up" was fairly gas tight. The only air leaks occurred around the two 1 in. diameter electrical lead-through ports. While the plexiglass doors had the advantage that they afforded an interior view, they were heavy and hard to maneuver. The second set of doors was made from galvanized sheet metal with copper tubing soldered to the inner wall panel. The annular space between the inner and outer walls of the door was filled with insulation. A section of this door, 29 in. x 5 in. x $1\frac{1}{2}$ in., could be independently removed to allow observation and manipulation of equipment in the chamber. The door was held in place with the 12 previously mentioned spring clamps. At 25°C , the temperature was controlled to $\pm 0.05^{\circ}\text{C}$. A small fan controlled from outside the chamber circulated the air destroying thermal gradients. The fan had to be turned off during ripple measurements.

Vibration control

A very important concern was the isolation of the apparatus from building vibration. Building decoupling was

never completely successful; however, the noise generated at the receiving probe due to building vibration was minimized by the following steps:

- i) Several layers of $\frac{1}{4}$ in. rubber sheet were placed under a soap stone 5 ft. x 3 ft. x 3 in. The air thermostat was supported at the four corners on this soap stone by four damped spring shock mounts (Korfund, Type LO-A32). The floor of the inner chamber of the air thermostat was covered with $\frac{1}{4}$ in. rubber strips, 1 in. wide. A flat piece of boiler plate 37 in. x 16 in. x $\frac{1}{2}$ in. was placed on these rubber strips. The micromanipulator and surface balance were mounted on this plate, see Figure 3. The sending probe was mounted on a Dexion structure built over but separated from the steel plate and isolated from the chamber floor by 1 in. x 1 in. x $\frac{1}{4}$ in. rubber squares. The tripod support screws for the teflon trough ride in three shallow depressions punched in the steel plate at appropriate positions. The barrier sweep mechanism was positioned behind the trough slightly beyond the edge of the steel plate on rubber supports.
- ii) Lint free wet towels were hung from the Dexion supporting structure close to the inner walls. A piece of acoustic damping composition board was

placed across one end of the trough. These precautions appeared to decrease the noise level by a factor of approximately 5.

iii) Matched filter circuits were built to filter out selectively 60 cps and 20 cps noise, Figure 14. A matched pair of high pass filters was also included in the circuit. The 3 db point for this filter pair was 240 cps. The filters were placed in the circuit symmetrically with respect to the x and y axis of the oscilloscope, see Figure 8. Thus even though the signal passing through the filter from the preamplifier side would suffer phase changes as the frequency was brought close to the maximum reject region, the phase shift was exactly matched by the other member of the filter pair placed in the circuit between the oscilloscope and the speaker coils. Switching allowed the six filters to be by-passed or not in any desired combination. The filter circuits were vitally needed above roughly 300 cps.

Initial steps in operation of the apparatus

The sequence of operations for measuring capillary ripple propagation parameters include:

i) The trough was lowered so that neither probe was in

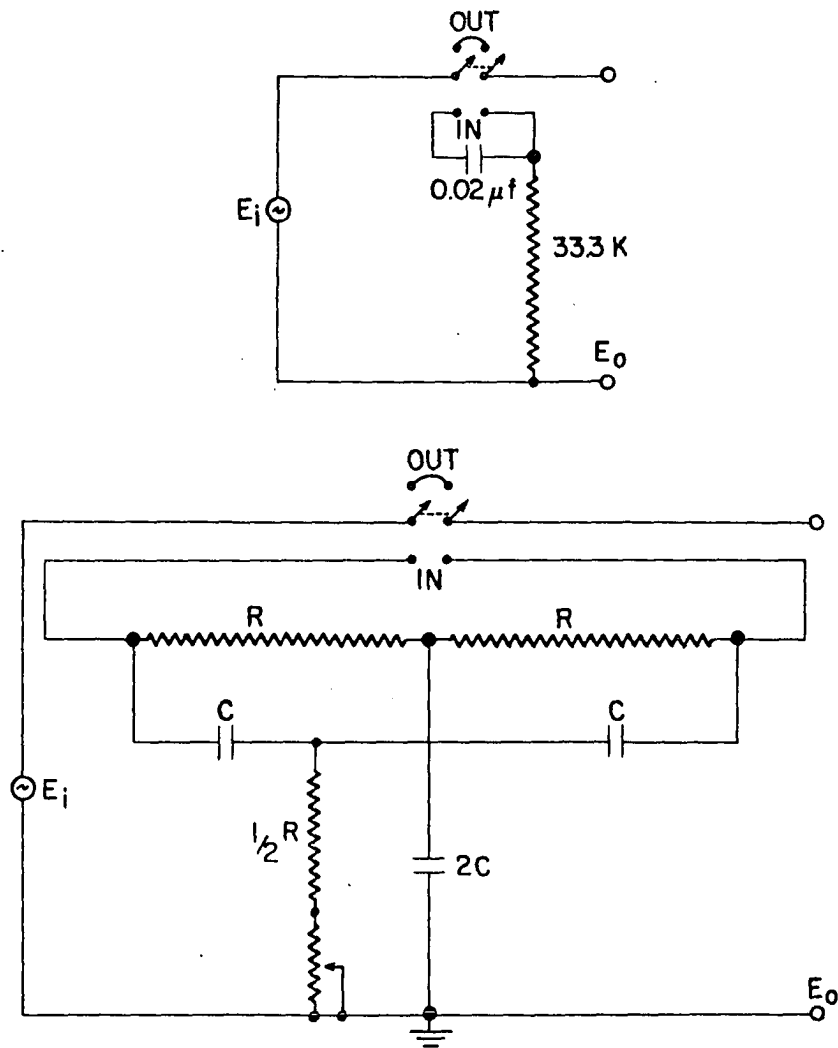


Figure 14. High pass and peaked filter circuits

the water surface.

- ii) The surface was swept to clean off possible surface contamination. In the case of insoluble monolayers, the monolayer was spread from a solution of benzene or low boiling petroleum ether. Initial force-area curves were determined to check film characteristics. The surface pressure was reduced from roughly 10 d/cm to the lowest surface pressure which would still ensure a continuous film. This pressure was roughly 0.3 d/cm in the case of films such as that formed by stearic acid.
- iii) The trough was then carefully raised by turning in the three trough support bolts until the sending bar just contacted the surface. The receiving probe was then positioned and lowered to the surface for the actual measurement of the propagation parameters.

The propagation parameters of interest were the phase velocity as a function of frequency and the wave damping coefficient as a function of frequency. Several techniques were available for each case. We could measure propagation velocity either by directly measuring the wave length at known frequencies or else by keeping the probe separation constant and finding all frequencies for which there were half-integer numbers of waves between the probes. Damping

in mechanical systems usually follows an exponential decay law and this was found to be so in the case of capillary ripples. Before discussing the data collection sequence in detail and the errors associated with the present level of instrumentation, we believe that a mathematical discussion of the wave motion pertaining to our experiments will speed understanding of the operational details.

Calculation of the damping coefficient

Since the data actually collected were the r.m.s. voltage outputs from the receiving probe as a function of probe separation at constant frequency, we had to establish that, over the frequency range investigated, the r.m.s. output from the receiving probe was directly proportional to the particle amplitude at the receiving probe. Since the waves should follow an exponential damping law, one would suppose that the log plot of signal strength with probe separation should be linear with the slope equal to the negative of the damping coefficient. This was true if the probe separation was sufficiently large (Figure 15); however, Figure 16 shows that amplitude varied periodically with probe separation at small separations. It should be obvious that the waves can no longer be considered as traveling waves but rather as standing waves. The fact that waves are reflected at the receiving probe and again at the

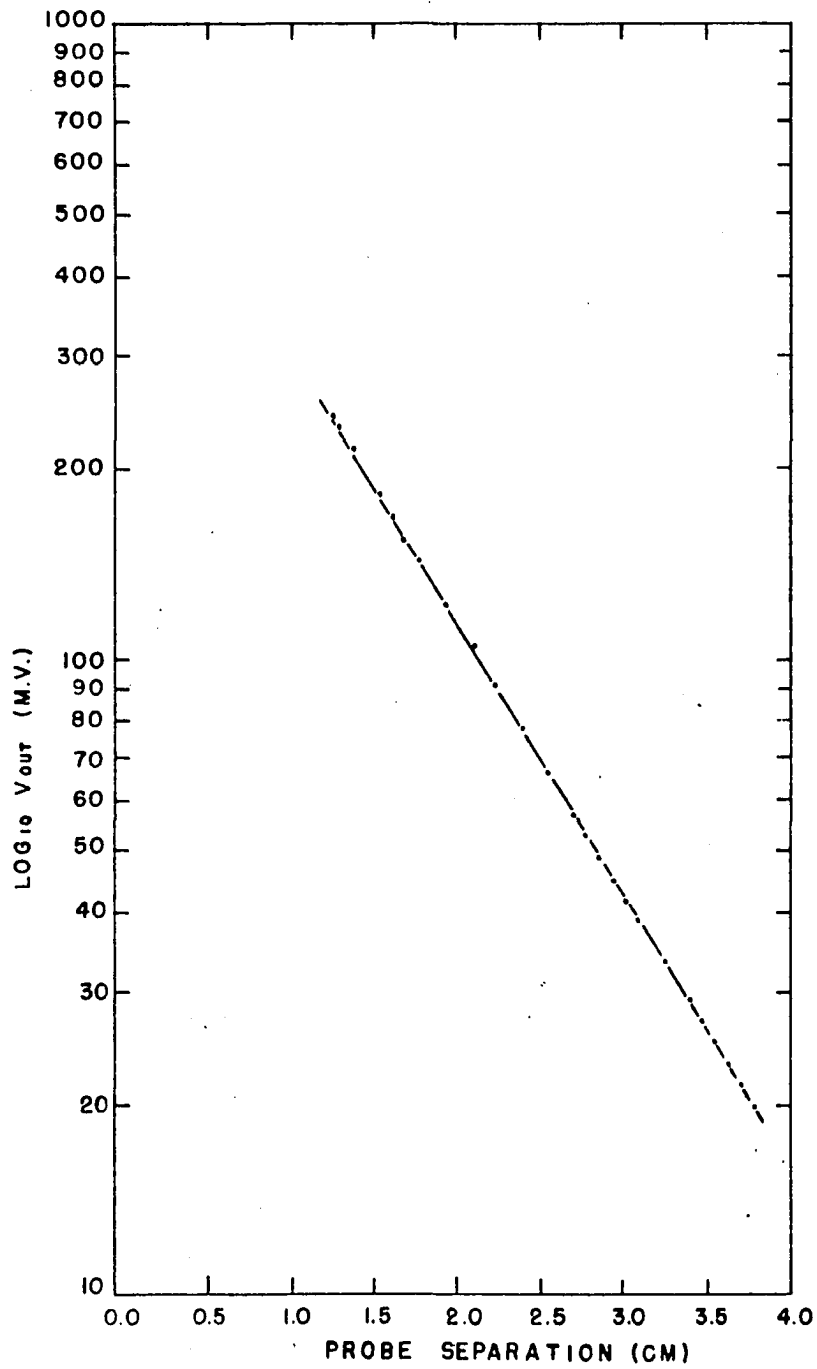


Figure 15. Ripple damping at large probe separation

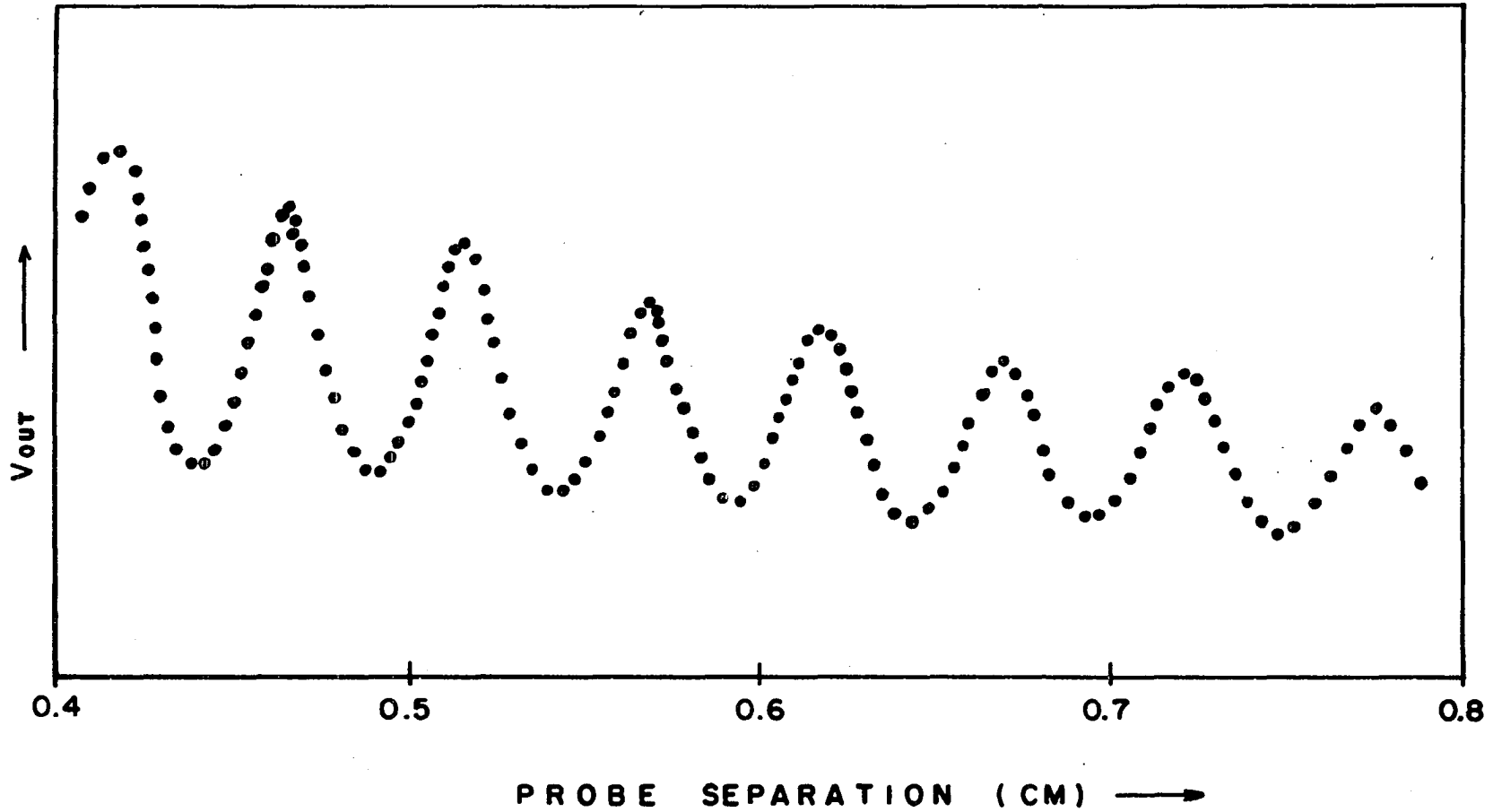


Figure 16. Ripple damping at small probe separation

sending probe cannot be ignored. The analysis of the wave motion closely parallels the analysis of vibration damping in stretched polymer filaments. The work of Hillier and Kolsky (32) was found to be pertinent. They sketch the theory to be presented here. They used real representation for the wave motion; we use complex representation for the motion. Their wave count vs. probe separation and amplitude vs. probe separation data¹ closely parallels our data given in Figures 15 and 16. We next proceed to derive the equations which will allow the calculation of damping coefficients and propagation parameters from our data.

Let the driven probe be situated at $x = 0$ and move according to

$$y(0) = A \exp(i\omega t) \quad . \quad (\text{Eq. 3})$$

Let the receiving probe be situated at $x = L$ and move relative to the driven probe according to

$$y(L) = B \exp i(\omega t + \theta) \quad . \quad (\text{Eq. 4})$$

The waves propagated along the trough will be reflected at $X = L$ and again at $X = 0$. After a short period of time,

¹Hillier and Kolsky (32), figure 5, page 116.

steady state conditions will exist such that between the probes

$$y(x) = y_0 \exp(-\alpha x) \exp i(\omega t - kx) - y_1 \exp(\alpha x) \exp i(\omega t + kx) \quad (\text{Eq. 5})$$

will hold and beyond the barrier the waves not reflected will be described by

$$y_2(x) = y_2 \exp(-\alpha x) \exp i(\omega t - kx) \quad (\text{Eq. 6})$$

We assume that the distance from $x = L$ to the trough edge is such that

$$\lim_{x \rightarrow \text{edge}} y_2(x) \approx \lim_{x \rightarrow \infty} y_2(x) = 0 \quad (\text{Eq. 7})$$

Hence $y_2(x)$ is of no further interest.

Specifically for our case, the outgoing wave will be given by

$$\vec{y}(x) = y_0 \exp(-\alpha x) \exp i(\omega t - kx)$$

and the reflected wave by

$$\overleftarrow{y}(x) = -y_0 r \exp(i\varphi) \exp -\alpha(2L-x) \exp i(\omega t - k[2L-x])$$

where

$$\frac{\text{Complex amplitude of reflected wave}}{\text{Complex amplitude of incident wave}} = -r \exp(i\varphi)$$

which takes into account not only an amplitude change upon reflection but also a phase change, φ .

Adding \overrightarrow{y} and \overleftarrow{y} will give the displacement y at x ;

$$y(x) = y_0 [\exp(-\alpha x) \exp i(\omega t - kx) - r \exp(i\varphi) \exp -\alpha(2L-x) \exp i(\omega t - k(2L-x))] .$$

For boundary conditions we have

$$y(0) = A \exp(i\omega t) = y_0 [1 - r \exp(i\varphi) \exp(-2\alpha L) \exp(-2ikL)] \exp(i\omega t)$$

so that

$$y_0 = A [1 - r \exp(i\varphi) \exp(-2\alpha L) \exp(-2ikL)]^{-1} .$$

We also can determine y_2 in Equation 6 from the condition $y(L) = y_2(L)$, however this is of no concern here. Thus

$$y(x) = \frac{A[\exp(-\alpha x)\exp i(\omega t - kx) - r \exp(i\varphi)\exp -\alpha(2L-x)\exp i(\omega t - k(2L-x))]}{[1 - r \exp(i\varphi)\exp(-2\alpha L)\exp(-2ikL)]} \quad (\text{Eq. 8})$$

The receiving probe signal is proportional to the acceleration of the blade forced into motion by ripples traveling down the trough; the probe output will be also proportional to the displacement for sinusoidal waves as used in our application. Thus at the probe

$$V(L) = \frac{\bar{A}[\exp(-\alpha L)\exp i(\omega t - kL) - r \exp(i\varphi)\exp(-\alpha L)\exp i(\omega t - kL)]}{[1 - r \exp(i\varphi)\exp(-2\alpha L)\exp(-2ikL)]}$$

where $V(L)$ is the voltage output from the crystal cartridge at L cm from the driven probe. Rewriting slightly we have that

$$V(L) = \frac{[1 - r \exp(i\varphi)]\bar{A} \exp(-\alpha L)\exp i(\omega t - kL)}{[1 - r \exp(i\varphi)\exp(-2\alpha L)\exp(-2ikL)]} \quad (\text{Eq. 9})$$

From the form of Equation 4, we see that we would like to introduce a phase factor into Equation 9. Let us rewrite Equation 9 as

$$\begin{aligned}
 V(L) &= \frac{[1-r \exp(i\varphi)] \exp(-ikL)}{[1-r \exp(i\varphi) \exp(-2\alpha L) \exp(-2ikL)]} \bar{A} \exp(-\alpha L) \exp(i\omega t) \\
 &= C \bar{A} \exp(-\alpha L) \exp(i\omega t) \quad . \quad (\text{Eq. 10})
 \end{aligned}$$

We introduce the phase relation between the probes by writing the complex constant C as

$$C = a+ib = |C| \exp(i\theta) \text{ where } \tan\theta = \frac{b}{a} \quad .$$

Some algebraic manipulation yields

$$\begin{aligned}
 a &= \frac{\cos kL [r^2 \exp(-2\alpha L) + 1] - r [\exp(-2\alpha L) + 1] \cos(\varphi - kL)}{[1 - 2r \exp(-2\alpha L) \cos(\varphi - 2kL) + r^2 \exp(-4\alpha L)]} \\
 b &= \frac{r [\exp(-2\alpha L) - 1] \sin(\varphi - kL) + [r^2 \exp(-2\alpha L) - 1] \sin kL}{[1 - 2r \exp(-2\alpha L) \cos(\varphi - 2kL) + r^2 \exp(-4\alpha L)]}
 \end{aligned}$$

and so

$$\tan\theta = \frac{r [\exp(-2\alpha L) - 1] \sin(\varphi - kL) + [r^2 \exp(-2\alpha L) - 1] \sin kL}{[r^2 \exp(-2\alpha L) + 1] \cos kL - r [\exp(-2\alpha L) + 1] \cos(\varphi - kL)} \quad .$$

(Eq. 11)

Recalling that

$$C = \frac{[1-r \exp(i\varphi)] \exp(-ikL)}{1-r \exp(-2\alpha L) \exp i(\varphi-2kL)}$$

$$|C| = \frac{|[1-r \exp(i\varphi)] \exp(-ikL)|}{\sqrt{1-2r \exp(-2\alpha L) \cos(\varphi-2kL) + r^2 \exp(-4\alpha L)}}$$

So that we have

$$C = \frac{\sqrt{1-2r \cos\varphi + r^2} \exp(i\theta)}{\sqrt{1-2r \exp(-2\alpha L) \cos(\varphi-2kL) + r^2 \exp(-4\alpha L)}}$$

(Eq. 12)

where $\tan\theta$ is given by Equation 11.

The final equation is then

$$V(L) = \frac{\bar{A} \sqrt{1-2r \cos\varphi + r^2} \exp(i\theta) \exp(-\alpha L) \exp(i\omega t)}{\sqrt{1-2r \exp(-2\alpha L) \cos(\varphi-2kL) + r^2 \exp(-4\alpha L)}}$$

(Eq. 13)

with θ given by Equation 11.

Let $\varphi = 0$, then

$$V(L) = \frac{\bar{A}(1-r)\exp(i\theta)\exp(-\alpha L)\exp(i\omega t)}{\sqrt{1-2r\exp(-2\alpha L)\cos 2kL+r^2\exp(-4\alpha L)}} \quad (\text{Eq. 14})$$

and

$$\begin{aligned} \tan\theta &= \frac{-r[\exp(-2\alpha L)-1]+r^2\exp(-2\alpha L)-1}{r^2\exp(-2\alpha L)+1-r\exp(-2\alpha L)-r} \tan kL \\ &= \frac{(1-r)[-r\exp(-2\alpha L)-1]}{(1-r)[1-r\exp(-2\alpha L)]} \tan kL \end{aligned}$$

so that

$$\tan\theta = \frac{[r\exp(-2\alpha L)+1]}{[r\exp(-2\alpha L)-1]} \tan kL \quad (\text{Eq. 15})$$

Using K as a constant independent of L , the r.m.s. crystal cartridge output will be given by

$$\overline{V(L)} = \frac{K\exp(-\alpha L)}{\sqrt{1-2r\exp(-2\alpha L)\cos kL+r^2\exp(-4\alpha L)}} \quad (\text{Eq. 16})$$

We see that if L is sufficiently large,

$$\overline{V_1(L)} = K\exp(-\alpha L) \quad (\text{Eq. 17})$$

A plot of $\log_{10} \overline{V}_1(L)$ vs. L should be linear and have a slope equal to $-\frac{\alpha}{2.303}$.

Suppose $\alpha L = 2$, $r \approx 1$ (actually r is probably less than 1). Then

$$\max\left(\frac{V(L)}{\overline{V}_1(L)}\right) = \frac{1}{\sqrt{1-2r \exp(-2\alpha L)+r^2 \exp(-4\alpha L)}}$$

$$\max\left(\frac{V(L)}{\overline{V}_1(L)}\right) = \frac{1}{0.98} = 1.02 \quad .$$

The error is given by $\frac{V-V_1}{V} \times 100 = \pm 2\%$ approximately. Let us consider the case for small L and define $r = \exp(-2\beta)$ then

$$\overline{V(L)} = \frac{\overline{K}}{\sqrt{[\exp 2(\alpha L+\beta)-2 \cos(2kL)+\exp -2(\alpha L+\beta)]}}$$

$\overline{V(L)}$ occur when $\cos(2kL) = \pm 1$ so that
max,min

$$\begin{aligned} \overline{V}_{\max}(L) &= \frac{\overline{K}}{\sqrt{[\exp 2(\alpha L+\beta)-2 + \exp -2(\alpha L+\beta)]}} \\ &= \frac{\overline{K}}{2 \sinh(\alpha L+\beta)} \end{aligned}$$

and

$$\bar{V}_{\min}(L) = \frac{\bar{K}}{2 \cosh(\alpha L + \beta)} .$$

Then

$$\tanh(\alpha L + \beta) = \frac{V_{\min}}{V_{\max}}$$

and

$$\tanh^{-1}\left(\frac{V_{\min}}{V_{\max}}\right) = \alpha L + \beta . \quad (\text{Eq. 18})$$

Further

$$\tanh^{-1} \frac{V_{\min}}{V_{\max}} = \frac{1}{2} \log \frac{1 + \frac{V_{\min}}{V_{\max}}}{1 - \frac{V_{\min}}{V_{\max}}} = \alpha L + \beta$$

so that

$$\log \frac{V_{\max} + V_{\min}}{V_{\max} - V_{\min}} = 2\alpha L + 2\beta . \quad (\text{Eq. 19})$$

A plot of $\log_{10} \frac{V_{\max} + V_{\min}}{V_{\max} - V_{\min}}$ vs. L should be linear and have a

slope equal to $\frac{2\alpha}{2.303}$. The intercept should allow for calculation of r .

Details of data collection

As indicated in the previous section, two techniques were available for the measurement of the wave propagation velocity; either the wave length was measured directly by changing the probe separation at constant frequency or else the probe separation was held constant and $\{\nu_n\}^1$ satisfying Equation 15, noting that $k = \frac{\omega}{c} = \frac{2\pi\nu}{c}$, was collected within the frequency range available, 50 cps - 2000 cps. Both of these techniques were used.

Vary L technique To measure the wave length directly, we proceeded as follows:

- i) Steps previously described were carried out; see the section headed Initial steps in operation of the apparatus.
- ii) The oscillator was adjusted to some convenient frequency in the range of frequencies studied. Precise frequency control was maintained by either counting the oscillator output for 10 seconds using the Computer Measurements Co. frequency counter or

¹We shall use this notation to designate the sequence of all ν satisfying Equation 15 while keeping the probe separation, L , constant.

by beating the working oscillator output against the Hewlett Packard frequency standard oscillator. In this case, the frequency standard oscillator usually proved to be more convenient and precise. The Lissajous figures derived from beating the working oscillator against the frequency standard oscillator allowed us to keep the working frequency to within one part per 10,000 during the course of the measurement. Power to the speaker was adjusted to about 0.1 volt.

- iii) The balanced filter circuits were switched in or out of the circuit. In general, it was found that all three filters, 20 cps, 60 cps and the high pass (3 db point = 240 cps) filter could be used to gain advantage in signal to noise ratio for frequencies above 400 cps. Below this frequency the filters were switched out; the 60 cps filter was bypassed below 300 cps, then the 240 cps was switched out at 200 cps and finally the 20 cps filter was bypassed below roughly 100 cps. The two members of the balanced filter circuits were matched so closely that even in the region approaching maximum attenuation, the phase shift introduced into the circuit was small enough to be ignored. This point is discussed later.

- iv) The receiving probe was lowered to the water surface using the y axis control of the micromanipulator. The signal would immediately increase above noise level as the probe contacted the surface. The probe separation was initially set between one and two centimeters. At this point, the power amplifier output to the speaker coils was adjusted so that the detector output was at a satisfactory level. With the probe separation of one centimeter, this meant that the amplified detector output was usually between 100 mv and 1000 mv. The transducer characteristics were such that the amplitude of the sending Tee bar would fall as $\frac{1}{\omega^2}$ at constant coil voltage so that at frequencies above 1200 cps, the amplified signal from the receiving probe cartridge was usually below 100 mv with the noise level between 3 and 10 mv. The working levels just described corresponded to an amplitude of less than one micron at the Tee bar. The amplitude was always small compared to the wave length, i.e., much less than 1% of the wave length. Measurement of the sending bar amplitude as a function of frequency will be discussed later.
- v) The probe separation was changed until the elliptical Lissajous figure on the oscilloscope

formed from beating the signal from the transducer against the signal from the receiving probe showed that the two signals were inphase. At this probe separation, L_1 , there were n_1 waves residing between the probes. The probe separation was decreased (or increased if desired) until the Lissajous figure on the oscilloscope again showed that the two signals were inphase so that n_2 waves were zipping across the surface bounded by the probes L_2 cm apart. Then, referring to Equation 15, we must have that

$$\lambda = \frac{L_1 - L_2}{\Delta \bar{n}} .$$

For best precision it was convenient to plot $\Delta \bar{n}$ vs. L . The plots were always linear, e.g., see Figure 17. The inverse of the slope of this plot gave λ .

vi) The frequency was then changed and steps i through v repeated. After the first detailed plot of n vs. L described in v, much less detailed plots were needed to define the wave length at the new frequency. Usually three points were determined. The straight line through these three points always extrapolated to zero within experimental error.

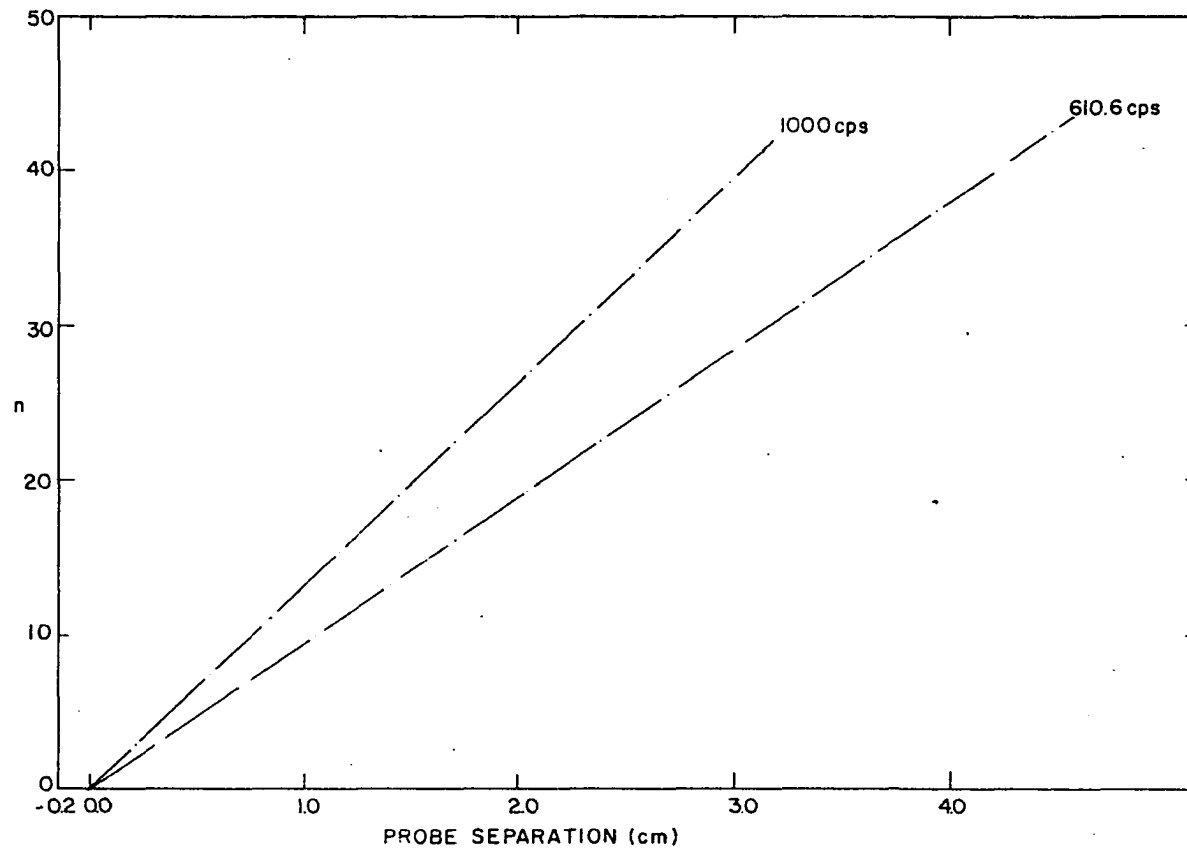


Figure 17. Dependence of wave number on probe separation

Constant L technique The second method of determining wave propagation velocity again depends upon Equation 15. Holding L constant we see that for $\theta = n\pi$

$$\lambda_n = \frac{2L}{n}, \quad n = 1, 2, 3, \dots$$

Here n refers to half-integer wave lengths. The condition that $\theta = n\pi$ holds for certain sets of frequencies symbolized by $\{v_n\}$. Collecting, in sequence, all frequencies for which the Lissajous figures implied that the two probes were either exactly inphase or exactly out-of-phase allowed the calculation of λ_n if L and n were known for any one frequency. We next describe the sequence of steps necessary for the collection and interpretation of the $\{v_n\}$ data:

- i, ii, iii) as previously stated were also followed for this method of determining velocity dispersion curves.
- iv) The run was often initiated at 1000 cps; the experimental values of n and L were established at this frequency as previously described. The probe separation was then adjusted until the Lissajous figure showed that the two probes were inphase. The probe separation was not changed during the rest of the run.
- v) The oscillator was tuned off of 1000 cps, inphase,

until a new frequency, say 1050 cps, out-of-phase, was reached: this frequency was ν_{n+1} . Again the oscillator was tuned off of 1050 cps to say 1100 cps, inphase; this frequency was ν_{n+2} . The wave lengths associated with ν_n , ν_{n+1} , ν_{n+2} had to be $\frac{2L}{n}$, $\frac{2L}{n+1}$, $\frac{2L}{n+2}$. This procedure was continued to include frequencies lower than 1000 cps.

Discussion of these techniques The y-axis intercept of the Δn vs. L plots (vary L technique) not only allowed determination of the number of waves traveling between the probes but also the effective probe separation.

Writing

$$\Delta \bar{n} = \frac{1}{\lambda} L + b$$

we see that $\Delta \bar{n} - b$ should be a number close to some integer n . Since the apparent probe separation was known to within $\frac{1}{2}\lambda$, rounding to the nearest integer gave the actual number of waves oscillating between the probes. Since the physics of the experiment require n to be integer, the rounding error must correspond to a correction to be applied to the probe separation data. This correction was always small and within the expected error associated with visual alignment of the probes. The effective zero probe separation did not

change with frequency.

It has happened that n appeared to be off by ± 1 . In this case we usually redetermined L and n at some frequency around 300 cps. The problem of determining n became really difficult only when the signal to noise ratio was less than 2:1. The signal to noise ratio was usually favorable at 200 or 300 cps even under conditions of high surface pressure. However, 1000 cps was a convenient frequency for establishing optimum operating conditions.

The two methods described above for measuring propagation velocities complement each other. The vary L technique has the advantage that small phase angle shifts with frequency are not important so long as the shift in phase angle is constant with probe separation. Any mechanical coupling contribution phase shifts at certain resonance frequencies was shown to be constant with change in L . The noise level, with filters in, was reduced to 3-5 millivolts as measured at the oscilloscope and corresponded to 3-5 microvolts at the crystal cartridge. The noise was random until the major mechanical resonance frequency, 1540 cps, was reached. The coupling at that frequency was so large that measurements could not be made there; the signal to noise ratio was very bad. However, even here the Lissajous figure showed constant phase angle with probe separation.

The major operational disadvantage of this technique

was that scanning the frequency region of interest was a long and slow process. However, one could pick a small region in the frequency range and choose for study any desired set of frequencies to show up structure features of the dispersion curves without scanning the whole range. In this sense, the vary L technique was more flexible. The major uncertainty appears to be in the measurement of λ gained from the $\Delta\bar{n}$ vs. probe separation plots. Probe separation of one centimeter or more can be measured to one part per thousand with present instrumentation; small differences in probe separation can be determined to better than one part per hundred. It is possible to determine the slope of the $\Delta\bar{n}$ vs. L plot to approximately 5 parts per thousand. Alternating between the events per 10 seconds and 10^{-5} seconds per 10 events mode of counter operation for high frequency and low frequency measurements respectively, we were able to establish frequencies to one part per ten thousand. Using the frequency standard to beat against the working oscillator, frequencies in convenient multiples of the standard oscillator could be established to better than 1 part per million. The stability of the working oscillator limited us to one part per 100,000. We were amazed that the Hewlett Packard Audio Oscillators were so stable. Resetting the working oscillator to 1 part per 100,000 was difficult, but once warmed up for several hours and set to a frequency,

the oscillator would not go off frequency by more than one part per 10,000 in an hour.

It was hard to estimate objectively an error level for the phase angle measurement necessary for both the vary L and constant L techniques. The signal to noise ratio played a very important part in this aspect of the measurement. The phase error was extremely small when the signal to noise ratio was greater than 10:1, a level usually attained except at high frequencies. One order of magnitude more of probe separation resolution should be possible before the phase angle determination limits the precision of the measurement. It should be possible to measure propagation velocities to approximately one part per 10,000 if the probe separation resolution can be increased.

The constant L technique was much faster than the vary L technique. Once L and n had been determined, the whole frequency region available, 50 cps to 2000 cps, could be scanned in frequency increments, $\nu_n - \nu_{n-1}$, of approximately 25 cps in about 30 minutes. As some reflection on Equation 15 will show, $\nu_n - \nu_{n-1}$ can be controlled by the choice of L; as L becomes larger $\nu_n - \nu_{n-1}$ will become smaller. Naturally $\nu_n - \nu_{n-1}$ will vary somewhat with frequency at a given probe separation, but the trend is still true. It was possible, then, by collecting $\{\nu_n\}$ at various probe separations to search a frequency region as thoroughly as

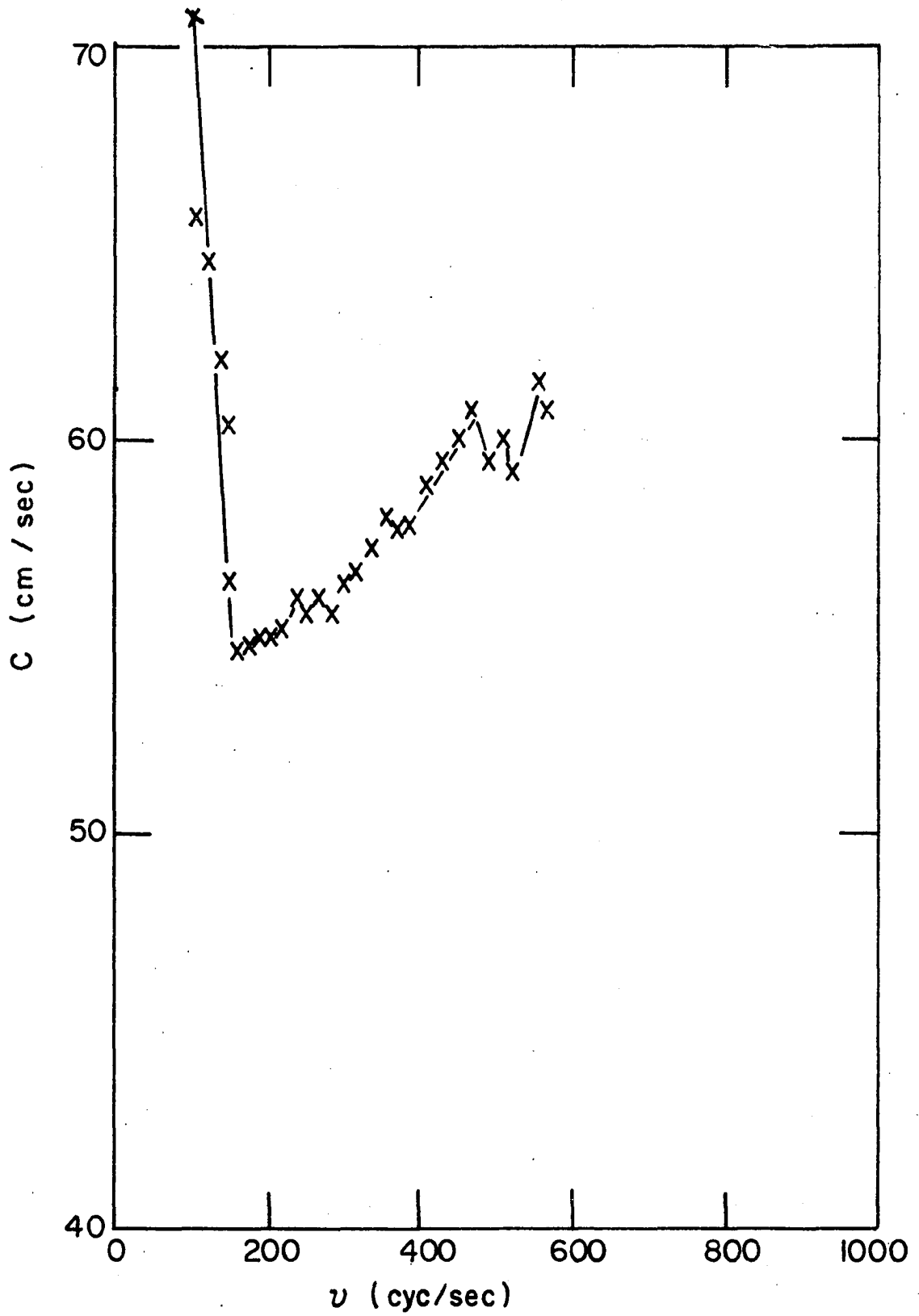
desired. Difficulties arise with the high frequency end of the available range. Damping and maximum wave amplitudes were such that the probes had to be closer in order to realize a sufficient signal to noise ratio. The result was that many more sets of $\{v_n\}$ data had to be collected in high frequency regions in order to gain the desired resolution. It was found that a much lower signal to noise level was tolerable in the constant L mode of measurement; a signal to noise ratio of 1.5:1 was sufficient to find $\{v_n\}$. The maximum probable error increased to between 0.5 and 1%. Fortunately the eye must resolve only an elliptical Lissajous figure going to a linear Lissajous figure in order to find $\{v_n\}$.

The major difficulty with the constant L technique was that the probes were weakly coupled through the air and supporting structure. In general, coupling of this type was of the order of the intrinsic noise level of the circuits; at most frequencies the noise level did not increase beyond 5 mv compared to the intrinsic noise level, 3 mv, found with the vibrating probe at rest. However, there were a number of resonance frequencies, e.g., the mechanical resonance frequency of the sending probe was 1540 cps. These resonance frequencies were very bothersome during the early phases of this experimental effort and led to some ridiculous results. We found that members of $\{v_n\}$ would be shifted in the

neighborhood of the resonance frequency or else pseudo members of $\{\nu_n\}$ would appear. This last possibility produced the result shown in Figure 18; a rational, consistent assignment of n could not be made due to the ghost frequencies. The previously discussed transducer design along with careful placement of the coil in the speaker magnet eliminated much of the trouble. Combining data, Figure 19, from three $\{\nu_n\}$ sets at three different probe separations attested to this assertion. Even so there was some shift in frequency due to resonance since $\nu_n - \nu_{n-1}$ vs. ν_n plots were not quite smooth; however, the problem appears to be tractable. It should be easy to determine whether ν_n shifts on monolayers are due to resonance frequency shifts or anomalous dispersion through the monolayer. $\nu_n - \nu_{n-1}$ vs. ν_n curves need only to be compared to the analogous clean water curves.

Wave damping determination The wave damping coefficient, α , was established by the vary L technique. In principle, α could be evaluated with the constant L technique using Equation 15 if detailed frequency vs. phase angle data is known. It was much easier experimentally, and also more direct, to calculate α from crystal receiver output vs. probe separation data. Equations 17 and 19 pertain to this approach. As these equations indicate, the measurements naturally separate into two cases: the probe

Figure 18. Velocity dispersion calculated from a set of constant L data containing "ghost" frequencies (myristic acid monolayer, $\pi = 0$ d/cm)



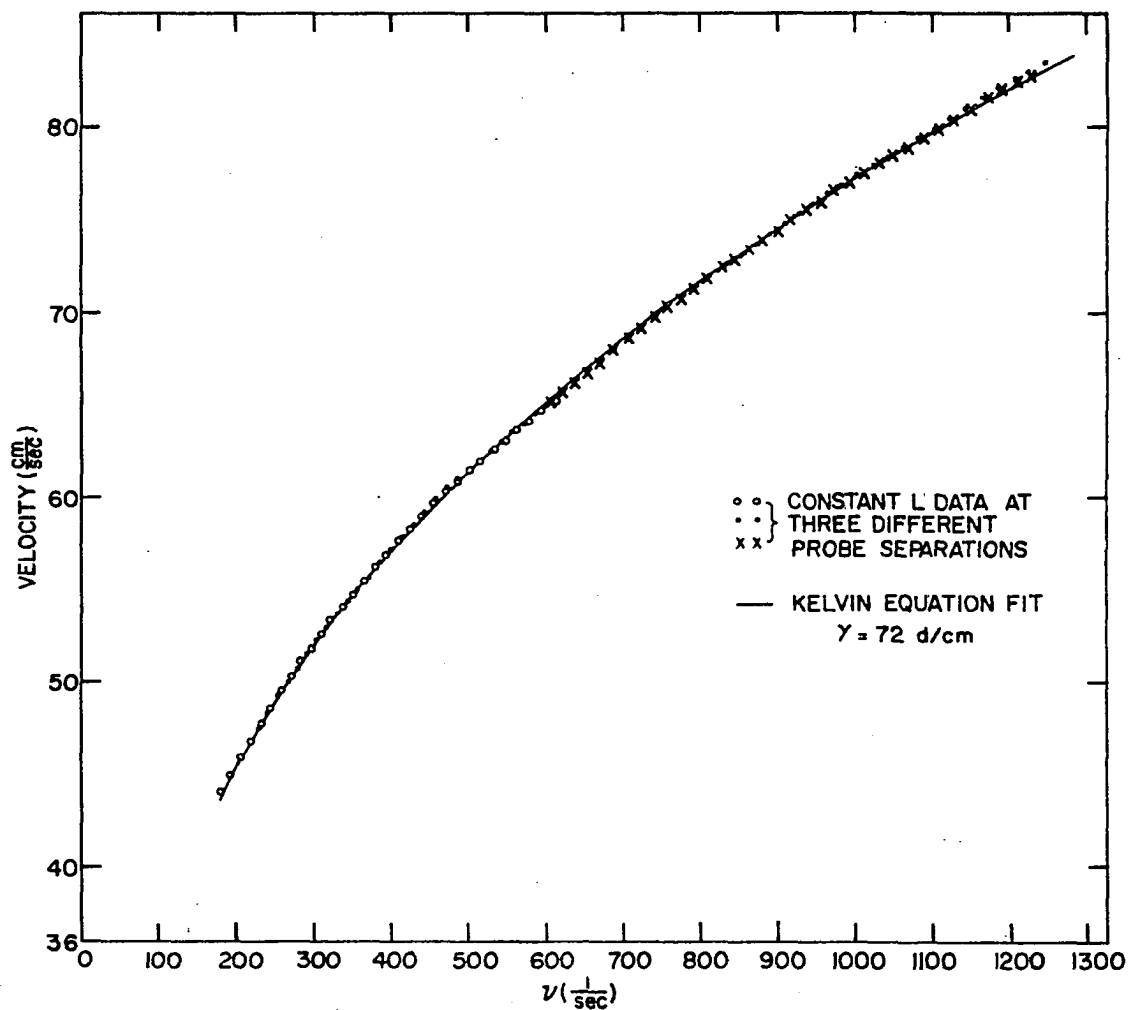


Figure 19. Velocity dispersion on monolayer free water calculated from constant L data sets

separation was small, $\alpha L \leq 1$, and the probe separation was large, $\alpha L > 1$. In the latter case the simple exponential law was followed, see Figure 15. In the former case, we found that the receiver output went through sequential maxima and minima. This effect is predicted by Equation 16 and in fact the amplitude vs. probe separation is to follow the curve constructed from a damped sine wave superimposed on an exponential decay law. This type of damping was found experimentally, see Figure 16.

Since the plot of log cartridge output vs. probe separation was linear, the vary L procedure at large probe separation was by far the easiest and fastest of the two techniques used in the evaluation of the damping of capillary ripples. The point that had to be established was that the crystal cartridge output was truly directly proportional to the wave amplitude at the receiving bar. To check this point, we carefully measured the amplitude of the sending bar as a function of frequency and as a function of coil voltage using a Schaevitz Linear Variable Differential Transformer (LVDT).

The 003-ML LVDT was excited by 5 volts oscillating at 20 KC. The LVDT core was coupled directly to the transducer in place of the Tee bar. The piston was weighted so that the transducer load with the core in place was the same as the transducer load with the Tee bar attached. The LVDT coil

was then positioned around the core so that electrical coupling gave a secondary output of roughly 1 mv peak-to-peak. This signal was monitored by a Tektronix 545A oscilloscope with the low level plug-in unit, Tektronix Type E, as the preamplifier. A convenient sweep rate was one millisecond per centimeter. The amplitude of the probe vibration was directly proportional to the modulation level on the 20 KC output from the LVDT secondary. The 20 KC output from the LVDT had been previously calibrated and found to be a linear function of core position. A change in core position of one micron was easily measured using the low level preamplifier on the Tektronix oscilloscope. At every frequency investigated in the range 100 cps to 1400 cps, the relation between probe amplitude and speaker coil excitation potential was linear. An example of the plots collected is presented in Figure 20.

Enough data sets were collected to convince us that the Tee bar amplitude was a linear function of coil excitation voltage throughout the frequency region studied in This Thesis. Since we had calibrated the LVDT, the absolute amplitude of the Tee bar could be determined as a function of frequency at constant excitation potential. These data allowed us to adjust the Tee bar amplitude so that we could always justify the assumption that the wave amplitude was very small compared to the wave length. The wave amplitude

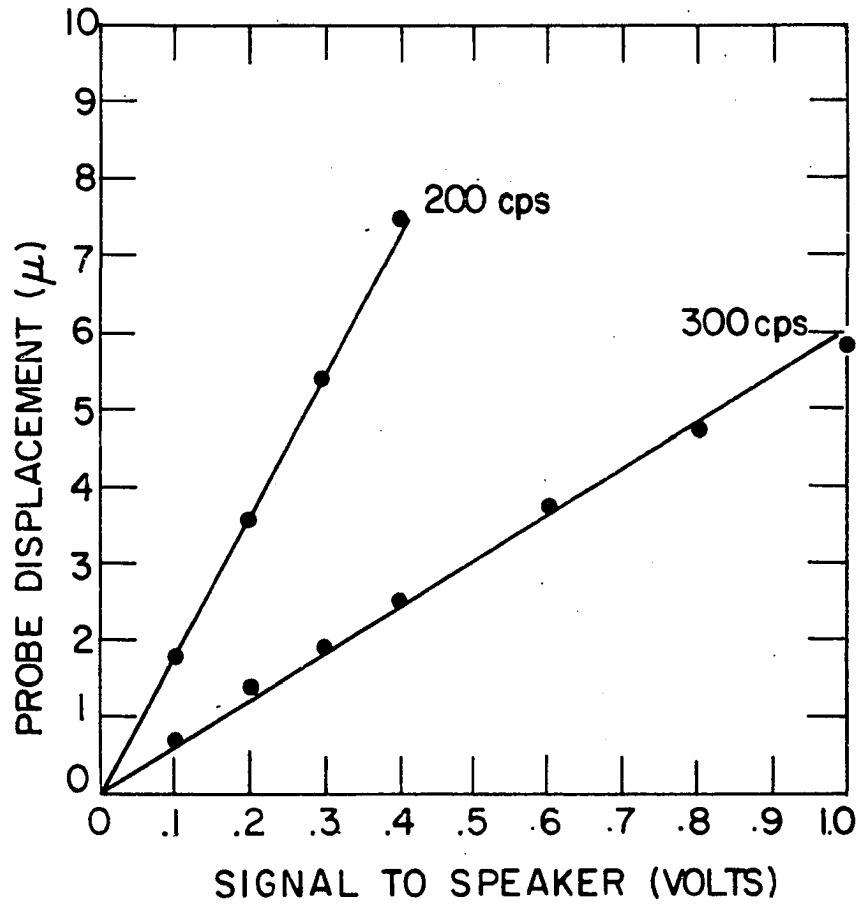


Figure 20. Dependence of sending probe amplitude on speaker coil excitation

at $x = 0$ was never larger than one micron. At high frequencies, the wave amplitude at $x = 0$ was usually smaller than 0.1 micron. Usually we had that

$$\frac{\text{Wave amplitude}}{\text{Wave length}} \approx 10^{-4} .$$

We next proceeded to establish that the crystal cartridge coupled to the receiving probe presented an output which was a linear function of the speaker coil excitation potential. The probes were brought to the clean water surface according to the previously discussed procedure. The probe separation was set to roughly 1 cm; however, a number of probe separations were used during subsequent linearity checks. The output from the crystal cartridge was monitored by a Hewlett Packard 400H A.C. vacuum tube voltmeter. The receiving probe output was then determined as a function of the speaker coil excitation at constant frequency. The output measured after preamplification did not exceed 3 volts r.m.s. Linear plots were always found no matter what probe separation or frequency conditions were chosen. Figure 21 was typical of the data collected in this phase of the experimental work.

These experiments established to our satisfaction that the output from the receiving probe was directly proportional to the wave amplitude at the receiving probe. It was

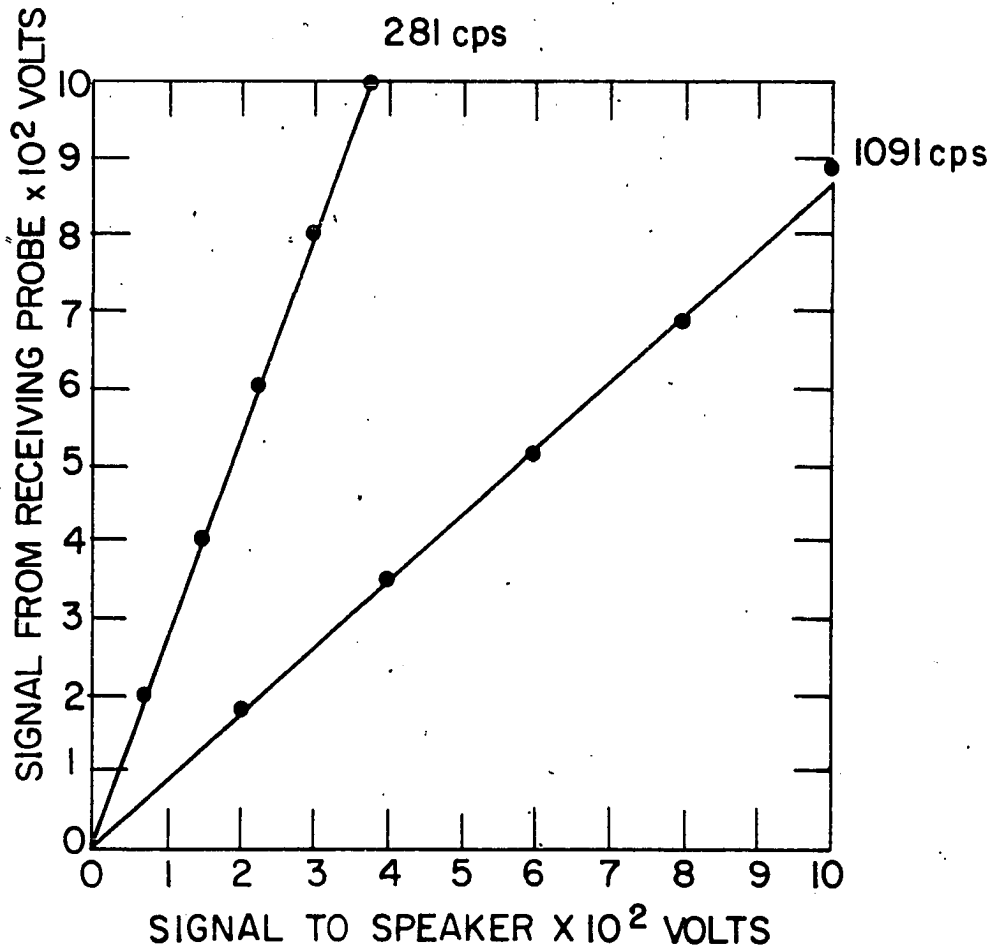


Figure 21. Dependence of crystal cartridge receiving probe output on speaker coil excitation.

not necessary to establish the proportionality constant since only amplitude ratios were needed. The flat frequency response, so dear to high-fi fans, was not found in either the speaker transducer or the receiving probe operating characteristics. However, since the vary L (at constant frequency) technique was used to measure damping characteristics, this property of the instrumentation was of little concern to us.

Discussion of the wave damping measurement When applicable, the vary L at large probe separation procedure using Equation 17 was the most precise way of finding α . The $\log_{10} V$ vs. L plots usually allowed calculation of the slope, $\frac{-\alpha}{2.303}$ to 1%. The flaw in the procedure was the fact that the signal level was low since the probe separation must necessarily be large. This disadvantage was observed with low surface tension systems at high frequencies. However, α seemed to be determined with 10% even under poor signal-noise conditions.

Clean water surfaces presented a slightly different problem. Damping was so small that very large probe separations, 2 cm or larger, were needed before Equation 17 could be used. Below 400 cps, the V vs. L curves showed maxima and minima even at probe separations of 5 cm. The micromanipulator had an extension of only 6 cm. Under these

conditions, it was more convenient to use V_{\max} , V_{\min} data to calculate α from Equation 19.

The small probe separation vary L procedure appeared to determine α to within 10%; however, the method was slow since 5 or 6 sets of V_{extrema} were needed to give sufficiently well defined envelope curves which would allow precise calculation of α . The exact positions of the extrema were hard to determine quickly without outlining the V vs. L curve as extensively as was done in Figure 16. A further complication was found in the fact that small deviations from parallel probe orientation had a very significant effect on the positions of the V_{extrema} . Undoubtedly part of the difficulty was due to the fact that at short probe separations, of the order of 1 to 6 millimeters, the surface was distorted due to slight roughness of the paraffin covering the probe surfaces.

In the case of insoluble monolayers, the surface pressure was increased by advancing the moving barrier as described in the section on the film balance. The surface pressure could be kept constant to within 0.3 d/cm during the collection of velocity and attenuation data. Small surface pressure variations during the course of a run led to some scatter in the log V vs. L data which was reflected in uncertainty in the calculation of α . This difficulty was not as pronounced in measuring propagation velocities since

these data could be collected in a much shorter time.

The soluble monolayer work was not quite so sensitive to this type of uncertainty. We filled the trough with heptanoic solution possessing a known surface tension. We would close the constant temperature chamber and allow the solution to equilibrate over night. Checking the solution surface tension at intervals demonstrated that after equilibration for 12 hours, the surface tension of the heptanoic acid solution would remain constant within 0.2 d/cm over a 4 hour period. A small fan inside the air bath switched on or off from the control panel greatly quickened the approach to equilibrium conditions. The fan was never running during the actual measurements; air movement and the fan vibration greatly increased the noise level.

Miscellaneous Comments on Technique

There are several points on technique that have not been mentioned. We wish to point out that some care must be exercised to insure homogeneity of the monolayer between the probes and elsewhere on the section of the trough constraining the monolayer. For example, stearic acid films are "solid" and thus fracture quite easily. This means that the receiving probe must be moved over the surface with care. The proper technique appears to be to raise the probe from the surface carefully with the vertical micromanipulator

control until the probe blade breaks clear of the film. The probe position is then changed by use of the proper manipulator control and the probe carefully lowered onto the film with the vertical micromanipulator control. The blade edge is sufficiently narrow so that any rupture of the film contributes very little to the error inherent in measuring the propagation parameters. It was our experience that if the probe blade was carefully paraffined and if care was exercised in lifting the probe from the surface slowly and smoothly then little rupture occurred. It usually appeared that the blade was sitting on top of a "rubber sheet" without cutting or piercing the "sheet."

To insure homogeneous monolayers, the probes were oriented perpendicular to the moving barrier, that is, parallel to the trough sides. After increasing the surface pressure by compression, sufficient time (5 minutes) was allowed to insure that any surface flow effects would have subsided.

In the case of gaseous monolayers, heptanoic acid for example, and clean water surfaces it was not necessary to raise the receiving probe from the surface in order to change probe separation. This fact increased the rate at which data could be collected for these systems.

We tried to speed data collection by use of recording techniques. The Hewlett Packard A.C. V.T.V.M. used to

monitor the crystal output on the receiving probe was slightly modified to allow recording of the signal magnitude. A 10Ω precision resistor, shunted by $50\ \mu\text{f}$, was placed in series with the V.T.V.M. meter. Shielded two lead cable tapping across the resistor was led to the floating y axis on the Autograph x-y recorder. It was necessary to completely float the recorder y axis circuit by disconnecting the $0.47\ \mu\text{f}$ capacitor from the y axis low side to the chassis ground. This was necessary since the meter circuit in the V.T.V.M. was above ground by 130 vdc plus ripple; the ripple must not be shunted to ground. The response of the recorder-V.T.V.M. system was linear on all scales and at all frequencies away from lower 60 cps harmonics. Small amplitude beats were seen at 120 cps and 180 cps.

The probe separation circuit was connected to the x axis of the recorder by way of the output from the Kintel D.C. V.T.V.M. acting as the null detector in the double potentiometer probe separation circuit. This allowed us a sensitivity of two chart inches per millimeter of probe separation change.

We were then able to record wave amplitude as a function of probe separation. This technique would have been fully automatic if we would have driven the micromanipulator probe separation axis with a slow speed motor. Unfortunately

the crystal receiving cartridge was very sensitive to vibration; even careful movement of the rack and pinion micro-manipulator axis control introduced very high noise levels swamping out the wanted signal. The recording was done semi-automatically. We would first change the probe separation with the recorder pen lifted and the gain switched to a very low sensitivity. Then we could quickly switch to high gain and lower the pen to dot the output level on the chart. This process was repeated until the whole curve was defined. Figure 16 was produced in this fashion.

This procedure was somewhat faster than reading a meter and it was easier to define the extrema points in the collection of attenuation data at small probe separations. However, data collection for the linear region was done without the x-y recorder circuit since the data would have needed replotting as the log of the crystal cartridge output.

The frequency of the Hewlett Packard standard oscillator was checked against the National Bureau of Standards broadcasting station WWV. This station could be heard on at least one of the frequencies, 5, 10 or 15 mc, using a Hallicrafter model SX-71 receiver, with sufficient clarity to obtain a check on the oscillator frequency to at least one part per million.


Suggestions for Improved Instrumentation

We suggest that the probe separation be controlled by a micrometer screw device; probe separations could then be determined to within one micron. This modification would allow a higher level of precision on the propagation velocity determination. Since it would be advantageous to record automatically amplitude vs. probe separation data, we suggest that thought be given to a change in the probe mounting arrangements. For example, mount the receiving probe in a fixed position with maximum mechanical decoupling from the micromanipulator frame, and mount the sending probe on the micromanipulator so that now the micromanipulator movement would change the position of the sending probe with respect to the fixed receiving probe. The sending probe for this arrangement must be much less massive than the present design. This might be accomplished by using a modified electro-mechanical record disk cutting head. These are available commercially¹ and are roughly the same size as the crystal phonograph cartridges used in this study. Continuous, motorized movement of the micromanipulator control should be possible without inducing excess mechanical noise into the receiving circuit.

¹An example of such a device is the M-41 Series Cutting Head produced by the Astatic Corporation, Conneaut, Ohio.

Commercial amplifiers are available with the feature that the output is delivered as the logarithm of the input signal. This type of amplifier coupled with automatic probe separation advance should allow us to speed the attenuation coefficient data collection process considerably.

It would be highly desirable to move the equipment to some area of the project that has less building vibration and fewer sources of electrical noise, e.g., induction furnace converters.

It is suggested that the moving barrier device be completely redesigned. A design closer to that mentioned by Harkins (2) would be desirable. The lead screw should still be coupled to a Helipot to give continuous area readout. However, the  shaped arm used to couple the barrier to the lead screw developed sufficient torque while pushing the teflon barrier to partially bind the lead screw bushing so that at higher barrier velocities the barrier movement was somewhat rougher than we had wished to tolerate. We suggest that a continuously variable, 5:1 - 1:5, motor coupling such as that made by Merton Instruments Co. (Series 2A Variable Reducer) be used to vary the barrier velocity; gear trains, while adequate, were not convenient.

Toward the end of the experimental phase, it was found that a substantial increase (factor of 5) in signal to noise ratio could be realized by a slight modification of the

position of the razor blade on the shank going to the crystal cartridge. We soldered the shank to the end of the blade rather than in the exact center of the blade. Dissection of a spare crystal cartridge of the type we were using confirmed our hypothesis that the crystal mounting detail produced maximum signal output with twisting motion. We were worried that allowing the receiving blade to transmit the fluid motion as a torque would upset the wave reflection boundary conditions assumed in the data reduction equations. This did not appear to be so. We suggest that transducers be surveyed in hopes of finding a system which would sense vertically constrained motion alone and have a band pass below 50 cps.

Film Spreading

The insoluble films were spread from solution using well documented techniques, see for example discussions by Adam (1), Harkins (2), Adamson (3), and Davies (4). Solvent retention by the monolayer was an early problem solved satisfactorily by using low boiling petroleum ether. Benzene was not satisfactory since it appeared to take 4 to 12 hours for the solvent to evaporate to the point where force-area curves were reproducible. This problem is discussed extensively by LaMer (31).

Egg albumin films presented the usual problem of

incomplete spreading. Various approaches are discussed in the literature by Bull (33) and Trurnitt (34) for example. We found that spreading from a single crystal gave the best results as far as reproducible compression characteristics were concerned. The co-area of 0.9 meters/mg compared fairly well with literature co-area quotations; Bull claims 0.9 meters/mg on K_2SO_4 solution, Trurnitt claims 1.1 meters/mg. We attempted Trurnitt's "sophisticated" approach to protein film spreading, flowing the protein solution down the sides of a glass rod sitting in the trough, without much success. The technique apparently requires more art than Trurnitt (34) admits in his ten page paper on the subject.

The surface tension of the heptanoic acid solutions, forming soluble surface films, was measured with a Cenco-DuNoy tensiometer to ± 0.1 d/cm. The correction formula of Zuidema and Waters (35) was used to give the actual surface tension of the solutions to ± 0.2 d/cm.

Materials

All of the insoluble film forming compounds had been recrystallized several times from various solvents. The melting points of these compounds were very sharp and checked literature values to within $\pm 1^\circ C$. The long chain fatty acids had been prepared by Armour Inc. The heptanoic acid, the octadecanol and the hexadecanol were Eastman White

label chemicals.

The petroleum ether and benzene were distilled through an Oldershaw 30 plate distillation column. The middle fractions boiling at 36°C and 80°C were retained as monolayer spreading solvents. Solvent alone was spread on the trough to check for possible contamination. These experiments indicated that solvent impurities would contribute at most 0.05% error to the observed film pressure.

The esters were supplied by Proctor and Gamble. The polyvinyl acetate, used as received, was supplied by Interchemical Co.

Distilled water used for this experiment was first obtained from a Barnstead distillation column used to produce conductivity water for use in the undergraduate physical chemistry laboratory program. The surface tension was usually only 0.3 d/cm below literature value at 25°C . Later an all fused silica continuous double distillation column was purchased from Engelhard Industries, Inc. Initially the surface tension obtained from the double distillation of tap distilled-deionized water was 0.5 to 0.4 d/cm lower than the literature value. It appeared that some fairly long chain amine was distilling over with the water. A carbon black adsorption column in stream just before the tap distilled water entered the first stage pot apparently eliminated the offending compound. Surface tension of the still output was

0.1 to 0.2 d/cm below the literature value of 71.9 d/cm quoted from Lange's Handbook (36). This water was sufficiently clean for our purpose. Using this triply distilled water, sufficient contamination to warrant discontinuing the experiment in progress would accumulate only after 8 hours of use.

RESULTS

Three sets of data were collected for each system investigated; the force-area isotherms, the ripple propagation velocity dispersion, and the ripple damping coefficient dispersion. We will present our data in both tabular and graphic form. We will shorten the tables associated with the constant L velocity technique by including only enough data to define the dispersion curves.

We divide this section into two parts: the presentation of the experimental data and the presentation of the machine calculation method used to extract numbers from the theory developed in a previous section.

Theoretical Calculation

We were not able to put the full theory into equations that would be sufficiently compact to allow fast hand computation. We decided to use electronic computer methods to calculate the sets of numbers needed to compare our theory with the experimental results. While some programming was done on the IBM 704 machine located at the University of Wisconsin, most of the computations were accomplished on the "Cyclone" computer located at this University. It is the purpose of this subsection to present the problem outline from which the program for the

calculation was derived. The data calculated from the theory will be presented graphically along with the experimental comparison and will not be tabulated in This Thesis.

Logic outline

This outline includes only the logic portion of the programs written for the various computations. The actual calculations were done with subroutine programs to be described later. The outline follows:

1. Input alphabetic.¹
2. Output alphabetic.
3. Input constants.
4. Input into permanent storage locations N_1 values of each of the parameters Z_2 , Z_3 , Z_4 , Z_5 and Z_6 (a total of $5 \times N_1$ numbers) corresponding to a given surface pressure and N_1 different frequencies.
5. Load index register for N_1 calculations.
6. Transfer one each of the Z_4 , Z_5 and Z_6 values to temporary memory locations for calculation; store $Z_2 = 0$, $Z_3 = 0$ in the proper temporary locations for the calculation.
7. Perform the calculation as a subroutine and output the resulting Z_1 value.
8. Have we performed the calculation N_1 times? If no, then store the next values of Z_4 , Z_5 and Z_6 in

¹Table headings were first stored in the computer memory, then immediately punched out on paper tape.

temporary locations; loop back to order 7. If yes, then continue to the next order in the program.

9. Load the index registers needed for subsequent looping.

-
10. Transfer all values of Z_2 from permanent storage locations to working locations.
11. Transfer one each of Z_2 , Z_3 , Z_4 , Z_5 and Z_6 to temporary locations for use in the calculation subroutine.
12. Perform the calculation subroutine and output Z_1 .
13. Have we performed this operation N_1 times? If no, then store the next values of Z_2 , Z_3 , Z_4 , Z_5 and Z_6 in the temporary locations for use in the calculation subroutine and loop back to order 12. If yes, then divide Z_2 values stored in the working locations by a constant and store back in working locations.¹
14. Have we performed this operation N_2 times? If no, then loop back to order 11 and start the calculation sequence again. If yes, then multiply all Z_3 values by a constant and store in the Z_3 locations erasing previous Z_3 values.²
15. Have we performed this operation N_3 times? If no, then loop back to order 10 and start the sequence again.³ If yes, then stop and prepare for input of the next data table.

¹Only the k_v values were modified by this order, k_e values were not changed at this point in the calculation.

² k_e values were modified by this order.

³The first consequence of this order was to recopy the original k_v values into the working locations.

The logic portion of the program not only generated the values of the visco-elastic constants, k_e and k_v , but it also directed the orderly computation of the reduced ripple damping coefficient dispersion and the reduced ripple velocity dispersion using all permutations of the internally generated visco-elastic parameters. The logic was designed so that any one of the parameters could be calculated in terms of the others through use of the proper subroutine.

Subroutines

The theory leads, both in the insoluble and soluble monolayer cases, to the requirement that a 2 x 2 complex determinant involving the quantities Z_1, Z_2, \dots, Z_6 must have a zero value. This condition furnishes two equations in these 6 variables. Since the relation

$$Z_6 = 2Z_4Z_5^2$$

holds, a total of three relations connect these six variables, permitting three of them to be established in terms of the other three variables.

Three subroutines were written for this study; the calculation of Z_1 dispersion for the insoluble monolayer case, the calculation of Z_6 dispersion for the insoluble monolayer case, and the calculation of Z_1 dispersion for the

soluble monolayer case. We found that the imaginary part of the complex determinant could be fairly easily solved for $Z_6 - 1$ so that these terms could be eliminated from the real part of the complex determinant. While Z_6 still appeared in the formula used to calculate Z_1 , the approximation $Z_6 = 1$ was consistent with the degree of approximation already assumed. These points will be considered later. The final equations derived in the soluble monolayer case and the insoluble monolayer case were both quadratic in Z_1 . The quadratic formula was used to calculate the roots; only the negative root was of physical interest. The subroutine program was, in this case, purely arithmetic.

The algebraic manipulation required to solve for Z_6 after eliminating Z_1 from the real and imaginary parts of the complex determinant was horrendous. In order to simplify the algebra, all terms second order and above in Z_1 were ignored. Even so the final equation was a cubic in Z_6 ; however, the zero was conveniently found by the Newton-Raphson (N.R.) iteration technique (37). If we let $f(Z_6)$ be given by

$$f(Z_6) = AZ_6^3 + BZ_6^2 + CZ_6 + D \quad , \quad (\text{Eq. 1})$$

then we seek a Z_6 such that

$$f(Z_6) = 0 \quad . \quad (\text{Eq. 2})$$

The coefficients A, B, C and D are complicated algebraic functions of Z_2 , Z_3 , Z_4 and Z_5 . The N.R. formula for finding members of the sequence $\{Z_{6k}\}$ reads

$$Z_{6k} = Z_{6(k-1)} - \frac{f[Z_{6(k-1)}]}{f'[Z_{6(k-1)}]} \quad . \quad (\text{Eq. 3})$$

If $f'(Z_6) = 0$ and $f''(Z_6)$ is finite, then the convergence factor goes to zero if and only if $Z_{6k} \rightarrow Z_6$.

In view of Equation 1, Equation 3 can be written as

$$Z_{6k} = \frac{2AZ_6^3(k-1) + BZ_6^2(k-1) - D}{3AZ_6^2(k-1) + 2BZ_6(k-1) + C} \quad . \quad (\text{Eq. 4})$$

Since we knew experimentally that the zero for this equation must be in the interval (0.9, 1.0), $Z_6 = 0.90$ was used as the initial guess in all of the iteration calculations. This number was generated in the subroutine so that the main program would not have to be changed to allow the input of Z_{60} values.

The logic outline for the N.R. subroutine follows:

1. Calculate and store the coefficients A, B, C and

D using values of Z_2 , Z_3 , Z_4 and Z_5 supplied by the main program.

2. Calculate and store the initial guess, $Z_6 = 0.90$, from the constants stored by the main program.

3. Calculate and store Z_{61} from Z_{60} using Equation 4.

4. Calculate and store the magnitude of $Z_{61} - Z_{60}$.

5. Is

$$|Z_{61} - Z_{60}| - 10^{-6}$$

negative?

If no, then loop back to order 3 using Z_{6k} in place of $Z_{6(k-1)}$ for $k = 1, 2, 3, 4 \dots$

If yes, then output Z_{6k} and transfer back to the main program.

We checked the rate of convergence of the iteration during the first run of this program by printing out each member of $\{Z_{6k}\}$ rather than only the last member of the truncated sequence. Usually 2 to 4 iterations were sufficient to reach the desired error level. In subsequent runs, only Z_{6k} was punched out.

It was interesting to note that the machine time for calculating a set of 125 different Z_6 values was approximately $1\frac{1}{2}$ minutes. The similar calculation for Z_1 using the quadratic formula ran only slightly faster, approximately $1\frac{1}{4}$ minutes. The iteration method was apparently quite efficient.

Experimental

It was impractical to tabulate all of the "raw" data from which the ripple propagation parameters were calculated; however, at least one example of the less obvious methods of data work-up is presented. The general data collection and processing methods were extensively discussed in the experimental section; however, comments will be made concerning special conditions or difficulties associated with specific systems.

Force-area curves were recorded before each ripple dispersion data set was determined. During each run the spreading pressure was carefully monitored with the automatic recording surface balance so that any small change (0.5 d/cm), usually to a lower pressure, occurring during an experiment could be corrected by slowly advancing the moving barrier until the original spreading pressure was regained. Large changes in spreading pressure usually implied a barrier leak in which case the run was discontinued.

The surface pressure transducer was first carefully calibrated and then the films were spread to convenient limiting areas for the ripple dispersion measurements. Enough preliminary film balance work had been done to ensure that the force-area curves corresponded to published results. The previously mentioned book by Harkins (2)

compiles much of the pertinent film balance work. While we needed accurate spreading pressure information with each ripple dispersion data set, the complete force-area curves were used only to find the spreading pressures corresponding to phase changes.

Water

The theory derived in This Thesis should certainly be valid for the limiting case $k_e = k_v = 0$. These conditions should hold for surfactant free distilled water surfaces. It was important to collect sufficient data to check each aspect of the experimental technique and to compare these results with the limiting equations of the theory. Since wave damping is comparatively slow for this system, we were able to utilize the maximum sensitivity of the instrumentation for data collection.

Table 1 is a tabulation of all the members of $\{v_n\}$ observed with the constant L technique for a probe separation of 3.01 cm. These data are shown in Figure 19 located in the previous chapter. Table 2 tabulates velocity dispersion data collected with the vary L technique.

Table 3 presents receiving probe output data for one frequency, 860 cps. The damping coefficient is calculated from these data according to Equation 19 of the EXPERIMENTAL section. Similar tables were prepared for each damping

coefficient calculated in this study. Table 4 presents the damping coefficient dispersion data obtained for this system.

Stearic acid

The force-area curve¹ is shown in Figure 22. The two linear portions of curve III, Figure 22, extrapolate to $20.5 \text{ \AA}^2/\text{molecule}$ and $24 \text{ \AA}^2/\text{molecule}$ as π goes to zero. Table 5 presents the velocity dispersion data at various surface pressures and Table 6 presents the damping coefficient data for two surface pressures, 6.2 d/cm and 16.0 d/cm.

Mixed alcohols

Monolayers of n-octadecanol and n-hexadecanol mixed 1:1 by weight were spread from petroleum ether. The force-area curve is shown in Figure 23. Table 7 presents the velocity dispersion data and Table 8 presents the damping coefficient dispersion data.

Propylene glycol monostearate

The force-area curve for this system is shown in Figure 24. Table 9 presents the velocity dispersion data and Table 10 presents the damping coefficient dispersion data.

¹The film area increases to the right in this and subsequent force-area curves.

Stearic acid - polyvinyl acetate mixed monolayers

The force area curve for this system is shown in Figure 25. Table 11 presents the velocity dispersion data and Table 12 presents the damping coefficient dispersion data.

Benzene was first used as the spreading solvent. The force-area curves were not reproducible; the film appeared to retain a fair amount of solvent. Petroleum ether was used but polyvinyl acetate is not too soluble in this solvent.

1,3 dipalmitoyl glyceryl phosphoric acid

This material did not spread well from either benzene or petroleum ether; the force-area curves were not satisfactory. Work was discontinued on this system after obtaining the dispersion data displayed in Tables 13 and 14 at $\pi = 4$ d/cm.

Egg albumin

Since authors disagree on the force-area properties of egg albumin films, see Bull (33) and Trurnitt (34), we present the results of our preliminary work in Figure 26. This material was spread from a single crystal carefully placed on the water surface. The single crystals (~ 50 μgm) were weighed on an Ainsworth microbalance to 1 microgram. The velocity dispersion and damping are shown in Tables 15 and 16. Δv vs. v_n data resulting from the constant L technique

are presented in graphical form in the next section.

Heptanoic acid

Two concentrations were examined, 4.3×10^{-3} moles/liter and 15×10^{-3} moles/liter. The vary L damping coefficient technique at large probe separation was unreliable at the higher concentration level due to very poor signal to noise ratios. The small probe separation technique appeared to yield better results. The measurements were probably complicated by the fact that the solutions tended to wet the paraffin coated parts of the transducer system. An uncertainty of roughly 15% should be assigned to the damping coefficient results.

Soluble monolayer theory requires rather complete surface tension data for the comparison of the experimentally determined and the theoretically calculated propagation parameters. The surface tension data of King (38) were used to prepare Table 20. The diffusion coefficient was taken to be 8×10^{-6} cm²/sec in accord with the assumption of Hansen and Wallace (39). The necessary derivatives were determined by graphical techniques.

Table 1. Ripple propagation velocity on monolayer free water using constant L technique, $\gamma = 71.8$ d/cm ($t = 25.0^\circ\text{C}$)

n	$\lambda = \frac{3.010}{n}(\text{cm})$	$v(\frac{1}{\text{sec}})$	$c(\frac{\text{cm}}{\text{sec}})$
13	0.2315	193.8	44.86
13.5	0.2229	205.3	45.76
14	0.2150	216.7	46.59
14.5	0.2076	228.6	47.46
15	0.2007	240.5	48.27
15.5	0.1942	253.8	49.29
16	0.1881	266.3	50.09
16.5	0.1824	278.3	50.76
17	0.1771	291.0	51.53
17.5	0.1720	303.6	52.22
18	0.1672	316.7	52.95
18.5	0.1627	330.1	53.71
19	0.1584	343.4	54.39
19.5	0.1544	355.6	54.90
20	0.1505	370.9	55.82
20.5	0.1468	385.0	56.52
21	0.1433	399.2	57.20
21.5	0.1400	413.4	57.88
22	0.1368	428.1	58.56
22.5	0.1338	442.5	59.21
23	0.1309	457.3	59.86
23.5	0.1281	472.0	60.46
24	0.1254	486.5	61.01
24.5	0.1229	500.7	61.54
25	0.1204	515.3	62.04
25.5	0.1180	529.5	62.48
26	0.1158	544.0	62.99
26.5	0.1136	558.9	63.49
27	0.1115	573.9	63.99
27.5	0.1094	589.5	64.49
28	0.1075	606.1	65.16
28.5	0.1056	622.3	65.71

Table 1. (Continued)

n	$\lambda = \frac{3.010}{n}(\text{cm})$	$\nu(\frac{1}{\text{sec}})$	$c(\frac{\text{cm}}{\text{sec}})$
29	0.1038	638.7	66.29
29.5	0.1020	655.5	66.86
30	0.1003	672.4	67.44
30.5	0.09869	689.5	68.04
31	0.09710	706.7	68.62
31.5	0.09556	724.1	69.19
32	0.09406	742.0	69.79
32.5	0.09262	759.9	70.38
33	0.09121	777.8	70.94
33.5	0.08985	795.2	71.45
34	0.08853	813.8	72.05
34.5	0.08725	831.9	72.58
35	0.08600	850.3	73.13
35.5	0.08479	869.1	73.69
36	0.08361	888.2	74.26
36.5	0.08246	907.4	74.82
37	0.08135	926.0	75.33
37.5	0.08027	945.2	75.87
38	0.07921	964.6	76.41
38.5	0.07818	983.9	76.92
39	0.07718	1003.3	77.43
39.5	0.07620	1023.0	77.95
40	0.07525	1042.4	78.44
40.5	0.07432	1062.5	78.96
41	0.07341	1081.9	79.42
41.5	0.07253	1102.1	79.93
42	0.07167	1122.7	80.46
42.5	0.07082	1143.3	80.97
43	0.07000	1164.7	81.53
43.5	0.06919	1184.5	81.96
44	0.06841	1205.7	82.48
44.5	0.06764	1224.9	82.85
45	0.06689	1246.4	83.37

Table 2. Ripple propagation velocity on monolayer free water using vary L technique, $\gamma = 71.8$ d/cm ($t = 25.0^\circ\text{C}$)

$\nu(\frac{1}{\text{sec}})$	λ (cm)	$c(\frac{\text{cm}}{\text{sec}})$
100	0.362	36.2
150	0.276	41.4
200	0.225	45.0
240	0.201	48.2
300	0.174	52.2
343	0.158	54.2
400	0.142	56.8
450	0.131	59.0
500	0.123	61.5
540	0.116	62.6
600	0.108	64.8
700	0.097	67.9
750	0.0943	70.7
800	0.0896	71.7
900	0.0830	74.7
1000	0.0769	76.9
1180	0.0690	81.4

Table 3. Amplitude data treatment for small probe separation, vary L technique, on monolayer free water, $\nu = 860$ cps ($t = 25.0^\circ\text{C}$)

Probe separation ^a l/A (cm)	Cartridge output		$\frac{V_{\max} + V_{\min}}{V_{\max} - V_{\min}}$
	V_{\max} (mv)	V_{\min} (mv)	
0.710	462	(135) ^b	1.826
0.738	(444)	136	1.883
0.766	425	(137)	1.951
0.795	(408)	138	2.022
0.824	390	(138)	2.095
0.852	(375)	139	2.178
0.882	360	(139)	2.258
0.906	(348)	139	2.330
0.934	338	(138)	2.380

^aMultiply by 0.745 to convert to cm.

^bEach number enclosed in parentheses was read from the envelope curves passing through the maximum and minimum points on the plot of the receiving probe output as a function of probe separation. The numbers not enclosed in parentheses were the experimental maximum or minimum signal levels occurring at the indicated probe separation.

Table 4. Damping coefficient dispersion for monolayer free water, $\gamma = 71.8$ d/cm ($t = 25.0^\circ\text{C}$)

Small probe separation		Large probe separation			
$\nu(\frac{1}{\text{sec}})$	$\alpha(\frac{1}{\text{cm}})$	$\nu(\frac{1}{\text{sec}})$	$\alpha(\frac{1}{\text{cm}})$	$\nu(\frac{1}{\text{sec}})$	$\alpha(\frac{1}{\text{cm}})$
306	0.226	600	0.733	467	0.728
467	0.550	700	0.747	594	0.733
594	0.688	800	0.900	860	1.025
860	0.831	900	1.008	1000	1.07
1000	0.974	1000	1.086	1076	1.082
1076	1.117	1100	1.160	1201	1.28
1201	1.257	1200	1.237	1724	1.785
		1300	1.366		
		1400	1.517		

Figure 22. Dependence of spreading pressure on area per molecule for stearic acid monolayers

The curves have been displaced along the area axis relative to curve I. The spreading solvent was petroleum ether.

- I. Curve was run 5 minutes after spreading
- II. Curve was run 15 minutes later
- III. Curve was run 4 hours later

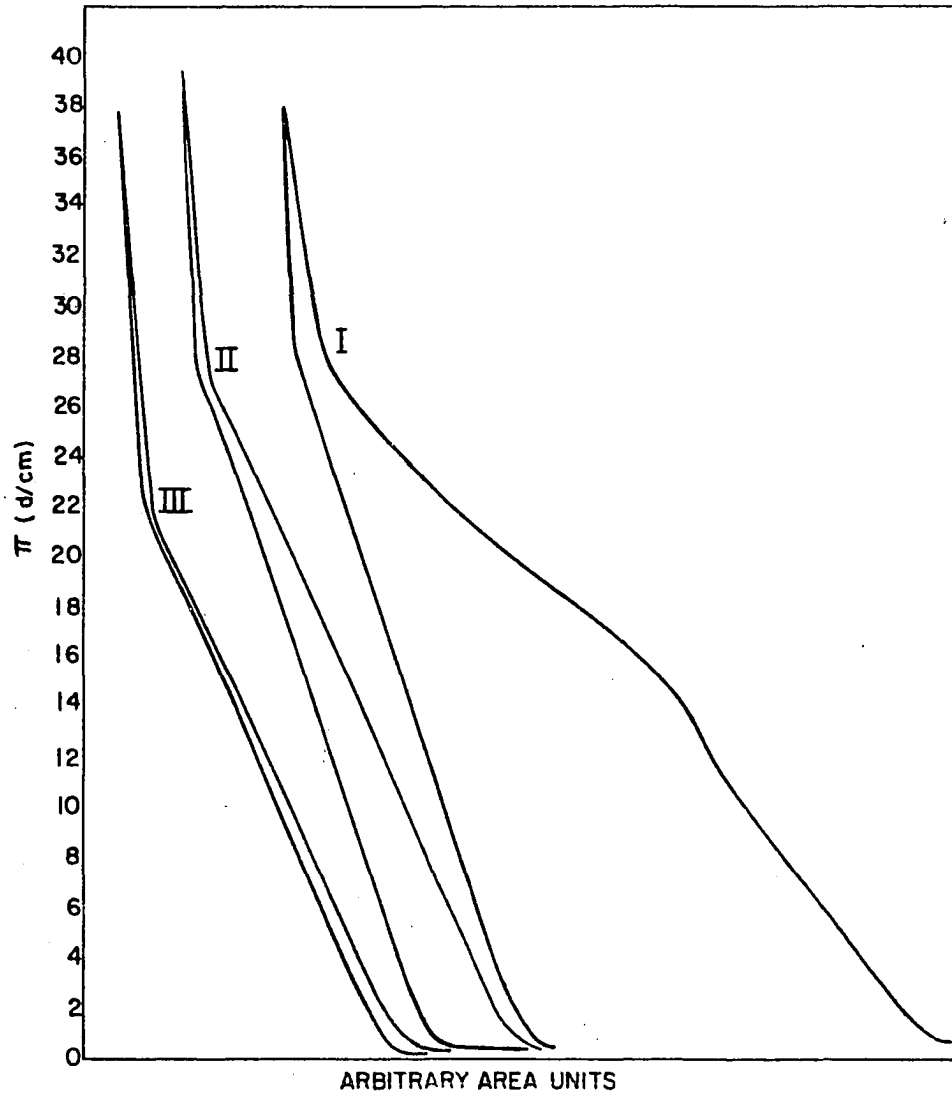


Table 5. Velocity dispersion data for stearic acid monolayers ($t = 25.0^{\circ}\text{C}$)

$v(\frac{1}{\text{sec}})$	$c(\frac{\text{cm}}{\text{sec}})$	$v(\frac{1}{\text{sec}})$	$c(\frac{\text{cm}}{\text{sec}})$	$v(\frac{1}{\text{sec}})$	$c(\frac{\text{cm}}{\text{sec}})$
<u>$\pi = 0.0 \text{ d/cm}$</u>		<u>$\pi = 5.0 \text{ d/cm}$</u>		<u>$\pi = 10.0 \text{ d/cm}$</u>	
200	44.5	660	64.50	200	42.3
300	50.9	751	67.27	300	48.5
400	55.9	845	69.87	400	53.3
500	60.0	942	72.32	500	57.1
600	63.7	1037	74.31	636	62.14
700	67.0	1136	76.32	724	64.86
800	69.9	1238	78.28	815	67.39
900	72.6	1348	80.50	907	69.64
1000	75.0	1458	82.42	1000	71.66
1100	77.4	-	-	1095	73.56
1200	79.5	-	-	1194	75.50
-	-	-	-	1296	77.40
-	-	-	-	1407	79.59
<u>$\pi = 15 \text{ d/cm}$</u>		<u>$\pi = 20 \text{ d/cm}$</u>		<u>$\pi = 25 \text{ d/cm}$</u>	
608	59.41	200	40.2	630	56.44
694	62.17	300	45.8	709	58.63
781	64.58	400	50.5	791	60.73
870	66.80	500	54.2	876	62.77
960	68.79	582	56.87	961	64.56
1052	70.67	661	59.21	1048	66.27
1146	72.46	746	61.69	1135	67.78
1244	74.29	832	63.88	1228	69.47
1351	76.43	919	65.86	1328	71.38
1458	78.37	1007	67.65	1423	72.84
-	-	1099	69.49	-	-
-	-	1193	71.25	-	-
-	-	1289	72.92	-	-
-	-	1391	74.77	-	-
-	-	1495	76.53	-	-

Table 6. Damping coefficient dispersion data for stearic acid monolayers. ($t = 25.0^{\circ}\text{C}$)

$\pi = 6.2 \text{ d/cm}$		$\pi = 16.0 \text{ d/cm}$	
$\nu(\frac{1}{\text{sec}})$	$\alpha(\frac{1}{\text{cm}})$	$\nu(\frac{1}{\text{sec}})$	$\alpha(\frac{1}{\text{cm}})$
600	1.54	600	1.77
700	1.79	700	2.00
800	2.03	800	2.26
900	2.27	900	2.44
1000	2.40	1000	2.70
1100	2.62	1100	2.99
1200	2.96	1200	3.03
1300	3.11	1300	3.26
1400	3.34	1400	3.54

Figure 23. Dependence of spreading pressure on area per molecule for the mixed monolayer system octadecanol and hexadecanol

The curves, recorded several hours apart, have been shifted along the area axis. The spreading solvent was petroleum ether.

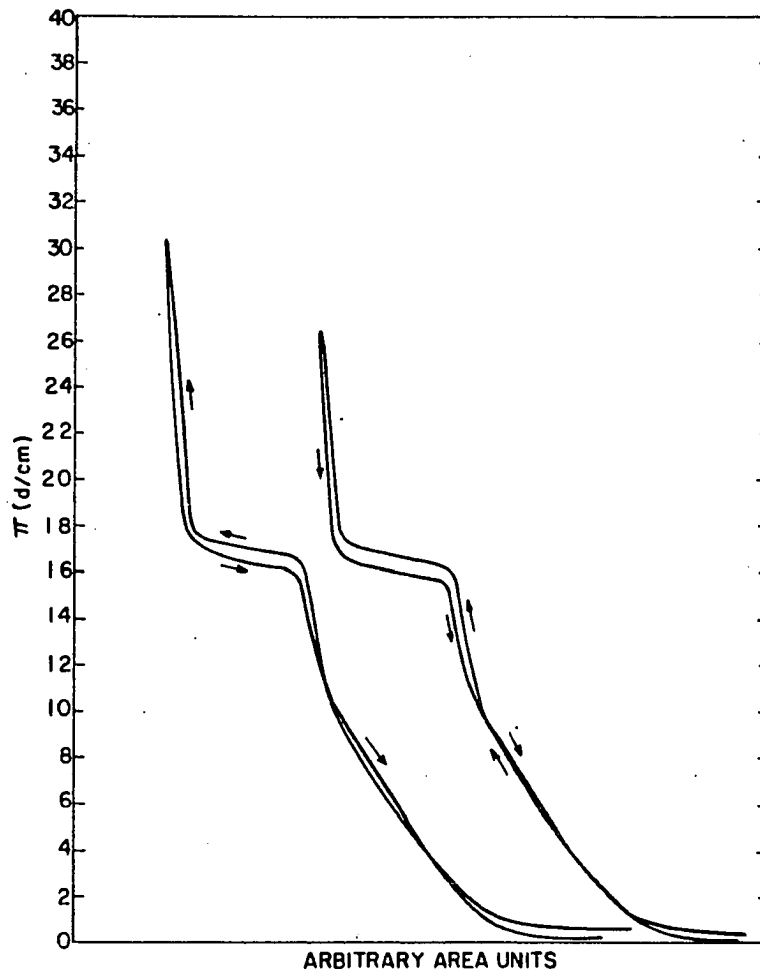


Table 7. Velocity dispersion data for 1:1 mixed monolayers of n-octadecanol and n-hexadecanol ($t = 25.0^{\circ}\text{C}$)

$v(\frac{1}{\text{sec}})$	$c(\frac{\text{cm}}{\text{sec}})$	$v(\frac{1}{\text{sec}})$	$c(\frac{\text{cm}}{\text{sec}})$
<u>$\pi = 0.5 \text{ d/cm}$</u>		<u>$\pi = 9.5 \text{ d/cm}$</u>	
265	48.81	248	45.68
348	53.42	325	49.89
439	57.77	410	53.96
535	61.58	500	57.55
638	65.27	597	61.07
746	68.71	698	64.28
857	71.73	804	67.30
971	74.52	911	69.92
1085	76.86	1021	72.33
1202	79.07	1132	74.46
1331	81.72	1249	76.69
1465	84.32	1373	79.03
-	-	1501	81.30
<u>$\pi = 16.4 \text{ d/cm}$</u>		<u>$\pi = 24.5 \text{ d/cm}$</u>	
235	43.29	286	43.90
307	47.12	364	47.90
387	50.93	444	51.10
473	54.44	526	53.81
564	57.70	619	57.01
659	60.69	714	59.76
760	63.61	813	62.40
863	66.23	912	64.61
969	68.64	1014	66.70
1074	70.65	1118	68.64
1182	72.57	1225	70.51
1299	74.77	1340	72.59
1423	77.08	1460	74.69

Table 8. Damping coefficient dispersion data for 1:1 mixed monolayers of n-octadecanol and n-hexadecanol ($t = 25.0^{\circ}\text{C}$)

$\pi = 0.5 \text{ d/cm}$		$\pi = 9.5 \text{ d/cm}$	
$\nu(\frac{1}{\text{sec}})$	$\alpha(\frac{1}{\text{cm}})$	$\nu(\frac{1}{\text{sec}})$	$\alpha(\frac{1}{\text{cm}})$
600	1.52	600	1.63
700	1.81	700	1.81
800	1.97	800	2.03
900	2.17	900	2.20
1000	2.44	1000	2.49
1100	2.52	1100	2.74
1200	2.62	1200	2.84
1300	3.19	1300	3.34
1400	3.34	1400	3.26

Figure 24. Dependence of spreading pressure on area per molecule for propylene glycol monostearate

The spreading solvent was petroleum ether.

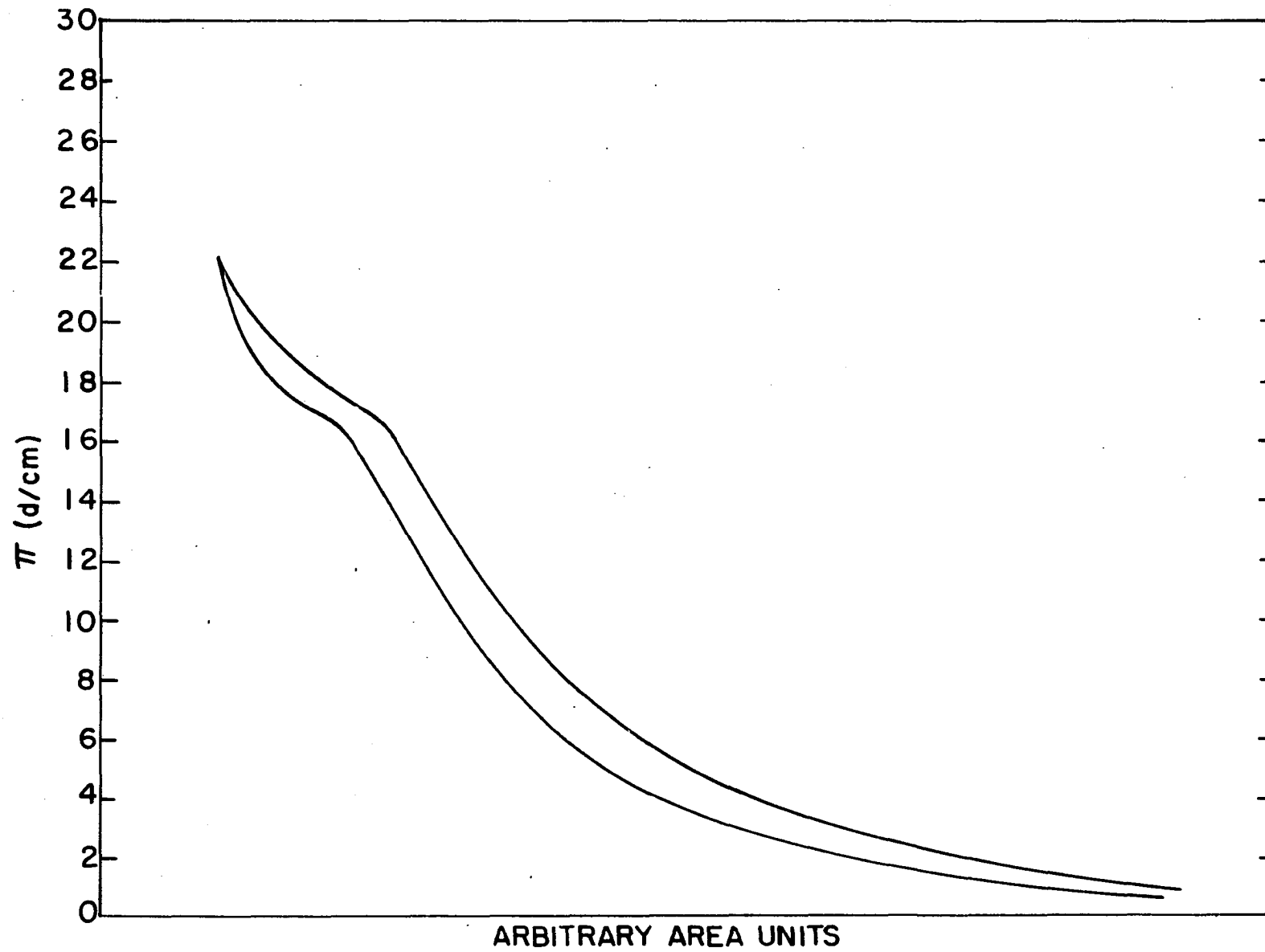


Table 9. Velocity dispersion data for propylene glycol monostearate monolayers ($t = 25.0^{\circ}\text{C}$)

$\pi = 2.0 \text{ d/cm}$		$\pi = 10.0 \text{ d/cm}$		$\pi = 16.7 \text{ d/cm}$	
$v(\frac{1}{\text{sec}})$	$c(\frac{\text{cm}}{\text{sec}})$	$v(\frac{1}{\text{sec}})$	$c(\frac{\text{cm}}{\text{sec}})$	$v(\frac{1}{\text{sec}})$	$c(\frac{\text{cm}}{\text{sec}})$
203	44.4	192	41.8	182	39.7
268	48.7	252	45.8	238	42.2
338	52.7	318	49.6	293	45.7
412	56.0	389	53.0	366	49.9
492	59.6	463	56.1	436	52.8
576	62.75	542	59.0	511	55.7
662	65.6	624	61.8	589	58.4
754	68.5	709	64.4	670	60.9
849	71.3	799	67.0	755	63.4
944	73.4	890	69.3	842	65.5
1041	75.7	983	71.5	930	67.6
1139	77.7	1076	73.2	1020	69.6
1243	79.8	1173	75.4	1109	71.3
1353	81.8	1273	77.0	1205	73.0
1466	84.2	1380	79.3	1303	74.9
-	-	1490	81.3	1408	76.8

Table 10. Damping coefficient data for propylene glycol monostearate monolayers ($t = 25.0^{\circ}\text{C}$)

$\nu(\frac{1}{\text{sec}})$	$\alpha(\frac{1}{\text{cm}})$	$\nu(\frac{1}{\text{sec}})$	$\alpha(\frac{1}{\text{cm}})$
<u>$\pi = 0.8 \text{ d/cm}$</u>		<u>$\pi = 5.0 \text{ d/cm}$</u>	
500	1.45	-	-
600	1.89	600	1.67
700	1.97	700	1.85
800	2.25	800	2.19
900	2.56	900	2.40
1000	2.78	1000	2.59
1100	3.16	1100	2.74
1200	3.34	1200	2.99
1300	3.55	1300	3.20
1400	3.71	1400	2.46
<u>$\pi = 10.0 \text{ d/cm}$</u>		<u>$\pi = 16.7 \text{ d/cm}$</u>	
500	1.59	500	1.47
600	1.69	600	1.85
700	2.01	700	2.18
800	2.22	800	2.44
900	2.48	900	2.60
1000	2.68	1000	2.96
1100	3.03	1100	3.07
1200	3.27	1200	3.17
1300	3.41	1300	3.45
1400	3.55	1400	3.71

Figure 25. Dependence of spreading pressure on area for the mixed monolayer system stearic acid and polyvinyl acetate (three hours between curves)

The curves, recorded several hours apart, have been shifted along the area axis. The spreading solvent was petroleum ether.

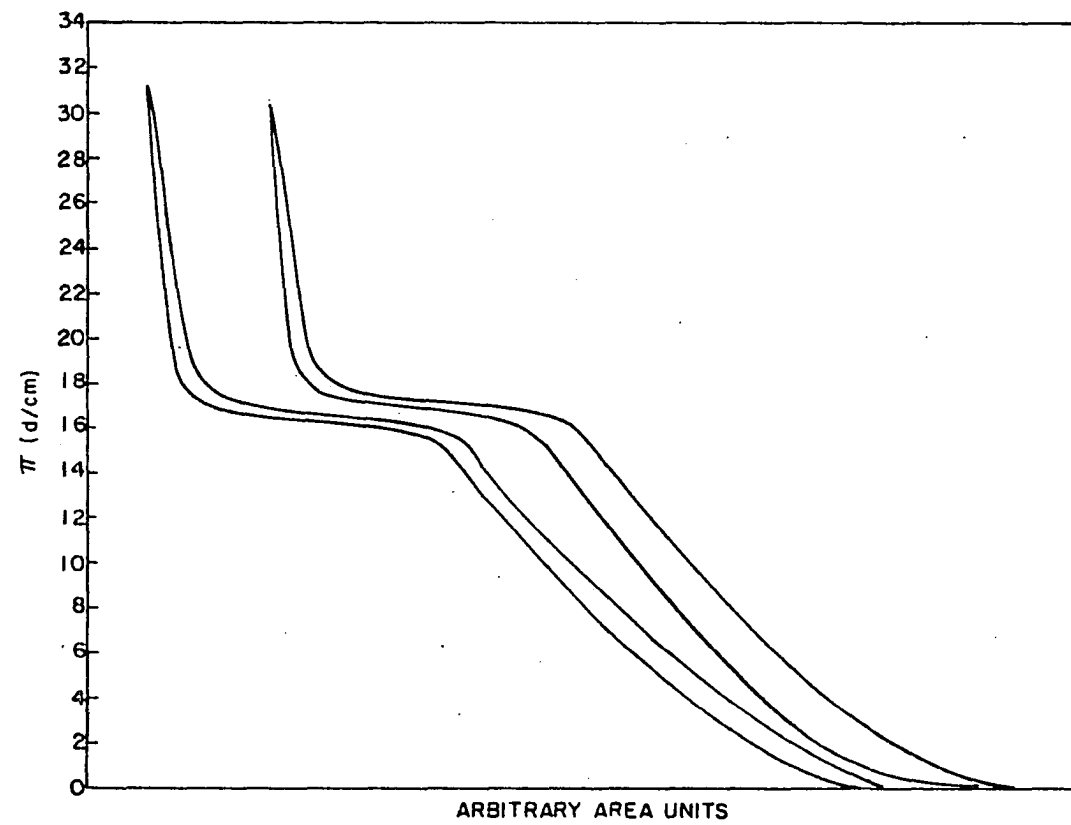


Table 11. Velocity dispersion data for stearic acid-polyvinyl acetate mixed monolayers ($t = 25.0^{\circ}\text{C}$)

$v(\frac{1}{\text{sec}})$	$c(\frac{\text{cm}}{\text{sec}})$	$v(\frac{1}{\text{sec}})$	$c(\frac{\text{cm}}{\text{sec}})$	$v(\frac{1}{\text{sec}})$	$c(\frac{\text{cm}}{\text{sec}})$
$\pi = 0.2 \text{ d/cm}$		$\pi = 10.0 \text{ d/cm}$		$\pi = 16.2 \text{ d/cm}$	
209	45.02	195	42.00	185	39.85
276	49.54	256	45.95	244	43.80
348	53.54	323	49.69	306	47.08
424	57.07	394	53.03	374	50.34
505	60.43	470	56.24	447	53.49
592	63.76	550	59.24	522	56.22
682	66.77	634	62.07	602	58.94
775	69.56	721	64.71	685	61.48
872	72.24	811	67.18	771	63.87
969	74.52	904	69.52	860	66.13
1068	76.68	997	71.58	950	68.21
1169	78.69	1092	73.50	1041	70.07
1276	80.83	1189	75.32	1133	71.78
1389	83.10	1291	77.24	1229	73.53
1502	85.13	1400	79.35	1331	75.44
-	-	1507	81.15	1437	77.38
$\pi = 16.5 \text{ d/cm}$		$\pi = 17.5 \text{ d/cm}$		$\pi = 25.0 \text{ d/cm}$	
185	39.85	240	43.08	222	39.85
243	43.62	302	46.46	280	43.08
305	46.92	370	49.80	345	46.44
373	50.21	441	52.77	411	49.18
445	53.25	516	55.57	480	51.70
521	56.11	595	58.25	553	54.14
600	58.74	677	60.76	631	56.63
683	61.30	762	63.12	709	58.73
769	63.70	851	65.44	791	60.83
857	65.90	940	67.49	876	62.90
948	68.07	1030	69.33	962	64.75
1038	69.87	1121	71.02	1046	66.26
1130	71.58	1217	72.81	1136	67.97
1227	73.41	1316	74.59	1225	69.43
1328	75.27	1421	76.52	1324	71.30
1432	77.11	1516	77.74	1421	72.87

Table 12. Damping coefficient dispersion data for stearic-acid polyvinyl acetate mixed monolayers
($t = 25.0^{\circ}\text{C}$)

$\nu(\frac{1}{\text{sec}})$	$\alpha(\frac{1}{\text{cm}})$	$\nu(\frac{1}{\text{sec}})$	$\alpha(\frac{1}{\text{cm}})$	$\nu(\frac{1}{\text{sec}})$	$\alpha(\frac{1}{\text{cm}})$
<u>$\pi = 0.4 \text{ d/cm}$</u>		<u>$\pi = 10.0 \text{ d/cm}$</u>		<u>$\pi = 16.4 \text{ d/cm}$</u>	
400	1.05	400	1.34	400	1.36
500	1.47	500	1.44	500	1.56
600	1.70	600	1.71	600	1.81
700	1.89	700	1.92	700	1.98
800	2.10	800	2.14	800	2.23
900	2.40	900	2.44	900	2.51
1000	2.51	1000	2.49	1000	2.73
1100	2.75	1100	2.88	1100	3.00
1200	2.94	1200	2.97	1200	3.10
1300	3.06	1300	3.32	1300	3.32
1400	3.51	1400	3.55	1400	3.63
<u>$\pi = 17.0 \text{ d/cm}$</u>		<u>$\pi = 17.8 \text{ d/cm}$</u>		<u>$\pi = 25.5 \text{ d/cm}$</u>	
400	1.33	400	1.38	400	1.35
500	1.56	500	1.58	500	1.61
600	1.80	600	1.77	600	2.03
700	1.98	700	2.02	700	2.35
800	2.27	800	2.27	800	2.53
900	2.51	900	2.58	900	2.74
1000	2.69	1000	2.73	1000	3.22
1100	3.03	1100	3.20	1100	3.24
1200	3.02	1200	2.99	1200	3.43
1300	3.52	1300	3.43	1300	4.14
1400	3.77	1400	3.60	1400	4.53

Table 13. Velocity dispersion data for 1,3 dipalmitoyl glyceryl phosphoric acid ($t = 25.0^{\circ}\text{C}$)

$\pi = 1 \text{ d/cm}$		$\pi = 4 \text{ d/cm}$	
$v(\frac{1}{\text{sec}})$	$c(\frac{\text{cm}}{\text{sec}})$	$v(\frac{1}{\text{sec}})$	$c(\frac{\text{cm}}{\text{sec}})$
209	45.02	203	43.72
276	49.54	268	48.11
349	53.69	337	51.85
425	57.20	412	55.45
507	60.67	489	58.51
593	63.87	574	61.82
684	66.96	659	64.52
777	69.74	750	67.31
874	72.40	843	69.83
972	74.75	937	72.06
1070	76.83	1033	74.17
1172	78.89	1131	76.13
1280	81.09	1234	78.17
1393	83.34	1342	80.29
-	-	1454	82.41

Table 14. Damping coefficient dispersion data for
1,3 dipalmitoyl glyceryl phosphoric acid,
 $\pi = 4$ d/cm ($t = 25.0^{\circ}\text{C}$)

$\nu(\frac{1}{\text{sec}})$	$\alpha(\frac{1}{\text{cm}})$
400	1.28
500	1.47
600	1.63
700	1.86
800	2.11
900	2.29
1000	2.58
1100	2.74
1200	3.09
1300	3.25
1400	3.23

Figure 26. Dependence of spreading pressure on area
for egg albumin films

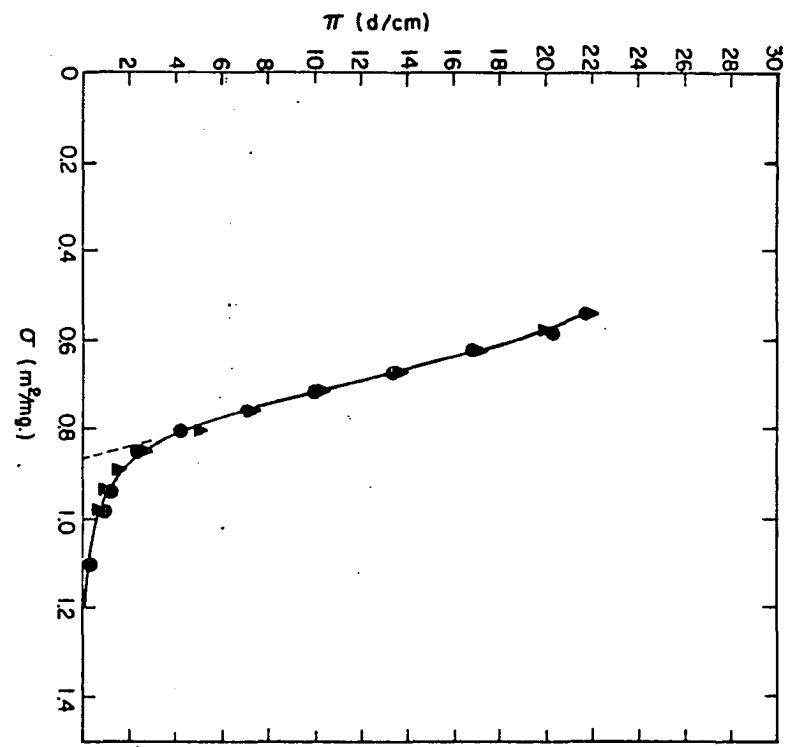


Table 15. Velocity dispersion data for egg albumin films,
 $\pi = 0.4$ d/cm ($t = 25.0^{\circ}\text{C}$)

$v(\frac{1}{\text{sec}})$	$c(\frac{\text{cm}}{\text{sec}})$
159.2	41.2
183.1	43.15
208.7	45.0
235.3	46.9
264.5	48.8
292.2	50.4
321.8	52.0
352.5	53.6
384.2	55.25
416.4	56.7
449.1	58.2
482.3	59.4
514.6	60.4
547.2	61.8
588.6	63.8
678.9	66.3
778.6	69.1
884.9	72.0
992.2	74.5
1105.8	77.1
1223.5	79.6
1345.1	82.0
1468.5	84.3

Table 16. Damping coefficient dispersion data for egg albumin films, $\pi = 0.4$ d/cm ($t = 25.0^\circ\text{C}$)

$\nu(\frac{1}{\text{sec}})$	$\alpha(\frac{1}{\text{cm}})$
300	0.85
400	1.11
500	1.29
600	1.50
700	1.67
800	1.95
900	2.03
1000	2.20
1100	2.43
1200	2.58
1300	2.69
1400	2.95

Table 17. Velocity dispersion data for heptanoic acid soluble monolayers ($t = 25.0^{\circ}\text{C}$)

$\gamma = 37.9 \text{ d/cm}$		$\gamma = 50.7 \text{ d/cm}$	
$v(\frac{1}{\text{sec}})$	$c(\frac{\text{cm}}{\text{sec}})$	$v(\frac{1}{\text{sec}})$	$c(\frac{\text{cm}}{\text{sec}})$
300.0	40.59	142.4	34.75
320.4	41.04	196.8	38.42
340.5	41.61	259.8	42.27
360.6	42.70	326.8	45.56
369.9	42.76	398.8	48.65
379.8	43.22	469.5	50.89
389.1	43.00	552.4	53.91
400.4	44.64	637.1	56.51
420.5	46.12	724.5	58.90
440.1	45.90	814.0	61.11
460.5	45.67	907.5	63.26
479.8	46.54	1001.7	65.17
500.4	47.42	1096.0	66.86
520.9	48.66	1116	67.80
540.5	48.06	1238	69.85
579.3	50.29	1384	72.88
662.3	52.71	1518	74.94
743.1	54.59	-	-
828.9	56.54	-	-
907.8	57.79	-	-
998.7	59.60	-	-
1076	60.44	-	-
1155	61.27	-	-
1268	63.73	-	-

Table 18. Damping coefficient data for heptanoic acid soluble monolayers, $\gamma = 50.7$ d/cm ($t = 25.0^\circ\text{C}$)

<u>Small probe separation</u>		<u>Large probe separation</u>	
$\nu(\frac{1}{\text{sec}})$	$\alpha(\frac{1}{\text{cm}})$	$\nu(\frac{1}{\text{sec}})$	$\alpha(\frac{1}{\text{cm}})$
100	0.365		
200	0.534	400	1.80 ^a
300	0.835	500	2.40 ^a
400	1.125	600	1.87
500	1.57	700	2.60
600	1.76	800	2.87
700	2.01	900	3.25
800	2.84	1000	3.00
900	3.09	1100	3.49
1000	3.39	1200	3.84
1100	3.68	1300	4.24
-	-	1400	4.60
-	-	1600	5.06

^aData scatter was above normal.

Table 19. Damping coefficient data for heptanoic acid soluble monolayers using the small probe separation technique, $\pi = 37.9$ d/cm ($t = 25.0^\circ\text{C}$)

$\nu(\frac{1}{\text{sec}})$	$\alpha(\frac{1}{\text{cm}})$
200	0.584
300	0.830
350	1.06
400	2.21
450	2.63
500	2.13
750	3.29
1000	3.34
1100	3.64

Table 20. Smoothed equilibrium data for heptanoic acid

c_o $\times 10^4$ (moles/liter)	γ (d/cm)	Γ_o $\times 10^{10}$ (moles/cm ²)	$\frac{1}{RT} \left(\frac{\partial \mu}{\partial r} \right) \Gamma_o$ $\times 10^{-10}$ (cm ² /mole)	$\frac{\pi}{r}$ $\times 10^{-7}$ (ergs/gm)	$-\frac{1}{A} \left(\frac{\partial A}{\partial \pi} \right)$ (cm/dyne)	$\frac{D^{1/2} c_o}{\sqrt{2RT}} \left(\frac{\partial \mu_s}{\partial r} \right) \Gamma_o$ (sec ^{-1/2})
1.0	73.0	1.0	0.61	-	-	1.30
2.0	72.0	2.0	0.75	-	-	3.17
4.0	70.0	2.9	0.85	-	-	7.22
6.0	68.0	3.4	0.95	-	-	12.1
10	64.5	3.8	1.05	18.2	0.0392	22.2
20	58.7	4.2	1.6	26.2	0.0171	67.8
40	51.5	4.6	2.7	36.2	0.00840	229
60	47.5	4.7	3.8	41.8	0.00574	483
80	44.2	4.8	5.0	-	0.00454	848
100	41.5	4.8	6.3	-	0.00400	1335
125	38.8	4.9	7.9	-	0.00340	2100
136	37.9	4.9	8.6	-	0.00312	2480

DISCUSSION

Before exploring the comparison of ripple propagation theory to experimental results, it is pertinent to consider first several results derived from limiting forms of the relations expressed in Equations 73 and 74 for the insoluble monolayer case and Equations 111 and 112 for the soluble monolayer case. We shall then present data reported in the last section now plotted as the dimensionless quantities Z_1 and Z_6 for comparison with theoretically derived curves. Implications of these comparisons will be discussed, and suggestions for future work will close This Thesis.

Theory

The reduction of Equations 73, 74 and Equations 111, 112 to sets of numbers suitable for comparison of the theory to experimental results was a most intriguing part of this study. The information sought was enmeshed in both the real and imaginary parts of the complex determinants of the coefficients of these equations in a surprisingly subtle manner.

For concreteness, let us first limit the discussion to the insoluble monolayer case; the soluble monolayer case is really of the same cast since only the role of the elastic constant is modified by a diffusion flux term. We shall

point later comments to this character. .

What characters will determine the propagation parameters of the systems studied? Bulk properties are given by parameters expressing fluid viscosity (μ), density (ρ) and body forces, usually gravity, while surface properties of the system are given by surface tension (γ), surface elastic (k_e) and surface viscosity (k_v) parameters which are, in principle, known. Suppose we take frequency (ν) to be the independent variable; then at a given frequency three propagation parameters, the wave length (λ), speed (c) and the damping coefficient (α) must be fixed. These dependent variables are unique; however, the inverse of the transformation, taking α and λ or c into ν , is not in general unique. If gravity is taken into account, as in Equation 23 (theory), then the velocity dispersion contains a minimum; gravity controlled waves travel faster as the frequency decreases but surface tension controlled waves travel faster as the frequency increases. We have developed only the equations for the higher frequency region where gravity effects can be neglected.

Since we have three propagation parameters to consider, i.e., c , λ , and α , we need three equations to determine these dependent variables in terms of the surface and bulk parameters and frequency:

$$F_r(\alpha, c, \lambda, \rho, g, \mu, \gamma, k_e, k_v, \nu) = 0 \quad (\text{Eq. 1})$$

$$F_i(\alpha, c, \lambda, \rho, g, \mu, \gamma, k_e, k_v, \nu) = 0 \quad (\text{Eq. 2})$$

$$c - \nu\lambda = 0 \quad (\text{Eq. 3})$$

Equations 1 and 2 are the real and imaginary parts of the complex determinant of the coefficients of Equations 73 and 74 of the theory section.

These equations were easily reduced to dimensionless form using the definitions expressed in Equations 79. In this new form, we again have three equations to consider:

$$f_r(Z_1, Z_2, Z_3, Z_4, Z_5, Z_6) = 0 \quad (\text{Eq. 4})$$

$$f_i(Z_1, Z_2, Z_3, Z_4, Z_5, Z_6) = 0 \quad (\text{Eq. 5})$$

and

$$Z_6 - 2Z_5^2 Z_4 = 0 \quad (\text{Eq. 6})$$

Again, three of the groups can be expressed in terms of the other three. However, the physical interpretation given these groups is now somewhat more subtle. The role of Z_1 is clear if we note that $2\pi Z_1$ is just the damping per wave

length. Z_2 and Z_3 clearly reflect the surface visco-elastic constants. Z_6 also appears unambiguous since this parameter must represent the departure of the system from ideal liquid behavior; $Z_6 = 1$ is precisely the Kelvin equation. We note that Z_4 contains the propagation velocity as the only frequency dependent factor. However Z_4 , Z_5 and Z_6 mix the bulk, surface and propagation parameters. The calculation of α involves only Z_1 ; however, the calculation of c or λ involves pairs of the three groups Z_4 , Z_5 and Z_6 . It should be clear from the discussion in the previous section that we calculated Z_1 and Z_6 using the first approximation to what would be an iterative procedure, i.e., the Kelvin equation, $Z_6 = 1$, was used to give k as a function of v for the calculation of $Z_{4,1}$ and $Z_{5,1}$ which, in turn, allowed us to solve Equations 4 and 5 for $Z_{1,1}$ and $Z_{6,1}$ using Z_2 and Z_3 as adjustable parameters.

If we take the real and imaginary parts of the determinant, Equation 85 (theory), and solve for Z_1 we find two quadratic equations as follows:

the real part

$$AZ_1^2 + BZ_1 + Z_3 - 4Z_4^2 + 4Z_4^2Z_5 + [Z_6 - Z_5(Z_2 - Z_3)][Z_6 - 1] = 0$$

(Eq. 7)

and the imaginary part

$$\bar{A}Z_1^2 + \bar{B}Z_1 + 4Z_4(Z_6 - Z_4Z_5) - Z_2 - Z_5(Z_2 + Z_3)(Z_6 - 1) = 0 \quad (\text{Eq. 8})$$

where A, B, \bar{A} and \bar{B} are polynomials in Z_2, Z_3, \dots, Z_6 .

At this point, one finds that Z_6 enters the formulation in a rather subtle fashion. Z_6 , experimentally, is close to 1 (0.90 to 1.0) so that to a fair approximation

$$Z_6 \approx 1 \quad .$$

However, we know experimentally that $1 - Z_6$ is of the same order of magnitude as Z_1 and we see from Equations 7 and 8 that $Z_6 - 1$ multiplies terms containing Z_2 and Z_3 . These two facts suggest that we must not exclude $Z_6 - 1$ by assuming that the Kelvin equation holds exactly.

Solving the imaginary part for $Z_6 - 1$ and substituting this result into the real part yields

$$\left[A + \frac{[Z_6 - Z_5(Z_2 - Z_3)]\bar{A}}{Z_5(Z_2 + Z_3)} \right] Z_1^2 + \left[B + \frac{[Z_6 - Z_5(Z_2 - Z_3)]\bar{B}}{Z_5(Z_2 + Z_3)} \right] Z_1$$

$$+ [z_3 - 4z_4^2 + 4z_4^2 z_5] + \frac{[z_6 - z_5(z_2 - z_3)][4z_4(z_6 - z_4 z_5) - z_2]}{z_5(z_2 + z_3)} = 0 \quad (\text{Eq. 9})$$

If we multiply Equation 9 by $z_5(z_2 + z_3)$ in order to find the limiting form corresponding to $k_e = k_v = 0$, the conditions for a clean water surface, we see that, in this case, the terms remaining are associated only with the imaginary part of the determinant. If we ignore all terms of second and higher order of smallness, we find

$$z_1 = \frac{4}{3}z_4 \quad (\text{Eq. 10})$$

The damping of capillary ripples on monolayer free water surfaces should follow this relation and, indeed, this was found experimentally as we shall display later.

Suppose we now assume that z_1 is very small and in fact can be taken as zero. Further, suppose that the fluid is monolayer free and that the bulk viscosity, the film viscosity and film elasticity constants can be taken as zero. These assumptions imply that $z_1 = z_2 = z_3 = z_4 z_5 = z_4 = 0$ so that Equations 81 and 82 (theory) become

$$i(Z_6 - 1)Q - G = 0$$

$$iZ_6G = 0 .$$

Since $Z_6 \neq 0$ we see that $G = 0$; for a non-trivial solution ($Q \neq 0$) we have

$$Z_6 = 1 \quad (\text{Eq. 11})$$

which states that the velocity dispersion for this limiting case is given by

$$\frac{\rho}{\gamma} \frac{\omega^2}{k^3} = 1$$

or

$$c = \sqrt[3]{\frac{\gamma}{\rho} \omega} .$$

This is precisely the Kelvin equation derived under the ideal fluid assumptions discussed early in the theory section.

Suppose we allow $(Z_2 + Z_3)$ to become very large, i.e., the elastic constant of the film is taken to be arbitrarily large. Referring to Equation 70 of the theory section we see that

$$\underline{kQ} - imG = 0 \quad (\text{Eq. 12})$$

which implies, according to Equation 55 (theory) that $\xi = 0$, i.e., the lateral monolayer displacement is zero. If we ignore second order and higher terms Equation 9 becomes

$$-1 + 3Z_1 Z_5 + Z_1 (3Z_5 - 4) = 0$$

so that

$$Z_1 = \frac{1}{6Z_5 - 4}$$

should approximate the rigid monolayer case.

The results for intermediate values of the viscoelastic parameters k_e and k_v are presented in Figures 27, 28 and 29. The Z_1 dispersion curves were calculated from Equation 9; the Z_6 dispersion was calculated using an analogous equation derived by eliminating Z_1 from the real and imaginary parts of Equation 85 (theory). Several features of these curves are listed below:

- i) The effect of a change in k_e on Z_1 and Z_6 is small for

$$k_e > 10^3 \text{ d/cm}$$

and

$$k_e < 10^{-1} \text{ d/cm} .$$

- ii) At constant k_v and ν , Z_1 goes through a shallow minimum for

$$10^{-1} \text{ d/cm} < k_e < 10 \text{ d/cm} .$$

- iii) The effect of k_v on Z_1 is small for

$$k_v < 10^{-6} \frac{\text{d} - \text{sec}}{\text{cm}}$$

and

$$k_v > 10 \frac{\text{d} - \text{sec}}{\text{cm}} .$$

- iv) At constant k_e and ν , Z_1 goes through a minimum for

$$10^{-2} \frac{\text{d} - \text{sec}}{\text{cm}} < k_v < 1 \frac{\text{d} - \text{sec}}{\text{cm}} .$$

- v) At constant k_v and ν , Z_6 goes through a minimum for

$$10^{-1} \text{ d/cm} < k_e < 100 \text{ d/cm} .$$

Figure 27. The theoretical dependence of Z_1 on frequency

$$\begin{aligned}\pi & - \text{varies} \\ k_e & = 10^4 \\ k_v & = 10^{-8} \frac{\text{d} - \text{sec}}{\text{cm}}\end{aligned}$$

$$\begin{aligned}\pi & = 0.0 \text{ d/cm} \\ k_e & - \text{varies} \\ k_v & = 10^{-8} \frac{\text{d} - \text{sec}}{\text{cm}}\end{aligned}$$

$$\begin{aligned}\pi & = 0.0 \text{ d/cm} \\ k_e & = 1 \text{ d/cm} \\ k_v & - \text{varies}\end{aligned}$$

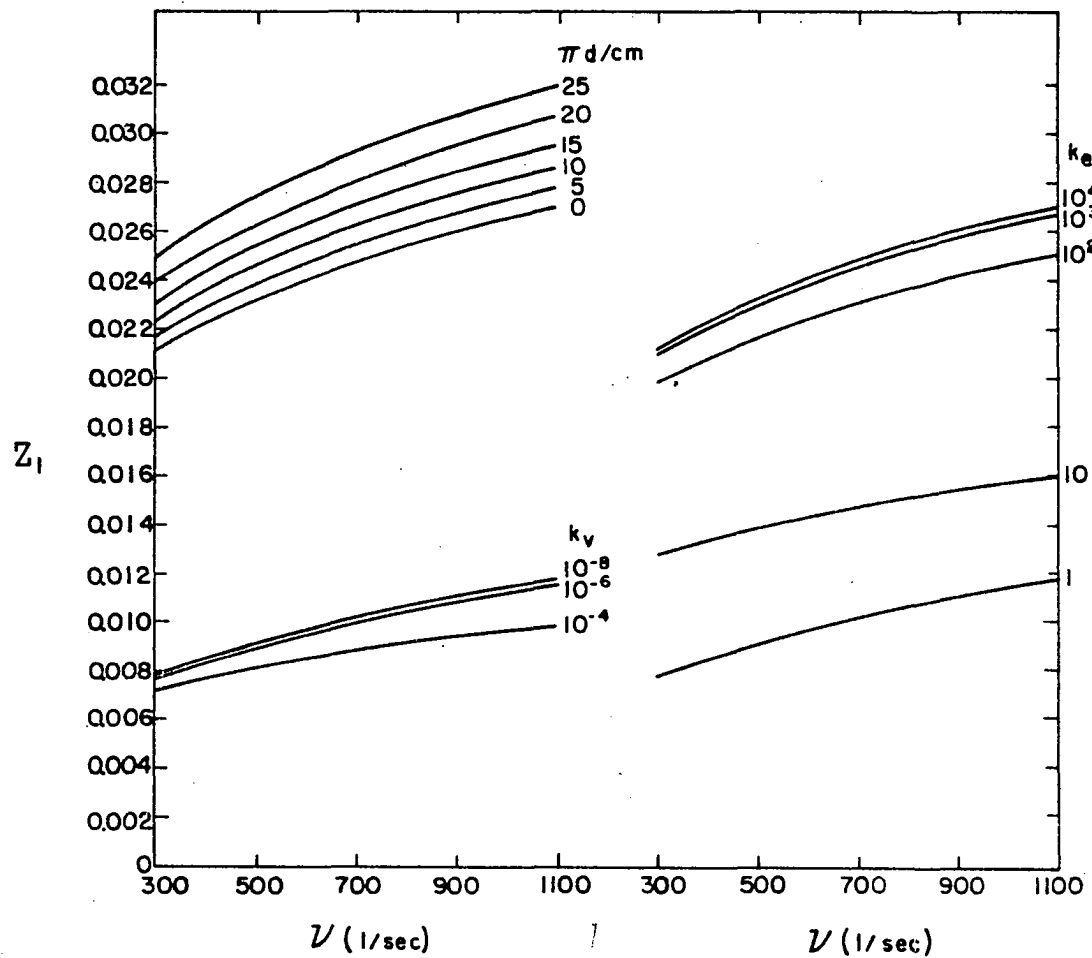


Figure 28. Theoretical dependence of Z_1 on k_e and k_v at 300 cps

$$\pi = 0.0 \text{ d/cm}$$

$$k_e = 1 \text{ and } 10 \text{ d/cm}$$

$$k_v - \text{varies}$$

$$\nu = 300 \text{ cps}$$

$$\pi = 0.0 \text{ d/cm}$$

$$k_v = 10^{-8} \frac{\text{d} - \text{sec}}{\text{cm}}$$

$$k_e - \text{varies}$$

$$\nu = 300 \text{ cps}$$

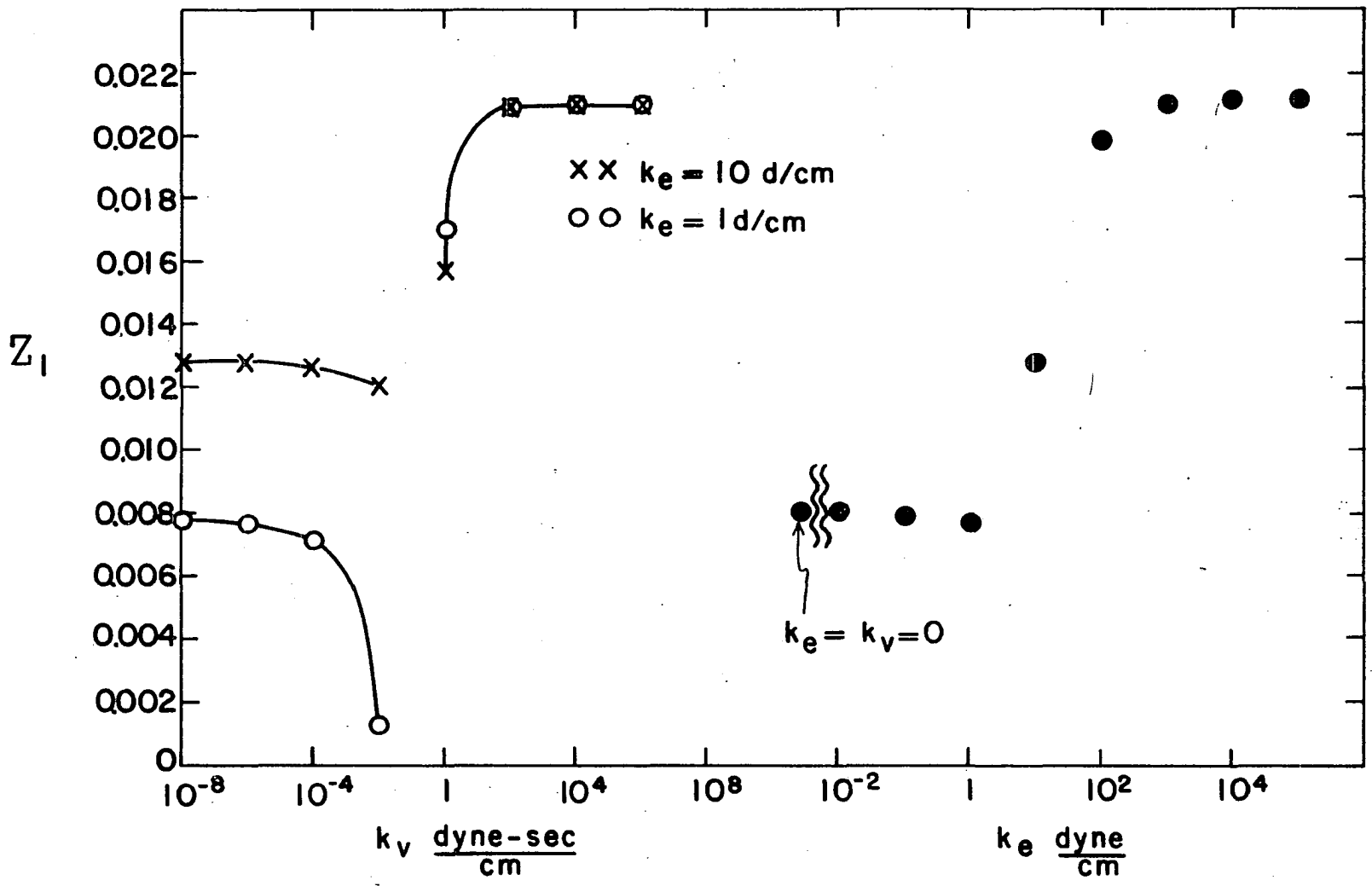
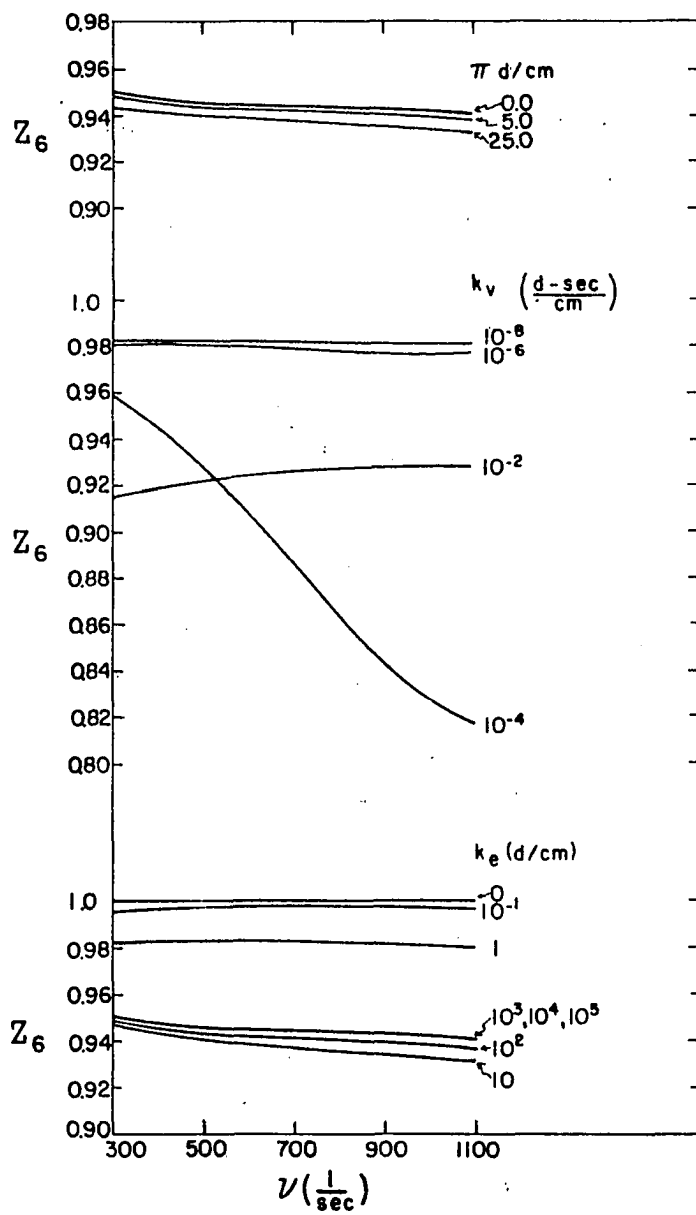


Figure 29. Theoretical dependence of Z_6 on frequency

$$\begin{aligned}\pi & - \text{varies} \\ k_e & = 10^6 \text{ d/cm} \\ k_v & = 10^{-8} \frac{\text{d} - \text{sec}}{\text{cm}}\end{aligned}$$

$$\begin{aligned}\pi & = 0.0 \text{ d/cm} \\ k_e & = 1 \text{ d/cm} \\ k_v & - \text{varies}\end{aligned}$$

$$\begin{aligned}\pi & = 0.0 \text{ d/cm} \\ k_e & - \text{varies} \\ k_v & = 10^{-8} \frac{\text{d} - \text{sec}}{\text{cm}}\end{aligned}$$



vi) At constant k_v , Z_6 is insensitive to k_e changes for

$$k_e > 10^2 \text{ d/cm}$$

and

$$k_e < 10^{-1} \text{ d/cm} .$$

vii) At constant k_e , Z_6 is insensitive to k_v changes for

$$k_v < 10^{-6} \frac{\text{d} - \text{sec}}{\text{cm}} .$$

viii) At $k_e = 1$, the Z_6 dispersion curve for $k_v = 10^{-4} \frac{\text{d} - \text{sec}}{\text{cm}}$ crosses that for $k_v = 10^{-2} \frac{\text{d} - \text{sec}}{\text{cm}}$.

ix) For $k_e > 10^2$ and $k_v < 10^{-6}$, Z_6 is rather insensitive to changes in surface pressures.

The dependence of Z_1 and Z_6 on k_e orders as one should intuitively expect since the lateral forces involved with local changes in surfactant density increase with k_e . It is interesting to note that for large values of k_e , i.e., for solid films, Z_6 dispersion is nearly independent of spreading pressure. As we shall show later, this property was one of our experimental results.

The dependence of Z_1 and Z_6 on k_v with $k_e < 100$ is surprising. With $k_e = 1$ d/cm and $\nu > 300$ cps, Z_1 becomes negative for $10^{-2} \frac{\text{d} - \text{sec}}{\text{cm}} \leq k_v < 1 \frac{\text{d} - \text{sec}}{\text{cm}}$. This region of the solution surface probably reflects resonance conditions for ripple propagation. Negative Z_1 values imply that waves would grow rather than damp with distance from the source. Emmons et al. (20), in a paper on Taylor instability of finite surface waves, described a set of conditions under which wave growth would occur. However, the body forces involved in their considerations were not simple gravity forces. While Z_1 may become small for certain combinations of ν , k_e , and k_v (resonance), we doubt that wave growth could occur under normal gravity conditions. However, three possibilities occur to us:

- i) The theoretical equations, based on a first order perturbation treatment, are not valid in this region of the solution surface.
- ii) The iteration procedure used to calculate Z_1 and Z_6 does not converge quickly enough (or at all) in this region to justify using only the first member of the sequence.
- iii) There are conditions under which ripples may grow in a normal gravity field.

This aspect of the theory will be left for future study.

We must hasten to point out that k_v is not the shear surface viscosity parameter calculated from bob damping or channel flow experiments but rather it is associated with the relaxation of compression stress on the monolayer. Unfortunately, stress relaxation in monolayer systems has not been studied extensively so that it is difficult to place bounds on k_v consistent with experiments independent of our own work. Since we should expect k_v to play an important role in frequency regions corresponding to time constants for stress relaxation, we wish to list frequency regions of possible interest.

- i) Relaxation due to hydrogen bonding or hydrocarbon chain interaction in fatty acid and alcohol monolayers should occur in frequency regions well above 10^6 cps. These regions are far out of our working range.
- ii) Stress relaxation of monolayers with time constants larger than 0.1 second has been noted in our film balance work. The force-area curve hysteresis loop, e.g., Figure 22, is an example of this effect. Harkins (2) also reports time effects.

Since we are far removed from these two regions, we should expect k_v to be small in simple monolayer systems such as stearic acid spread on water. However, this parameter

could gain importance in polymer films. Results on several polymer systems will be discussed later.

The soluble monolayer case is distinguished only by inclusion of a diffusion flux into the boundary value problem. This complication modifies the elastic constant somewhat for if we assume $k_v = 0$, then Equations 73 and 111 (theory) read

$$\left\{ \left[\frac{ik_e}{\omega} \right] ik^3 - 2i \underline{k}^2 \right\} Q + \left\{ \left[\frac{ik_e}{\omega} \right] mk^2 - \mu(\underline{k}^2 + m^2) \right\} G = 0$$

(Eq. 14)

and

$$\left\{ \left[\frac{\frac{ik_e}{\omega}}{1 + i \frac{C_o D}{RT\omega} \left(\frac{\partial \mu_s}{\partial r} \right) r_o \left(\underline{k}^2 - i \frac{\omega}{D} \right)^{\frac{1}{2}}} \right] ik^3 - 2i \mu \underline{k}^2 \right\} Q$$

$$+ \left\{ \left[\frac{\frac{ik_e}{\omega}}{1 + i \frac{C_o D}{RT\omega} \left(\frac{\partial \mu_s}{\partial r} \right) r_o \left(\underline{k}^2 - i \frac{\omega}{D} \right)^{\frac{1}{2}}} \right] mk^2 - \mu(\underline{k}^2 + m^2) \right\} G = 0$$

(Eq. 15)

Obviously $\frac{ik_e}{\omega}$ goes into

$$\frac{\frac{ik_e}{\omega}}{1 + i \frac{C_0 D}{RT\omega} \left(\frac{\partial \mu_s}{\partial r} \right) r_0 (k^2 - i \frac{\omega}{D})^{\frac{1}{2}}}$$

if a diffusion controlled mechanism is assumed for adsorption from solution. At high frequencies, soluble monolayers will behave as though they were insoluble. Since C_0 and D must become very small as solubility decreases, the insoluble monolayer equations could also be thought of as a limiting form of the soluble monolayer equations.

Experimental

Monolayer free water

The first crucial test of the theory was to predict the wave damping and velocity dispersion actually observed in our experiments with monolayer free water surfaces. We worked under a small handicap since even though the Kelvin equation has been verified previously, to our knowledge, only two quantitative damping coefficients for capillary ripples on water have been reported in the literature.¹

¹Brown (9) gave $\alpha = 0.191 \frac{1}{\text{cm}}$ for "straight" ripples and $\alpha = 0.212 \left(\frac{1}{\text{cm}} \right)$ for "circular" ripples, both for a frequency of 300 cps.

Obviously, comparison of our damping coefficient data with published experimental results was not possible.

The velocity dispersion data, in terms of Z_6 , are shown in Figure 30a. Recall that

$$Z_6 = \frac{\rho}{\gamma} \frac{\omega^2}{k^3}$$

so that the maximum differential % error is

$$\begin{aligned} \frac{\delta Z_6}{Z_6} \times 100 &= \left[\frac{\delta \rho}{\rho} + \frac{\delta \gamma}{\gamma} + \frac{2\delta \omega}{\omega} + \frac{3\delta k}{k} \right] 100 \\ &= \left[\frac{\delta \rho}{\rho} + \frac{\delta \gamma}{\gamma} + \frac{3\delta c}{c} + \frac{\delta \omega}{\omega} \right] 100 . \end{aligned}$$

Assigning conservative error levels, we have

$$\% \text{ error in } Z_6 \approx [0.1 + 1.0 + 3.0 + 0.1]$$

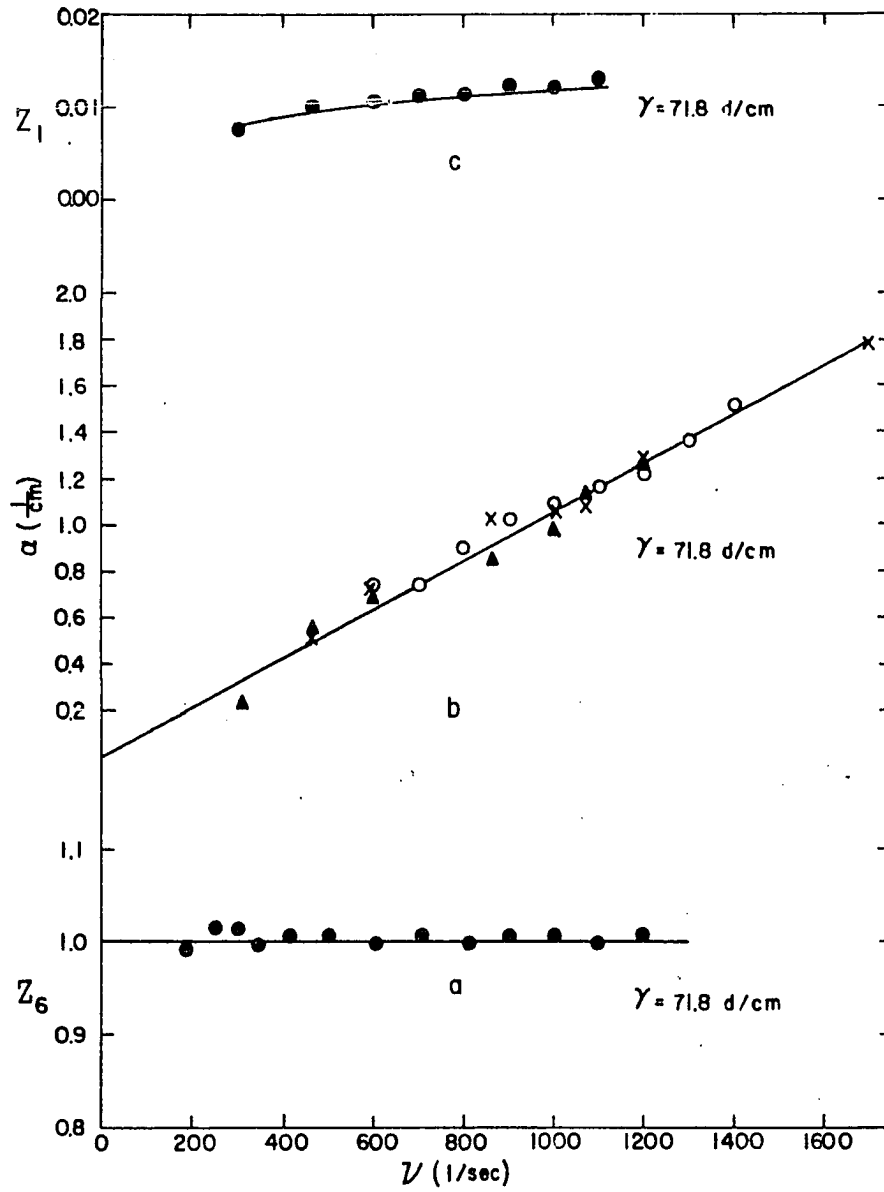
$$\approx 4 .$$

The water velocity data fit the theoretically predicted curve well within this error level and in fact, the maximum deviation from the theoretical level is 1.5% while the average deviation is below $\frac{1}{2}\%$. Obviously, ideal fluid

Figure 30. Dependence of wave velocity and damping on frequency for monolayer free water

Curves are theoretical, points are experimental

- a. Z_6 dispersion
- b. Damping coefficient dispersion
- c. Z_1 dispersion



behavior is followed rather closely in this system.

The damping coefficient data are presented in Figure 30b,c. In the damping coefficient (α) dispersion plot, three sets of data are represented:

- i) The probes were separated several centimeters so that output voltage vs. probe separation plots were linear. Two data sets are shown that had been taken several months apart. Our results were reproducible at frequencies above 300 cps to 10% or better.
- ii) The third set of data was taken using the oscillating output voltage vs. probe separation plots resulting from the vary L technique applied to small (1 cm or less) probe separations, e.g., Figure 16 (experimental section). Except for the 300 cps point, the data are within 10% of the theoretically predicted curve.

In the damping coefficient plot, Figure 30b, the theoretical curve was graphed from the first order limiting form of the theory written as

$$\alpha = \frac{4}{3} \frac{\mu}{\gamma} \omega .$$

The curve in Figure 30 designated by c shows the data fit using the dimensionless group Z_1 calculated from

Equation 9 with $Z_2 = Z_3 = 0$. The fit appears to be within experimental error; however, there is perhaps a small tendency to underestimate the experimental values. Even so, we considered the theory-experiment comparison to be quite satisfactory for the monolayer free water system.

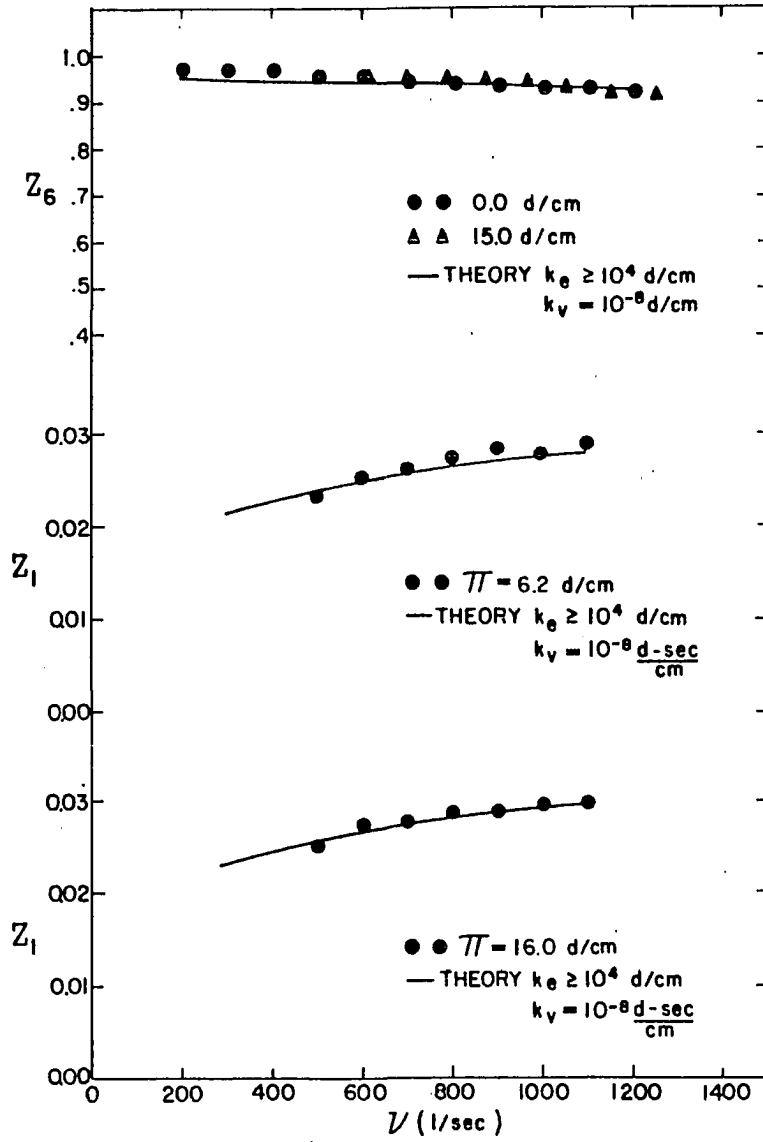
Stearic acid

Stearic acid monolayers have been extensively studied since the invention of the film balance during the early years of this century. Compression properties are well documented. It is pertinent to realize that stearic acid forms condensed monolayers at all spreading pressure; the compressibility ranges from $10^{-2} \frac{\text{cm}}{\text{d}}$ to roughly $10^{-3} \frac{\text{cm}}{\text{d}}$ depending upon the spreading pressure.

Since k_e should correlate with the inverse of the compressibility, we should expect that these monolayers will behave as rigid films to capillary ripple motion. As Figure 31 shows, this speculation closely correlates the theoretical and experimental results. The fit at either spreading pressure is within experimental error; however, the calculated Z_1 curves do seem to slightly underestimate the experimental points. The approximations carried in the calculation could account for this discrepancy.

We notice that, as predicted by theory, the parameter Z_6 is less than 1 at all frequencies and that it is

Figure 31. Dependence of Z_6 and Z_1 on frequency for stearic acid monolayers at various spreading pressures



essentially independent of spreading pressure.

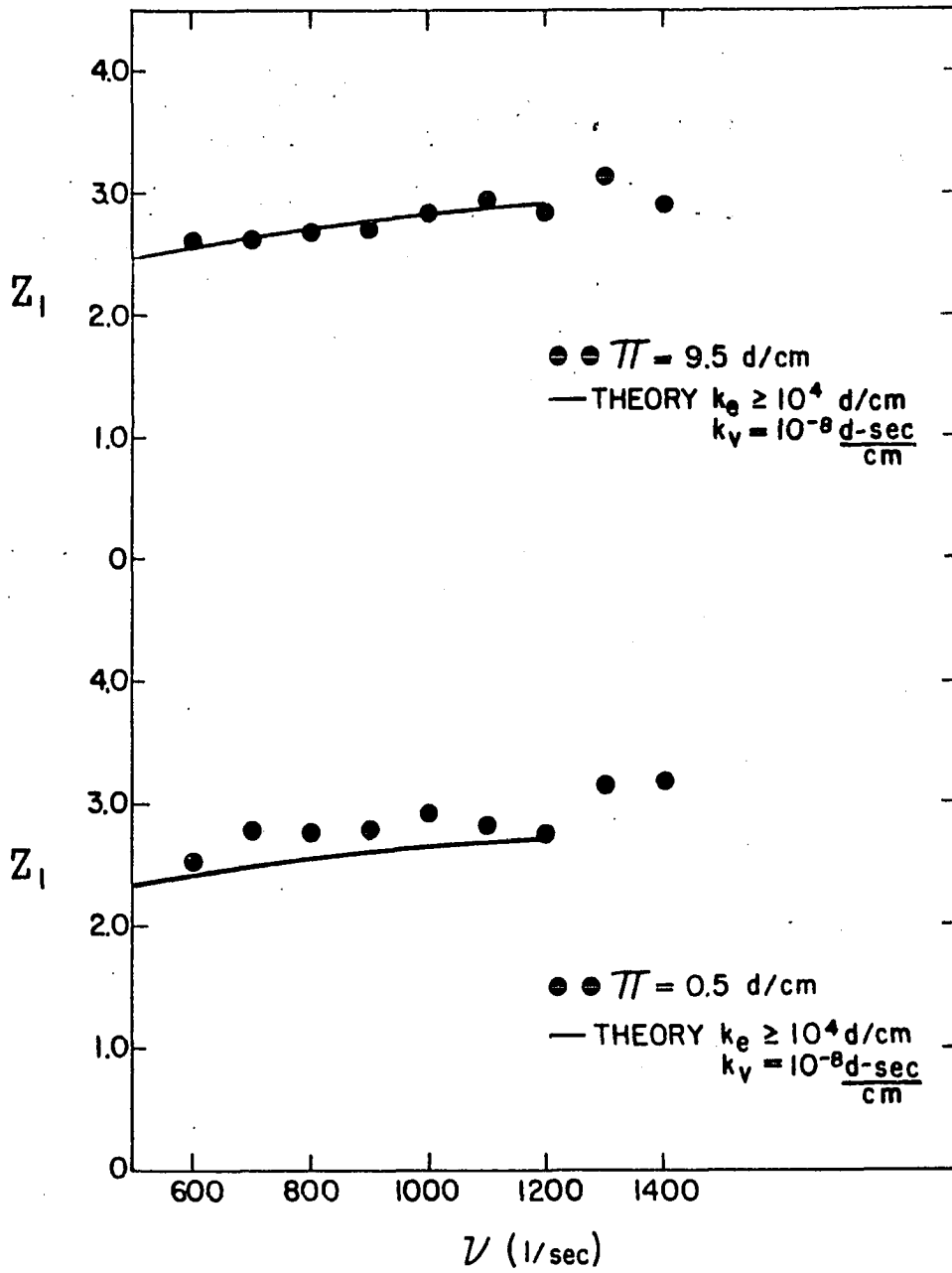
Mixed alcohol system

The mixed alcohol system, hexadecanol and octadecanol, provides a feature not accessible in most simple monolayer systems at room temperature; a two dimension phase change occurs as witnessed by the force area curve, Figure 23. Damping coefficient dispersion, Figure 32, was determined at only two spreading pressures while velocity dispersion was recorded for four spreading pressures including the pressure at which the phase change occurred. Although the 0.5 d/cm damping coefficient data were slightly underestimated by the theory, the correlation between theory and the experimental data was good enough to conclude that, in the frequency region explored, dispersion anomalies did not occur during phase changes.

Stearic acid - polyvinyl acetate

This mixed monolayer system presented another possibility for stress relaxation analysis. The force-area curves for this system have been recently discussed by Ries and Walker (40). It appears that at low spreading pressures stearic acid molecules and polymer molecules share the free surface; however, at high spreading pressures the polyvinyl acetate chains are squeezed out of the monolayer into a substrate layer just below the rigid stearic acid film.

Figure 32. Dependence of Z_1 on frequency for the mixed monolayer system octadecanol and hexadecanol



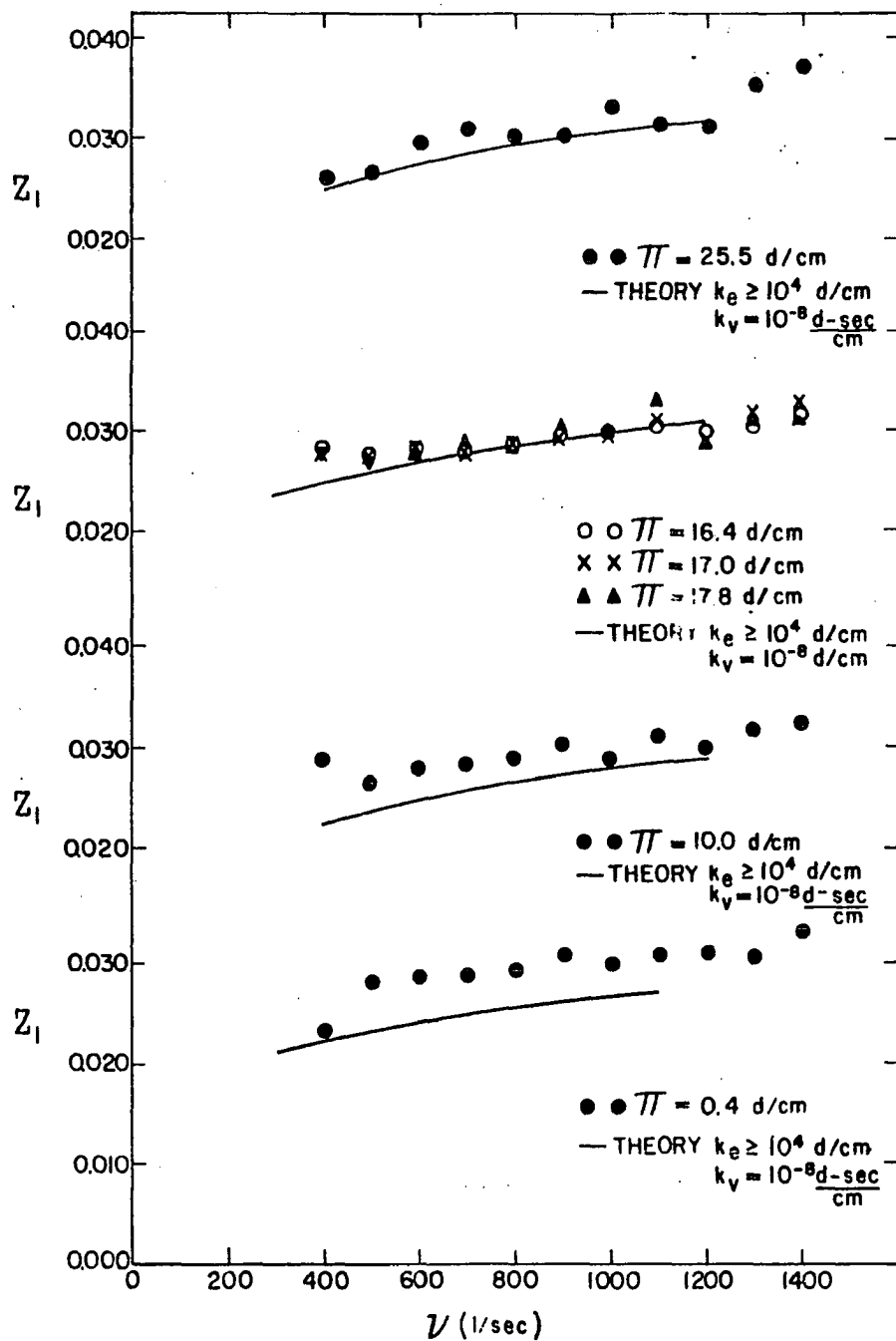
It is interesting to note in Figure 33 that the theoretical Z_1 curves fit the high spreading pressure data rather closely while the low spreading pressure data are underestimated by roughly 15%. This feature appears to correlate with the observation of Ries and Walker that under high surface pressure conditions, the mixed monolayer was composed principally of stearic acid molecules. It would be pertinent to explore much more extensively the dispersion properties of ripples traveling on this type of mixed monolayer system; dispersion occurring at low spreading pressures should be especially interesting.

Egg albumin

We chose the protein egg albumin as a representative of the class of naturally occurring polymers that form spread films. Even though a number of workers have explored this system using conventional film balance techniques, the published results are rather diverse. For us, however, the interesting fact was that even though egg albumin is rather water soluble, as compared to stearic acid, it can be spread as a very thin film¹ and further, it has compression properties similar to conventional insoluble monolayers. Extensive chain interaction could possibly affect the ripple

¹The term "monolayer" does not precisely describe these spread polymer films.

Figure 33. Dependence of Z_1 on frequency for the mixed monolayer system stearic acid and polyvinyl acetate at various spreading pressure



dispersion properties.

We mentioned in the experimental section that a gain in sensitivity was realized by a slight modification of the receiving probe. Figure 34 represents the result of that modification. Sufficiently large probe separations could be used so that very detailed velocity dispersion data could be collected by the constant probe separation and vary frequency technique. Comparison of the Δv^1 vs. $v_{\frac{n}{2}}$ plots for water and egg albumin films shows that even this rather complicated system reacts simply to ripple propagation. The structure in various regions, e.g., 500 to 550 cps, is probably due to mechanical coupling rather than film relaxation. It appears, however, that the instrumentation now has sufficient resolution and sensitivity to allow detection of small anomalous velocity dispersion effects in the range of 100 cps to approximately 1500 cps.

The Z_1 dispersion data, Figure 35a, was matched quite well by our theory. There was no indication of stress relaxation in the frequency range available to us.

$${}^1\Delta v = v_{\frac{n+1}{2}} - v_{\frac{n}{2}} \text{ for } n = j, j+1, j+2, \dots, j+m$$

where j is the half integer number of waves residing between the probes at the lowest frequency recorded and $j+m$ is the half integer number of waves between the probes at the highest frequency recorded.

Figure 34. Dependence of constant L frequency differences on frequency for monolayer free water and egg albumin films

Distilled water data, $\gamma = 71.8$ d/cm, plotted as recorded (probe separation was 2.88 cm)

Egg albumin, $\pi = 0.3$ d/cm, subtract 8 cps to reconstruct original data set (probe separation was 2.46 cm)

Egg albumin, $\pi = 9.9$ d/cm, subtract 15 cps to reconstruct original data set (probe separation was 2.46 cm)

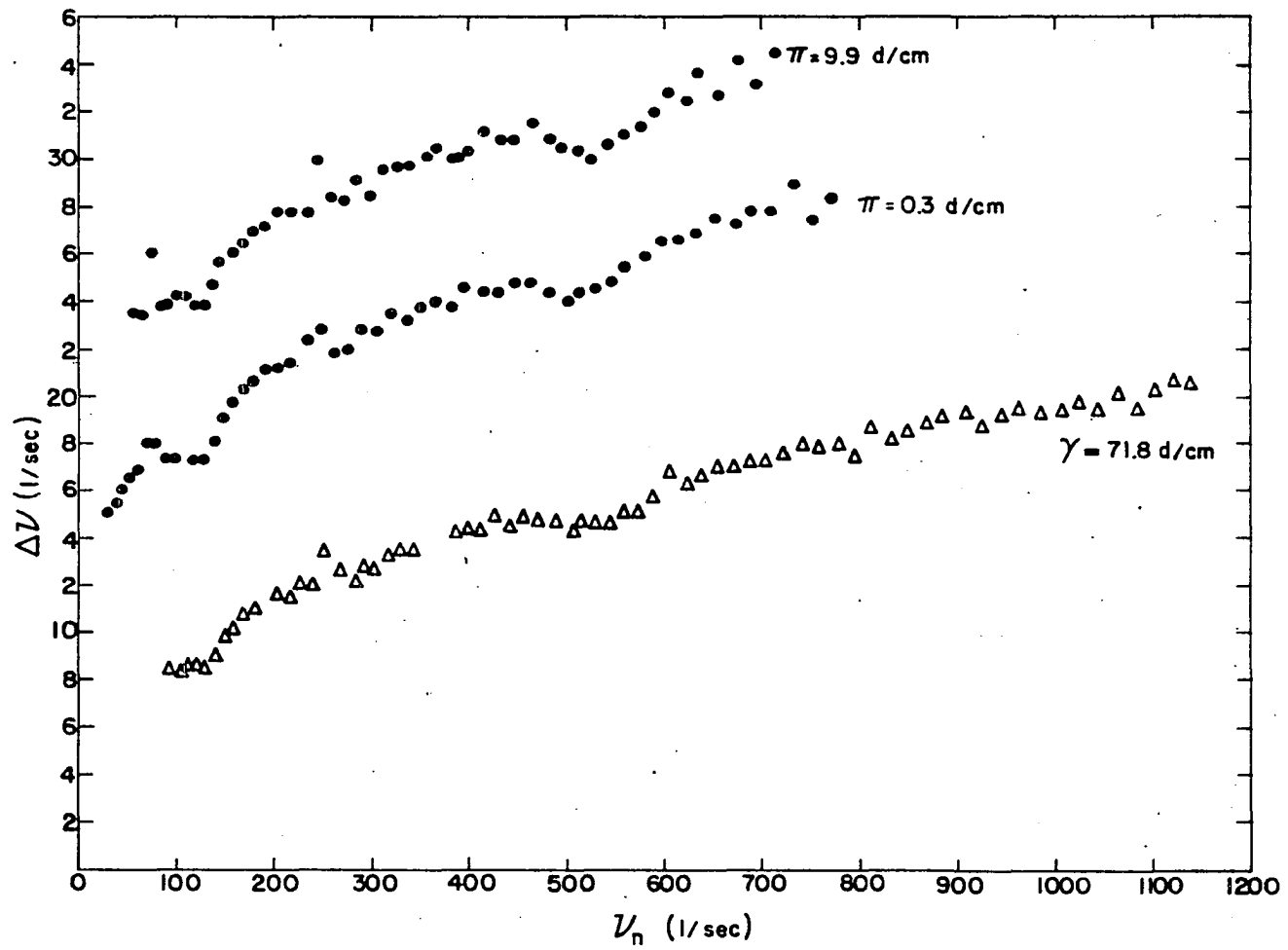


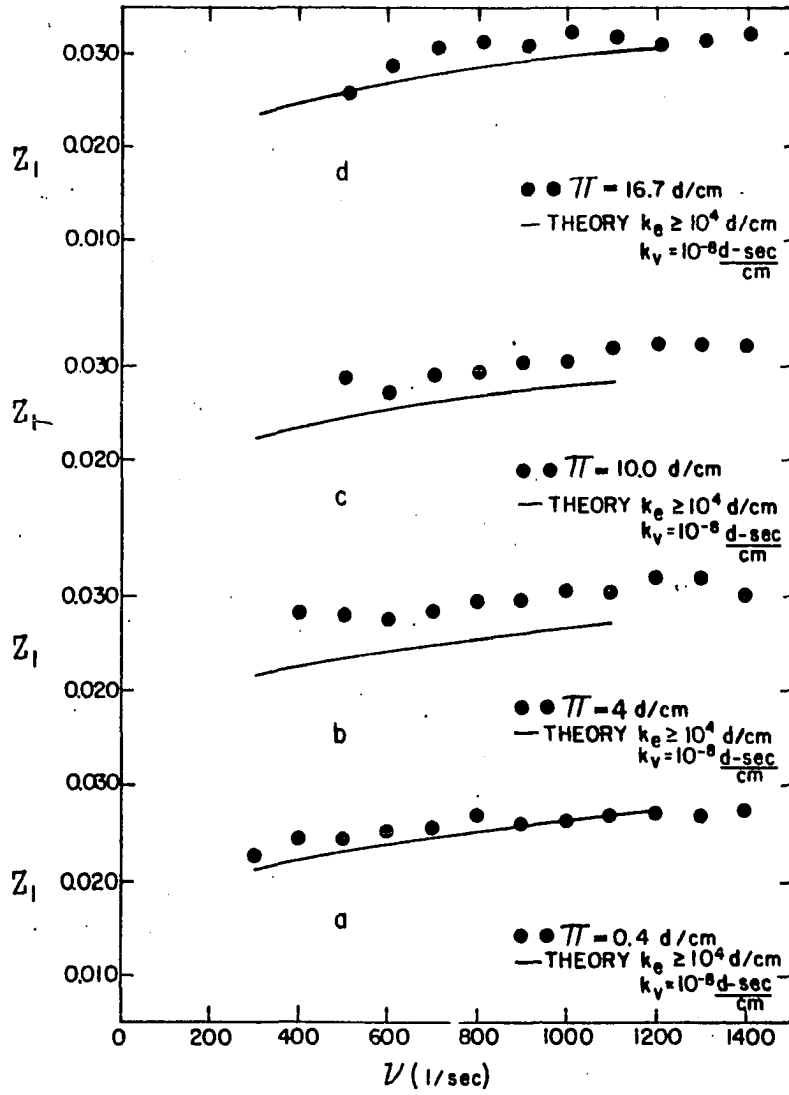
Figure 35. Dependence of Z_1 on frequency for several systems

d. Propylene glycol monostearate
 $\pi = 16.7$ d/cm

c. Propylene glycol monostearate
 $\pi = 10.0$ d/cm

b. 1,3 dipalmitoyl glyceryl phosphoric acid
 $\pi = 4$ d/cm

a. Egg albumin
 $\pi = 0.4$ d/cm



Long-chain fatty acid esters

Several esters were examined and the results (Z_1 dispersion) are presented in Figure 35. These systems were of interest in that the hydrophilic group is rather bulky so that several film properties are modified, e.g., the compressibility of these films is rather large compared to stearic acid. Since k_e is related to the inverse of the compressibility, smaller elastic constants should be necessary to fit the data. This was not so; large values of k_e were again necessary to fit the experimental data. Apparently the compression frequency was high enough to cause these monolayers to behave as solid films.

Heptanoic acid

We had experimental evidence, gathered by Hansen and Wallace (39) using the vibrating jet technique, that the time constants for film formation on aqueous, concentrated heptanoic acid solutions were in a region accessible to our present instrumentation. We wished to check our soluble monolayer theory and to search for anomalous dispersion associated with the relaxation time for film formation. The experimental data are presented in Figures 36, 37 and 38.

We were able to fit the data taken at the lower concentration level using the quantity $\frac{1}{RT} \left(\frac{\partial \mu_s}{\partial \Gamma} \right) \Gamma_0$ derived from the equilibrium surface tension study of King (38) noted in the

Figure 36. Dependence of Z_1 and Z_6 on frequency for
heptanoic acid solution (soluble monolayer
system) - $\gamma = 50.7$ d/cm

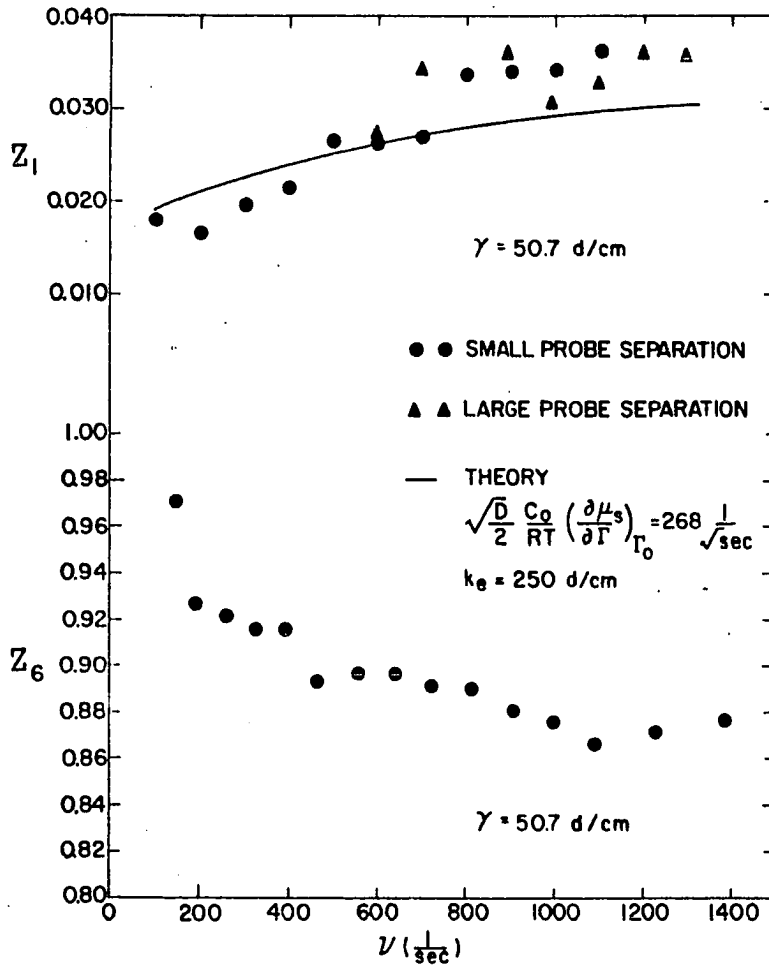


Figure 37. Dependence of wave velocity on frequency for heptanoic acid solution (soluble monolayer system) - $\gamma = 37.6$ d/cm

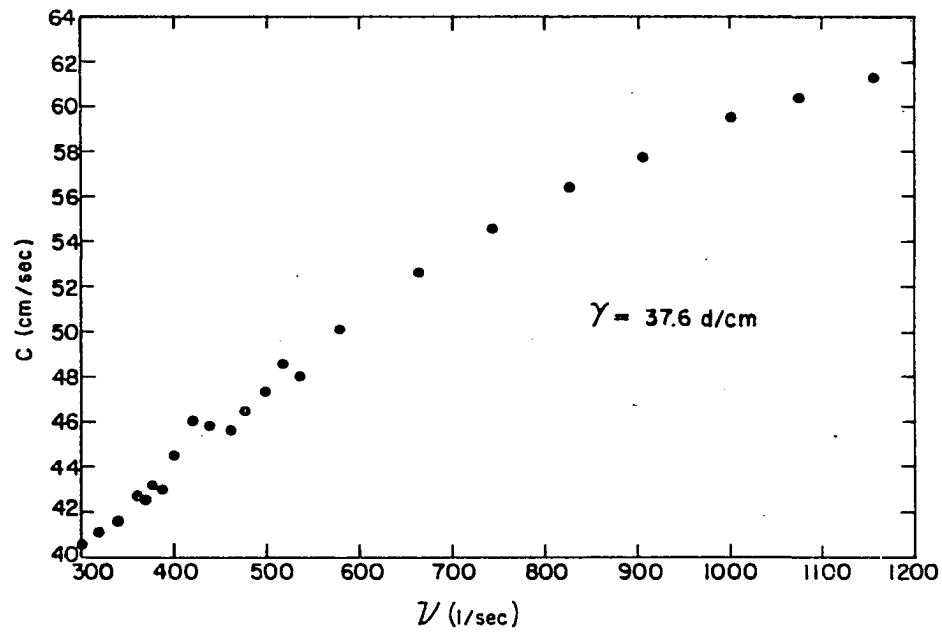
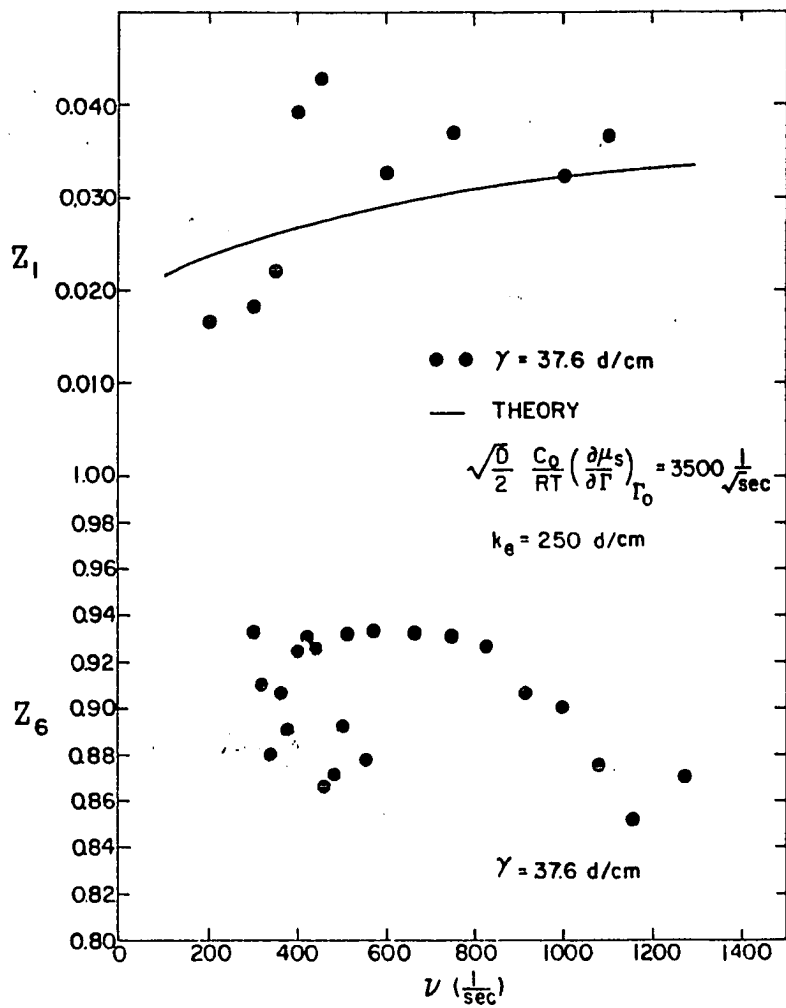


Figure 38. Dependence of Z_6 and Z_1 on frequency for heptanoic acid solution (soluble monolayer system) - $\gamma = 37.6$ d/cm



last section (Figure 36). A somewhat larger elastic constant parameter was needed for the fit, but this appears consistent with our previous results on insoluble monolayers.

The higher concentration study appeared to develop an anomalous velocity dispersion region (Figures 37 and 38) close to 400 cps, and this is precisely the relaxation region predicted from the extrapolated data of Hansen and Wallace. However, we must hasten to add that this can be only a tentative result since the unfavorable signal to noise ratio experienced during the experimental work on this system increased the probable error in the measurement so as to nearly obscure the true character of the curve.

The damping parameter, Z_1 , also varied abnormally in the frequency region close to 400 cps. Excluding the two points at 400 cps and 450 cps, the experimental data bracketed the theoretical curve rather well (Figure 38).

We feel that the diffusion control wave damping theory was consistent, after acknowledging the error level, with the experimental data; however, the abnormality noted certainly warrants further study.

Z_6 dispersion

It was interesting to note that, as predicted for systems described by large k_e values, the Z_6 dispersion on

insoluble monolayers was essentially independent of film composition or spreading pressure, Figure 39. However, this dimensionless group was very sensitive to deviations in propagation velocity, i.e., this parameter will be very sensitive to abnormal dispersion effects. The Z_6 plot (Figure 38) for the heptanoic acid system with $\gamma = 37.6$ d/cm will serve as an example of this property.

Conclusions and Recommendations

Since our theory predicts the ripple dispersion properties to within experimental and computational error, we conclude that the formulation is valid to at least the first order of approximation. We need to improve the calculation technique by striving to eliminate the order of magnitude assumptions that were invoked to produce Equations 81 and 82 from Equations 73 and 74 in the theory section. The horrendous amount of algebraic manipulation necessary to put (without further assumptions) Equations 73 and 74 into a form which would allow calculation of Z_1 and Z_6 caused us to take the approach discussed in This Thesis. Now that we have some confidence in the correctness of the theory, the two equations should be solved not only for Z_1 and Z_6 to a much better approximation but also solutions should be tabulated over a much wider frequency range. In particular, the low frequency range would be of interest. However,

Figure 39. Comparison of Z_6 dispersion data on insoluble monolayers

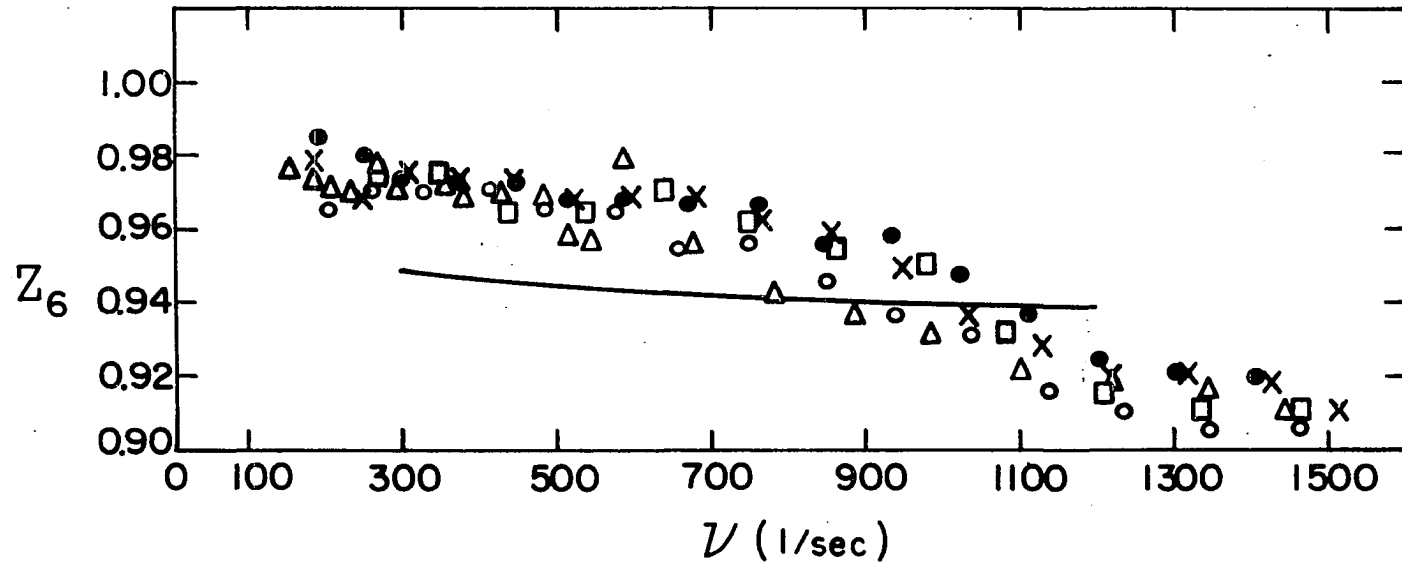
X - Mixed monolayers of stearic acid and polyvinyl acetate
($\pi = 16.5$ d/cm)

⊙ - Propylene glycol monostearate ($\pi = 10.0$ d/cm)

○ - 1,3 dipalmitoyl glyceryl phosphoric acid ($\pi = 4$ d/cm)

□ - Mixed monolayer of octadecanol and hexadecanol
($\pi = 0.5$ d/cm)

Δ - Egg albumin ($\pi = 0.4$ d/cm)



gravity effects must be included in the frequency region below approximately 100 cps.

The soluble monolayer theoretical calculation should be extended to include a much wider frequency range and a detailed study should be made of the nature of the solutions as the concentration, diffusion coefficient and $\frac{1}{RT} \left(\frac{\partial \mu_s}{\partial r} \right) r_0$ parameters are varied. It would be interesting to construct a soluble monolayer theory assuming that the adsorption rate is barrier controlled.

It would be interesting to attempt to program solutions of the two systems of complex simultaneous equations using subroutines to perform the necessary algebraic manipulations on the complex quantities needed to complete the calculation.

Instrumentation was developed that handles the frequency region embracing 100 cps to 1400 cps with good precision, especially with respect to the propagation velocity determination. The present equipment can be used beyond these limits; however, the probable error level increases rapidly outside of this frequency region. Instrumentation should be developed that will allow velocity and damping measurements down to at least 10 cps. The compression hysteresis found in our film balance work implies that stress relaxation should exist and may become important in this low frequency region. It should also be true that

k_e will approach $\frac{1}{\beta}$, where β is the film compressibility, as the frequency goes to zero.

Two sets of data showed rather interesting deviations from our theory: the low spreading pressure region for the mixed monolayer system, stearic acid-polyvinyl acetate, and the high spreading pressure region for the heptanoic acid soluble monolayer system. Further work with these systems might give us insight into the role of the substrate on film properties.

Our theory predicts rather interesting Z_1 and Z_6 dispersion if k_e is sufficiently small and k_v is sufficiently large. A search for such systems should be initiated. Shorter chain fatty esters of the 1,3 dipalmitoyl glyceryl phosphoric acid type might be of interest. However, extensive film balance work would be required on these somewhat obscure systems. Polymer systems, especially at low spreading pressures, should be explored.

Our experimental results imply that the ultra low spreading pressure region for liquid or gaseous types of monolayers such as lauric acid and many polymer systems might be of interest. We should be able to see the experimental curves go from the clean surface characteristic dispersion to the rigid monolayer characteristic dispersion while the spreading pressure remains essentially zero.

Our experimental technique could be applied to the

measurement of adsorption kinetics. At constant probe separation, one would need only to monitor the phase angle change with time to obtain rate of surface tension change data. This technique could bridge the gap between the vibrating jet technique applied to fast adsorption kinetics (e.g., heptanoic acid) and, for example, the drop weight technique for slow adsorption kinetics (e.g., decanoic acid). This time region holds rather critical information for workers interested in the kinetics of adsorption from solution.

Finally, the technique could be applied to liquid-liquid interface measurements. The theory would need to be recast; however, one form of this more general theory was given by Koussakov (19). The lateral interaction forces within the film residing at the liquid-liquid interface are greatly diminished. The dispersion should be more sensitive to these effects in the liquid-liquid systems than in the liquid-air systems where the interaction forces are much larger.

While we have accomplished the four goals listed in the introduction to This Thesis, the search leading to an understanding of the visco-elastic nature of surface films has only begun. We hope that the technique and theory described here will develop into a powerful tool for the exploration of the mechanical properties of monolayer systems.

SUMMARY

The propagation properties of surface tension controlled ripples traveling on aqueous-monolayer systems were studied theoretically and experimentally. The boundary value problems describing wave propagation in these systems were derived and solved from the viewpoint of continuum hydrodynamics. Two cases were discussed extensively, i.e., propagation on insoluble monolayer systems and propagation on soluble monolayer systems. The first case involved a surface elasticity parameter (k_e) and a surface viscosity parameter (k_v) while the second case added a term to the elastic parameter (k_e) resulting from the diffusion flux assumption.

The resulting equations were converted into a dimensionless form and simplified by order of magnitude assumptions. First order calculations for damping coefficient dispersion and propagation velocity dispersion as functions of the surface parameters (surface tension, film elastic constant, and film viscosity constant) were programmed on the "Cyclone" computer.

While an automatic recording surface balance was also designed and built, the experimental effort was centered on the development of the instrumentation necessary for the quick and accurate measurement of the propagation parameters

associated with capillary ripples traveling through surface films. A unique feature of our detection system was that a commercial, high output, crystal phonograph cartridge served to sense the very small amplitude surface waves generated during an experiment. Comparisons of the wave amplitude and the phase relation between the wave generator and detector done as a function of frequency and probe separation allowed calculation of the wave velocity dispersion and wave damping coefficient dispersion. These data were compared with the results of the theoretical calculation.

The insoluble monolayer theory was well substantiated by the experimental results on the systems studied: monolayer free water, stearic acid, several fatty acid esters, several mixed monolayer systems and a naturally occurring polymer system (egg albumin).

The soluble monolayer theory was substantiated by the experimental results on aqueous heptanoic acid solutions. However, the experimental data scatter was, at times, appreciable at the rather high concentration levels studied. There was a hint of relaxation dispersion, probably associated with an adsorption time constant, in the data recorded at the higher concentration level ($\sim 1.4 \times 10^{-2}$ moles/liter) studied. Further work is needed to substantiate this result.

LITERATURE CITED

1. Adam, N. K. The physics and chemistry of surfaces. 3rd ed. London, Oxford University Press. 1941.
2. Harkins, W. D. The physical chemistry of surface films. New York, N. Y., Reinhold Publishing Corporation. 1952.
3. Adamson, A. W. Physical chemistry of surfaces. New York, N. Y., Interscience Publishers, Inc. 1960.
4. Davies, J. T. and Rideal, E. K. Interfacial phenomena. New York, N. Y., Academic Press, Inc. 1961.
5. Tschoegl, N. W. J. of Colloid Science 13: 500. 1958.
6. Stoker, J. J. Water waves. New York, N. Y., Interscience Publishers, Inc. 1957.
7. Pockels, A. Nature 43: 437. 1891.
8. Thomson, W. Philosophical Magazine 42: 368. 1871.
9. Brown, R. C. Proceedings Physical Society of London 48: 312. 1936.
10. _____ Proceedings Physical Society of London 48: 323. 1936.
11. Dorsey, N. E. Physical Review 5: 170. 1897.
12. Watson, F. R. Physical Review 12: 257. 1901.
13. Gorter, E. and Seeder, W. A. Kolloid Zeitschrift 58: 257. 1932.
14. Lamb, H. Hydrodynamics. 1st American ed. New York, N. Y., Dover Publications. 1945.
15. Klemm, A. Physikalische Zeitschrift 40: 483. 1939.
16. Wiegardt, K. Physikalische Zeitschrift 44: 101. 1943.
17. Dorrestein, R. Proceedings Koninklijke Nederlandse Akademie Van Wetenschappen Ser. B, 54: 260. 1951.

18. Levich, V. Acta Physicochimica U. R. S. S. 14: 307. 1941.
19. Koussakov, M. Acta Physicochimica U. R. S. S. 19: 286. 1944.
20. Emmons, H. W., Chang, C. T., and Watson, B. C. J. of Fluid Mechanics 7: 177. 1960.
21. Ursell, F., Dean, R. G., and Yu, Y. S. J. of Fluid Mechanics 7: 33. 1960.
22. Crapper, G. D. J. of Fluid Mechanics 2: 532. 1957.
23. Case, K. M. and Parkinson, W. C. J. of Fluid Mechanics 2: 172. 1957.
24. Landau, L. D. and Lifshitz, E. M. Fluid mechanics. London, Pergamon Press, Ltd. 1959.
25. Wehausen, J. V. and Laitone, E. V. Handbuch der Physik 9: 446. 1960.
26. Truesdell, C. A. The kinematics of vorticity. Bloomington, Ind., Indiana University Press. 1954.
27. Sommerfeld, A. Mechanics of deformable bodies. New York, N. Y., Academic Press, Inc. 1950.
28. Birkhoff, G. Hydrodynamics, a study in logic, fact and similitude. Princeton, New Jersey, Princeton University Press. 1960.
29. Levich, V. Acta Physicochimica U. R. S. S. 14: 321. 1941.
30. Mann, J. A. and Hansen, R. S. Review of Scientific Instruments 31: 961. 1960.
31. LaMer, V. K. and Robbins, M. L. J. of Colloid Science 15: 123. 1960.
32. Hillier, K. W. and Kolsky, H. Proceedings Physical Society of London Ser. B, 62: 111. 1949.
33. Bull, H. B. J. of the American Chemical Society 67: 4. 1945.

34. Trurnitt, H. J. J. of Colloid Science 15: 1. 1960.
35. Zuidema, H. H. and Waters, G. W. Industrial and Engineering Chemistry, Analytical Edition 13: 312. 1941.
36. Lange, N. A. Handbook of Chemistry. 8th ed. Sandusky, Ohio, Handbook Publishers, Inc. 1952.
37. Hildebrand, F. B. Introduction to Numerical Analysis. New York, N. Y., McGraw-Hill Book Company, Inc. 1956.
38. King, H. H. Kansas State Agricultural College Technical Bulletin No. 9. 1922.
39. Hansen, R. S. and Wallace, T. C. J. of Physical Chemistry 63: 1085. 1959.
40. Ries, H. E. and Walker, D. C. J. of Colloid Science 16: 361. 1961.

ACKNOWLEDGMENTS

We gratefully acknowledge the help and encouragement of Professor R. S. Hansen. His deep insight into the physics and chemistry of surface phenomena have been a source of inspiration during this study.